Micromécanique et macromécanique des matériaux souples renforcés par des nanoparticules inorganiques

Mahrez Saadedine

THÈSE DE DOCTORAT

opérée au sein de

L'Université des Sciences et de la Technologie Houari-Boumediène

Laboratoire de Mécanique Avancée– LMA

Et

L'Université de Lille

École doctorale n°632 : Sciences de l'Ingénierie et des Systèmes – ENGYS

Laboratoire de Génie Civil et géo-Environnement – LGCgE ULR4515

Micromécanique et macromécanique des matériaux souples renforcés par des nanoparticules inorganiques

Thèse en cotutelle présentée et soutenue publiquement

Le **15/12/2022**, par

Mahrez SAADEDINE

pour obtenir le grade de

Docteur en Construction, Fabrication et Fiabilité Mécanique de l'Université des Sciences et de la Technologie Houari-Boumediène

Et

Docteur en Mécanique, Energétique, Matériaux de l'Université de Lille

Devant le jury composé de :

Fahmi BEDOUI, Professeur Université de Technologie de Compiègne	Rapporteur
Mabrouk HECINI, Professeur Université de Biskra	Rapporteur
Sophie BARRAU, Maître de Conférences, HDR Université de Lille	Examinatrice
Sabine CANTOURNET, Directrice de Recherche Mines Paris, Université PSL	**Présidente**
Cristian OVALLE, Chargé de recherche Mines Paris, Université PSL	Examinateur
Qiang GUO, Docteur Université de San Diego	Examinateur
Amar MESBAH, Professeur Université des Sciences et de la Technologie Houari-Boumediène	Membre invité
Nourdine OUALI, Professeur Université des Sciences et de la Technologie Houari-Boumediène	Directeur de thèse
Fahmi ZAIRI, Professeur Université de Lille	Directeur de thèse

Acknowledgements

Apart from the efforts of me, the success of this thesis depends largely on the encouragement and guidelines of many others. I take this opportunity to express my gratitude to the people who have been instrumental in the successful completion of this thesis.

I want to deeply thank my supervisor, Prof. Fahmi ZAIRI. In the past three years, he gave me great guidance from the subject selection, data analysis, to the writing of the thesis. Prof. Fahmi ZAIRI always took time out of his busy schedule to carefully work with me, checking word by word with huge patience. His rigorous academic researching spirt will inspire me forever. In life, he always makes me feel warm because of his great enthusiasm and considerateness. Herein, I would like to express my deep gratitude to him. I can't say thank you enough for his tremendous support and help. Working with him is one of the luckiest things in my life.

I was lucky to have two supervisors, I would like to express my most sincere thanks to my second supervisor Prof. Nourdine OUALI who has also made great contributions in my work. He gave me many valuable guidance and suggestions in my study and routine life. It is my greatest luck to meet him on the academic road.

I'm also grateful to Prof. Amar MESBAH for his understanding, encouragement and unlimited support throughout this challenging work. Completing tough steps of PhD would not have been imaginable without his endless support.

My deep appreciation extends to the other members of the jury, for their willingness to join my thesis committee and the time that they took out of their schedules to review my thesis.

I would also like to genuinely thank every student, staff and professors from LgcGE laboratory, Prof. Ali ZAOUI, Amar ALJER who helps us whenever we need him, Ramzi, Malek SIBAI and Christelle SANDRAS.

Last but not least, the guidance and support received from all my friends/ brothers. They have added much in my life. I would like to thank my Abdou for his aid and suggestion in my initial way of research. I would also like to thank Anwer for all the moments we spent together, traveling, training, eating with him was a pleasure. Thank's Amida for the delicious cooking ! I also thank, Malek, Ramdane, Yacine……the list is way too long to name you all, I am sure you will recognize yourselves. Thank you, guys.

Finally, I am grateful to my family, parents, sister, aunts, they give me endless loves. Thanks to them.

Thanks to all of you.

Dédicaces

A Maman et papa :

Fatma Benaiche

&

Nacer SAADEDINE

Je me permets de m'adresser au tandem sans lequel je n'aurais jamais existé. Mes chers parents ! Vous étiez toujours un modèle d'éthique, de bienveillance, de vigueur, de détermination et d'endurances, dont je suis extrêmement fière. Vous vous êtes voués à me préparer une atmosphère propice pour grandir m'épanouir et me construire. Merci d'avoir fait de moi ce que je suis. Merci pour l'amour et l'attention avec lesquels vous m'avez ceint. Merci pour le sens de persévérance et de ténacité que vous m'avez inculpé. Merci d'avoir cru en moi, de m'avoir aidé à édulcorer mon parcours et surtout, de m'avoir supporté. Si je me trouve actuellement à ce stade, c'est grâce a vous deux. Ainsi, permettez-moi de vous dédier ce travail et le fruit de ce travail. Vous êtes les véritables docteurs aujourd'hui.

Micromechanics and macromechanics of soft materials reinforced by inorganic nanoparticles

Micromécanique et macromécanique des matériaux souples renforcés par des nanoparticules inorganiques

Summary

General introduction

General introduction

Amongst the new cohort of advanced materials, hydrogel-based nanocomposites, designed by incorporating nano-sized second phase into hydrogels, have fascinating properties. They have very recently attracted a lot of attention due to the new extraordinary opportunities that such sophisticated and multifunctional materials offer in a wide range of domains including aerospace, 3D printing, waste-water treatment, biomedical engineering (drug delivery and tissue engineering), sensors, actuators and energy storage.

While traditional (organically crosslinked) hydrogels have poor mechanical performances (e.g. low fracture toughness and limited ductility), this new class of nanocomposites is extremely resilient and extremely stretchable with an elongation than can exceed 3000%. Very recent studies have illustrated impressive improvements of mechanical properties, in addition to extreme stretchability, such as high toughness and high mechanical strength. The reinforcing effect of nanoparticles is attributed to several factors such as hydrogel matrix properties, nature (and amount) of nanoparticles and strength of interactions. Nanofillers considerably improve the structural stability of the hydrogels due to the occurrence of multiple specific interactions between the polar surface of the charges and hydrophilic chains such as hydrogen bonds, van der Waals interactions and electrostatic interactions, to achieve better chemical, electrical, mechanical and biological properties. These smart and adaptive materials combine the advantage of the nano-scale reinforcement and the multiphysics (chemical, physical, mechanical and biological) properties of hydrogels including biocompatibility (along with some similarities to biological tissues), stimulating responsiveness, adsorption performance and facile room temperature self-healing (by restoring initial microstructure and mechanical strength).

Whereas considerable efforts have been devoted to elaboration and characterization of hydrogel-

filler material systems, the mechanisms of nanofillers reinforcement remain largely misunderstood. A better understanding of the structure-property relationship for such new material systems is of prime importance in order to provide detailed information for their reliable design considering a rigorous set of their various specific characteristics: extreme stretchability and self-healing facility along with a strong viscous consistency. As a meaningful prerequisite of advanced applications of such new materials, the formulation of constitutive models is needed. Such tools would provide a better understanding of the separate and synergistic effects of key factors that govern the impressive improvements of mechanical properties. An exhaustive literature survey shows that the constitutive modelling of hydrogels is rare. Despite the important advance accomplished by these models, they cannot connect the nanostructure to the overall recovery behavior of hydrogel-based nanocomposites. A rigorous constitutive representation of the nanofiller-hydrogel material system, including explicit active interactions between nanofillers and hydrogel matrix, would allow to propose physically consistent explanations of the reinforcement mechanisms in connection to the nonlinear material response and the room-temperature self-healing facility. In this regards, only micromechanics-based approaches allow to propose a framework avoiding (or at least limiting) the arbitrary inclusion of heuristic parameters. Such a development would offer a way to gain a better understanding of the reinforcing effect of nanoparticles on the overall properties and to provide detailed information for their design. A constitutive representation that considers as well history-dependent effects and local matrix-nanoparticle interaction has not yet been developed. In the present PhD dissertation, a model, formulated within the framework of nonlinear continuum mechanics, is developed to constitutively correlate the behavior of nanocomposites to their internal network structures in terms of rubbery matrix and inorganic nanoparticles properties.

Objective and thesis plan

In order to realize our objective, the actual thesis was planned following several well-constructed steps that will be described in details through the following chapters:

In **Chapter** I, a succinct summary of classic knowledge which can be found in specialized works and that have been selected for their relevancy in the present study for the reader convenience. The classification, properties and industrial applications are briefly reported. It was followed by detailed literature survey on reinforced hydrogels in terms of their methods of preparation, and improvement of mechanical, electrical, biological and magnetic properties and their applications in biomedical applications.

In **Chapter II**, we present a model based on the Eshelby inclusion theory and the micromechanics framework using the concept of cubic material volume to account for the effective role of nanoparticles on the nonlinear and finite-strain macro-behavior of hydrogel-based nanocomposites. The hydrogel-nanofiller material system is representatively regarded as a cubic unit cell containing nine particles. A central nanoparticle connects eight nanoparticles placed at the cube vertices via a number of hydrogel chains. The model explicitly considers the chains network with dynamic reversible detachable/re-attachable mechanisms of bonds to coherently capture the rate-dependent extreme stretchability and some inelastic features including strong hysteresis upon stretching-retraction and continuous relaxation. A quantitative evaluation of our model is presented by comparisons to a few available experimental data of a variety of hydrogel-nanofiller material systems. The model is used to discuss some important aspects of the mechanisms of nanofillers reinforcement, failure and room temperature self-healing facility.

In **Chapter III**, the micromechanical model is further developed to capture the inelastic response of hydrogel-based nanocomposites by considering the swelling-damage coupling. The constitutive model formulated in a finite strain context introduces explicitly the hydrogel network features in terms of swelling and dynamic breaking-recombination. The effective interactions between the nanoparticles and the swollen hydrogel network are considered using a micro-macro scale transition within the Eshelby inclusion theory. The model is compared to experimental observations of a high-swelling capacity hydrogel-based nanocomposites reinforced with different concentrations of nanoparticles. The model is firstly identified using monotonic stretching data at an initial swelling state in terms of stress-strain response, energy dissipation and ultimate properties. The predictive capability of the model is then verified on a wide range of swelling ratios for a given nanofiller concentration. The efficiency of the model is further critically discussed by comparisons with history-dependent data under stretching-retraction and self-healing. The effects of nanoparticles and swelling on the self-healing response are shown thanks to the model.

In **Chapter IV**, we address the problem of the multiscale constitutive representation of the multiaxial inelastic behavior of elastomeric particulate composites. A fully three-dimensional model is proposed within a micromechanical treatment to describe the multiaxial inelastic response in relation to the reinforcement mechanisms. A network decomposition based on the tube confinement theory is used to consider the combined effects of multiaxiality and inelasticity. The near-field direct interactions between the particles and the rubber networks are physically described using the Eshelby inclusion theory. The capabilities of the microstructure-based model are evaluated for different modes of deformation over a wide range of filler concentrations. It is found able to successfully reproduce the significant features of the multiaxial macro-response upon

monotonic and cyclic loading sequences. Important insights about the effective role of the reinforcement mechanisms on the multiaxial dissipation are revealed.

A **general conclusion** closes this PhD dissertation with the main results obtained.

Chapter I

Structure and properties of advanced soft materials

CHAPTER I

Structure and properties of advanced soft materials

A succinct summary of classic knowledge, which can be found in specialized works and selected for their relevancy, is provided in this first chapter. For the reader convenience, we begin to briefly report general assessments including classification, properties and industrial applications. We then provide a detailed literature survey on hydrogel-based nanocomposites in terms of their methods of preparation, and improvement of mechanical, electrical, biological and magnetic properties with a special focus on their biomedical applications.

I.1 What is a soft material?

Soft materials are omnipresent in nature as most living organisms are composed of materials that are soft, such as tissue and organs of the human body. The complex physics that is orchestrated from the nano to the macroscale, in conjunction with the dynamic internal/external stimuli underlying biological processes, has inspired the design of sophisticated soft materials exhibiting stimuli-responsive features. As one of the most fascinating soft materials designed, hydrogels are a typical soft material that has a unique, three dimensionally cross-linked polymers network structure swollen with a large amount of water. They can be designed with controllable responses due to external environmental conditions (Koetting et al., 2020; Zhang et al., 2020; Yang et al., 2022). Hydrogels may change configurations in response to a variety of physical and chemical stimuli, where the physical stimuli include temperature, electric or magnetic field, light, pressure, and sound. While the chemical stimuli include pH, solvent composition, ionic strength, and molecular species (Jiang et al., 2020; Andrade et al., 2021; Arrizabalaga et al., 2022; Fragal et al., 2022; Hu et al., 2022) (Figure I.1). They can be used either in their natural state or can be developed synthetically. Extensive employment of these products in several industrial and environmental areas of application are considered to be of prime importance. Hydrogel materials are widely used in various fields like biomedical, electronics, tissue engineering, robotics, medicines and wastewater treatment.

I.2 Classification of hydrogel products

The hydrogel products can be classified on different bases as detailed below:

I.2.1 Classification based on source

Hydrogels can be classified into two groups based on their natural or synthetic origins (Deng et al., 2022; Long et al., 2022).

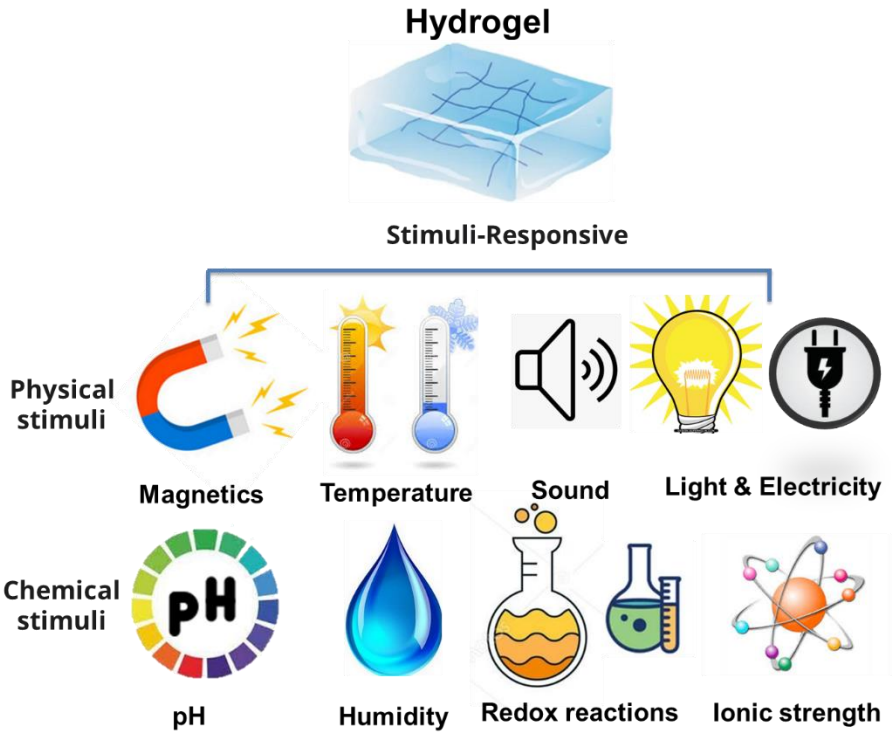

Figure I.1 Stimuli-responsive hydrogels reacting to physical and chemical stimuli.

I.2.2 Classification according to polymeric composition

The method of preparation leads to formations of some important classes of hydrogels. These can be classified as follows:

(a) Homopolymeric hydrogels (Dourado et al., 2021).

(b) Copolymeric hydrogels (Fox et al., 2020).

(c) Multipolymer interpenetrating polymeric hydrogel (Rungrod et al., 2022).

I.2.3 Classification based on configuration

The classification of hydrogels depends on their physical structure and chemical composition can be classified as follows:

(a) Amorphous (non-crystalline) (Xia et al., 2021).

(b) Semicrystalline: A complex mixture of amorphous and crystalline phases.

(c) Crystalline.

I.2.4 Classification based on type of cross-linking

a) Chemically cross-linked networks (Reis et al., 2021).

b) Physical networks (Pita-López et al., 2021).

I.2.5 Classification based on physical appearance

Hydrogels appearance as matrix, film, or microsphere depends on the technique of polymerization involved in the preparation process.

I.2.6 Classification according to network electrical charge

Hydrogels may be categorized into four groups on the basis of presence or absence of electrical charge located on the cross-linked chains:

(a) Nonionic (neutral) (Nguyen et al., 2011).

(b) Ionic (including anionic or cationic) (Shojaeiarani et al., 2021).

(c) Amphoteric electrolyte (ampholytic) containing both acidic and basic groups (Xu et al., 2022).

(d) Zwitterionic (polybetaines) containing both anionic and cationic groups in each structural repeating unit (Jiao et al., 2021).

I.3 Improving hydrogel properties with nanomaterials

With the current development in nanotechnology now make it is feasible to generate well-defined nanomaterials (in terms of sizes, shapes, and properties) from both organic and inorganic precursors which can be combined with soft materials. The innovative combination of nanomaterials and hydrogels creates synergistic, unique, and potentially useful properties that are not found in the individual components. However, the properties given to the hydrogel-nanocomposite systems

depend on the type of nanomaterials incorporated and synthesis method. The main aim of the incorporation of nanomaterials into the hydrogel (natural and synthetic) is to improve their mechanical, electrical, or biological properties. This combination increases the hydrogel properties. The resultant biomaterials could be used to optimize a variety of properties required for biomedical applications; these materials can be engineered as materials that better mimic the natural tissues. Improved properties of hydrogel-based nanocomposites can be attributed to their unique network structure as well as the specific way in which the nanomaterials interact with the surrounding polymers (Haraguchi et al., 2007). For instance, enhanced interactions due to surface functionalization of nanoparticles were demonstrated to influence mechanical, chemical, and biological properties all at once.

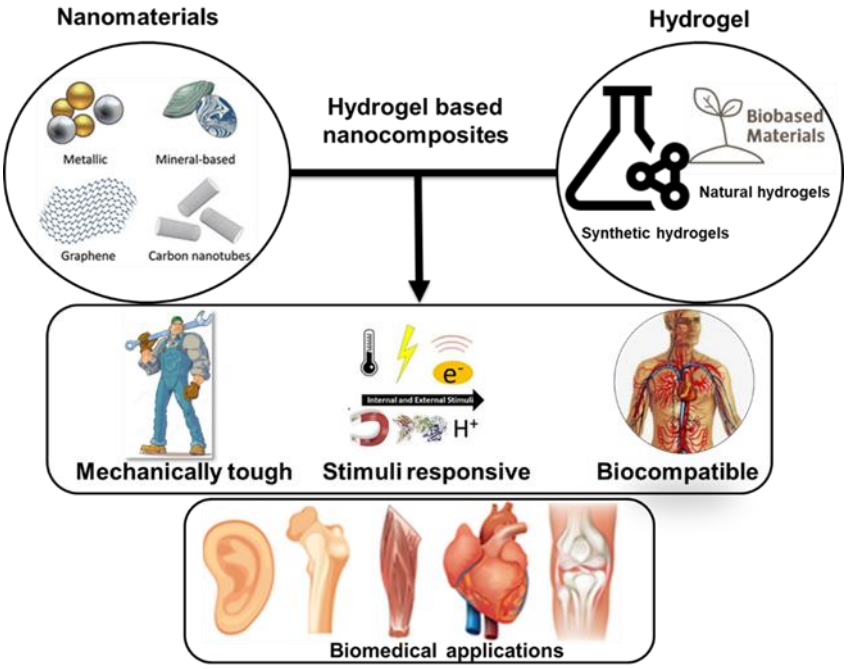

Figure I.2 With the right combination of nanomaterials and hydrogel, it is possible to manufacture mechanically tough, stimuli responsive, and biocompatible systems for biomedical applications.

I.3.1 Nanocomposite hydrogel synthesis

Generally, hydrogel-based nanocomposites can be synthesized from either synthetic polymers or natural polymers. Currently, there are several methods in which the incorporation of nanomaterials

into hydrogel can be achieved. These methods are applied to organic and inorganic nanomaterials (Figure I.2), and a wide range of nanomaterials were successfully incorporated into hydrogel networks (Thoniyot et al., 2015), by in situ polymerization, in situ growth of the nanoparticles, or physical mixing (Figure I.3). As a result, controlled network structures yielding hydrogel-based nanocompositeswith customized properties can be attained (Chen et al., 2018). Figure I.3 describes different ways used to fabricate nanocomposite hydrogel systems.

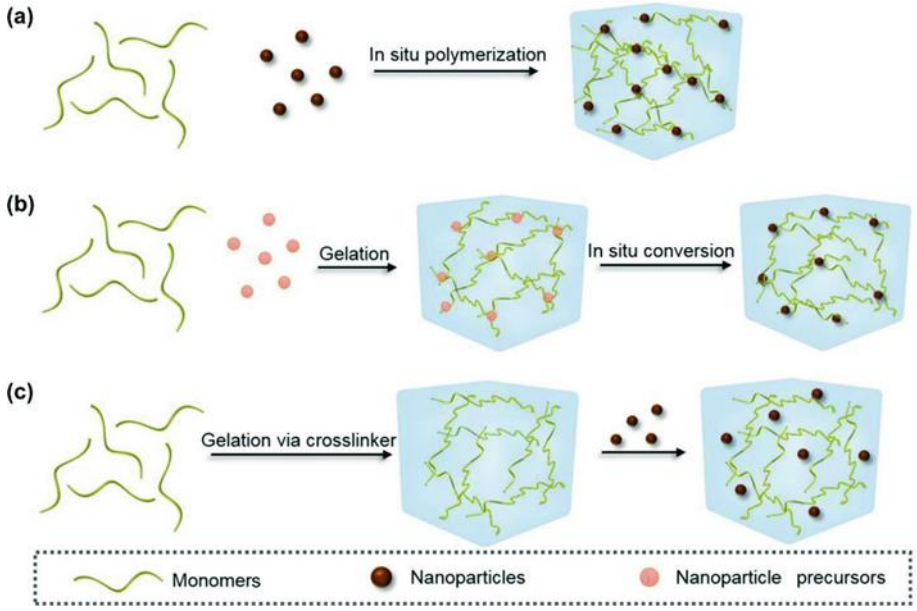

Figure I.3 Nanocomposite hydrogel synthesis: (a) in situ polymerization of monomer in nanoparticle suspension, (b) reactive nanoparticle synthesis within gelled materials, (c) physical embedding of nanoparticles into the hydrogel matrix after gelation (Chen et al., 2018).

I.3.2 Properties of hydrogel-based nanocomposites

Overall, the mechanical, physical, and biological properties of hydrogel-based nanocomposites vary depending on the synthesis strategy, nanomaterial choice, and network formation approach. By optimizing these parameters (individually or in synchrony) biomedically relevant hydrogel-based nanocomposites can be obtained and tailored applications will be possible for these materials.

I.3.2.1 Mechanical properties

Mechanical properties of materials are an essential feature, to improve mechanical properties, nanomaterials can be incorporated into the hydrogel network structures by physical crosslinking without the need for any organic crosslinkers. Nanomaterials can also act as chemical crosslinkers forming covalent bonds which leads to hydrogels with improved functionalities. Both natural and synthetic hydrogels using both organic and inorganic nanomaterials have been generated with enhanced mechanical performance (Haraguchi et al., 2003; Haraguchi, and Li, 2006, Bedoui et al., 2022) relevant to broad biomedical applications (Bach et al., 2013; Memic et al., 2015; Vedadghavami et al., 2017; Beldjilali-Labro et al., 2018; Esmaeili et al., 2022).

For example, in Figure I.4, hydrogel-based nanocomposites have been prepared by Haraguchi et al. (2007) with improved optical and mechanical properties that could be used for contact lens applications (Molina et al., 2015; Memic et al., 2015). Similarly, Li et al. (2021) prepared a SiO2@PANI core-shell nanoparticles which were used to enhance the mechanical and conductive properties of the P(AM/LMA) hydrogel. The mean diameter of Si-ANI particles was about 139.2 nm. The introduction of SiO2@PANI core-shell particles has improved the tensile strength, elongation at break, toughness, and elastic modulus of P(AM/LMA) hydrogel, by comparison to the pure PAM hydrogel (Figure I.5). The SiO2@PANI-P(AM/LMA) hydrogels were designed into various shapes to suit different applications.

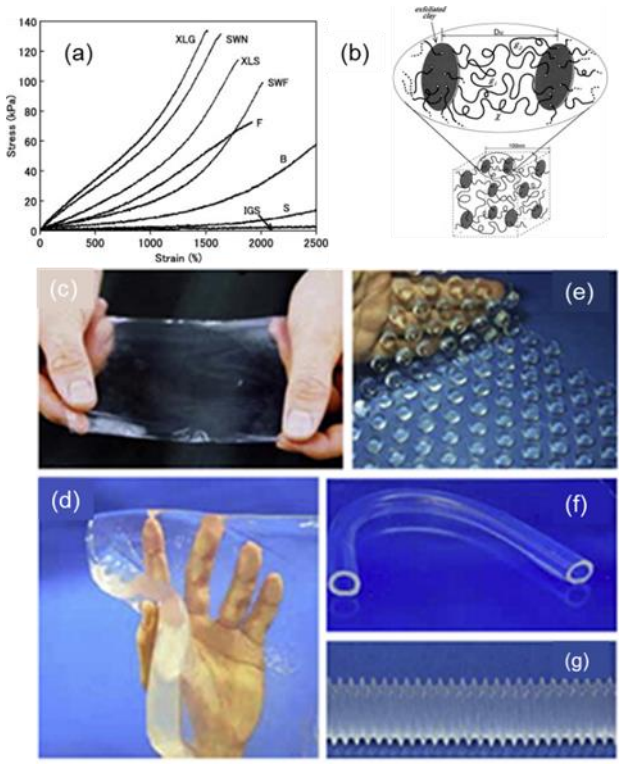

Figure I.4 (PDMAA-)/clay nanocomposite prepared using various kinds of clay: (a) tensile mechanical response of several kinds of hydrogel/clay nanocomposites, (b) schematic representation of the network structure. Panels c, d, e, f and g show a nanocomposite hydrogel obtained in various shape with extraordinary mechanical toughness: (c) thin film, (d) sheet, (e) uneven sheet, (f) hollow tube, and (g) bellows (Haraguchi et al., 2007).

In Figure I.6, a PAAm/exfoliated montmorillonite (MMT) nanocomposite were synthesized with unprecedented stretchability (fracture elongation up to 11 800%), toughness (fracture toughness up to 10.1 MJ m–3), and self-healing have been reported (Gao et al., 2015). Self-healable hydrogels have received considerable attention in recent years because of their good self-healing and mechanical performances. The remarkable performances of these materials are typically demonstrated by physical cross-linking (non-covalent bonding) between polymer chain and nonreinforcements.

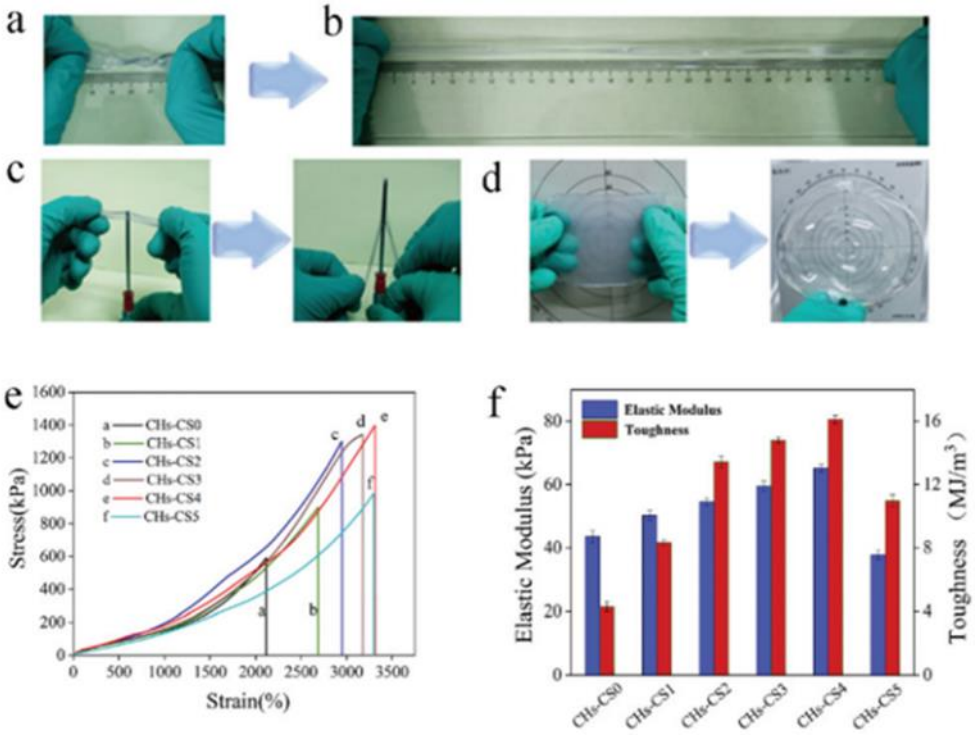

Figure I.5 SiO2@PANI-P(AM/LMA) hydrogels showing extraordinary mechanical properties: (a) Under curl, (b) stretch under curl, (c) puncture resistance, (d) blowing a ‘‘hydrogel balloon’’, (e) tensile stress-strain curve (the tensile strength of 589 kPa and elongation at break of 2100% was obtained), and (f) elastic modulus (43 kPa) and toughness (4.3 MJ m^3) (Li et al., 2021).

Shao et al. (2017) prepared a fully physically stretchable, recoverable, and self-healable cross-linked nanocomposite hydrogel (PAA-CNF-$Fe3^+$) by in situ free radical polymerization. In the resultant nanocomposite, the coordination bonds act as strong bonds and maintain primary structure, whereas the hydrogen bonds act as weak bonds to form a sacrificial network.

Adding to that, the coordination bonds are dynamic and serve as sacrificial bonds to dissipate energy after the rupture of hydrogen bonds, giving a unique combination of high toughness, fast self-recovery, and significant self-healing property after deformation or damage (Figure I.7).

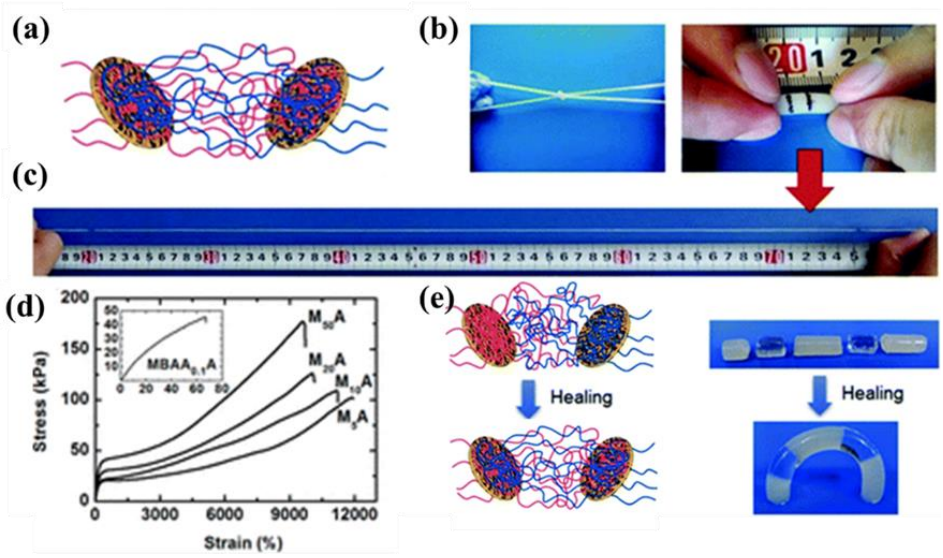

Figure I.6 Montmorillonite nanosheet crosslinked hydrogels: (a) Polymer chains are adsorbed on clay nanosheets, (b) the obtained hydrogels are very flexible and (c) stretchable to very large strains, (d) uniaxial tensile stress-strain curves show that the fracture strain was as high as 11 800%, (e) the polymer chains are able to migrate across the interface of two hydrogels in contact, leading to complete self-healing (Gao et al., 2015).

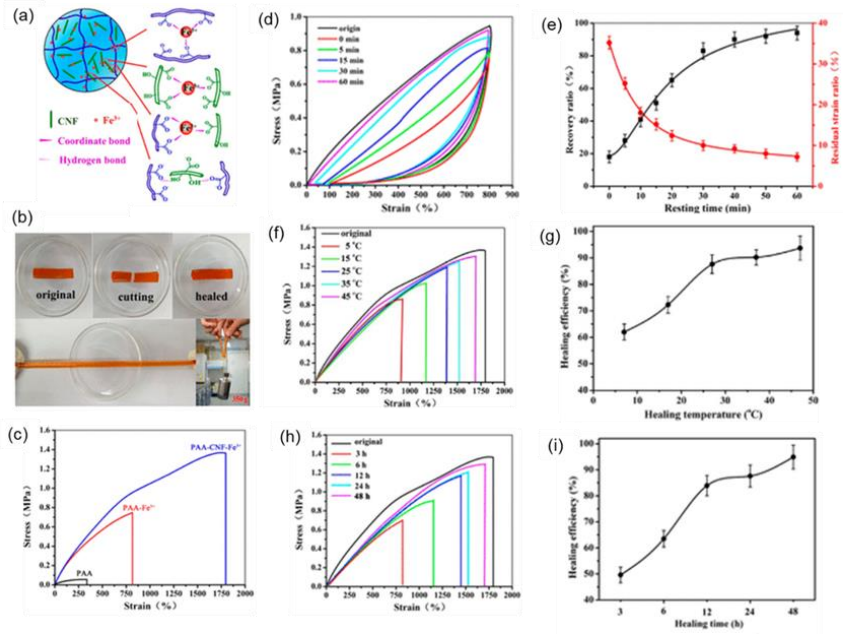

Figure I.7 (a) Schematic of PAA-CNF-Fe^{3+} physical hydrogel, (b) hydrogel specimens were cut into halves and self-healed without any external intervention at the ambient temperature, the healed hydrogel can sustain stretching and lifting a weight of 350 g, (c) tensile stress-strain curves of PAA, PAA-Fe^{3+}, and PAA-CNF-Fe^{3+}, (d) cyclic tensile loading-unloading curves with different resting times between two successive measurements, and (e) corresponding recovery ratio and residual strain, (f) stress-strain curves of PAA-CNF-Fe^{3+} with different healing temperatures and (g) corresponding healing efficiency, (h) stress-strain curves of the original and self-healed gels at various healing times and (i) corresponding self-healing efficiency (Shao et al., 2017).

Self-healing zirconium hydroxide nanocomposite hydrogel (Zr-NC gel) developed by Jiang et al. (2017) were fabricated by in-situ free radical copolymerization. This nanocomposite was prepared using non-covalent hydrogen bonding interactions between polymer chains and zirconium hydroxide. The obtained tough hydrogel has excellent self-healing properties at room temperature (Figure I.8).

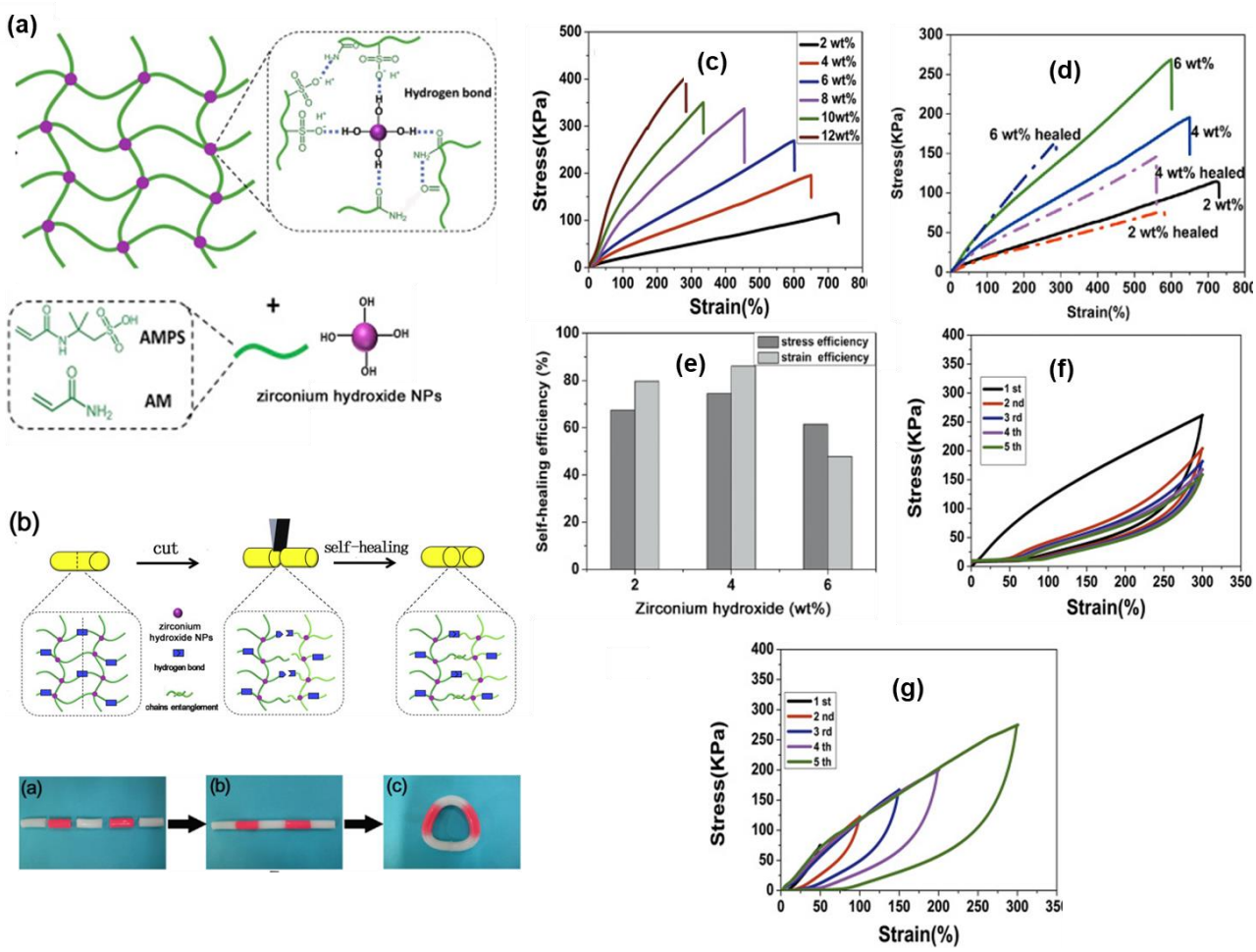

Figure I.8 (a) Schematic illustration of the synthesis of Zr-NC gels with zirconium hydroxide nanoparticles as crosslinkers, (b) self-healing process consisting of two healing mechanisms including hydrogen bonds recombination and polymer chain entanglements and (b) photographs of the self-healed Zr-NC gel, (b.a) the samples were cut into several blocks and two of them were dyed with methyl orange for visualization of the cut surfaces, (b.b) the separated blocks were brought into contact at room temperature without external stimulus, (b.c) the healed sample was mechanical tough which could be brought into a circle, (c) the tensile stress-strain curves with various zirconium hydroxide contents, (d) stress-strain curves of the original and healed Zr-NC gels, (e) the corresponding self-healing efficiency, (f) cyclic loading-unloading tensile testing with the same sample levels of maximum strains, (d) fixed maximum strain of 300% by cyclic tensile test of five times for Zr-NC gel with 6 wt% zirconium hydroxides (Jiang et al., 2017).

Soft materials exhibit a complex mechanical behavior. Cyclic loading-unloading tensile testing is a way to analyze this complex mechanical behavior and the internal fracture process of soft materials. The resulting stress-strain curves can be used as indices to assess the energy dissipation and the mechanical properties of the materials.

The change in mechanical properties of nanocomposites under cyclic loading was firstly observed by Mullins and his co-workers (Mullins, 1948, 1969; Mullins and Tobin, 1957, 1965). The principal phenomenological observations described by Mullins and co-workers can be summarized as follows:

- The softening is uniquely observed under higher elongations than the preceding ones in the loading history.
- An induced anisotropy as a consequence of the softening.
- The softening increases with an increasing volume of fillers.
- The complete recovery of the initial stiffness is never reached.
- The softening behavior is seen also from non-dilating load conditions, i.e. compression and shearing tests.

Additional to the first pre-strain softening (Mullins effect), the effect of repeated deformation leads the rubbery materials to approach asymptotically a steady state with a constant – equilibrium – stress response (Figures I.8-I.10). Softening occurs in both filled and non-filled soft materials. Numerous authors (Bouasse and Carrière, 1903; Shedd and Ingersol, 1904; Schwartz, 1907) published data demonstrating that stretching resulted in a softening of rubber. However, Holt (1931) was the first to describe the effects of repeated stretching and stretching-speed on the stress-strain properties of rubber compounds.

Together with the progressive softening during repeated deformation, Holt (1931) also showed that stretching to a series of increasing strains resulted in a progressive increase in the observed softening at low strains. Numerous authors have investigated the influence of filler particles on the stiffness of hydrogel-based nanocomposites (Figures I.7- I.10). Li et al. (2017) reports their strategy to design an ultrahigh mechanical strength, tough, and self-healable hybrid dual crosslinked polyacrylic acid (PAAc) hydrogel. The hybrid PAAc hydrogel was fabricated in a one-pot reaction with two types of crosslinking points, i.e. the primary chemical cross-linkers that create covalent cross-linking among PAA chains and the secondary physical cross-linkers Fe^{3+} that introduce ionic coordinates between $Fe3^{+}$ and −COO− groups (Figure I.9).

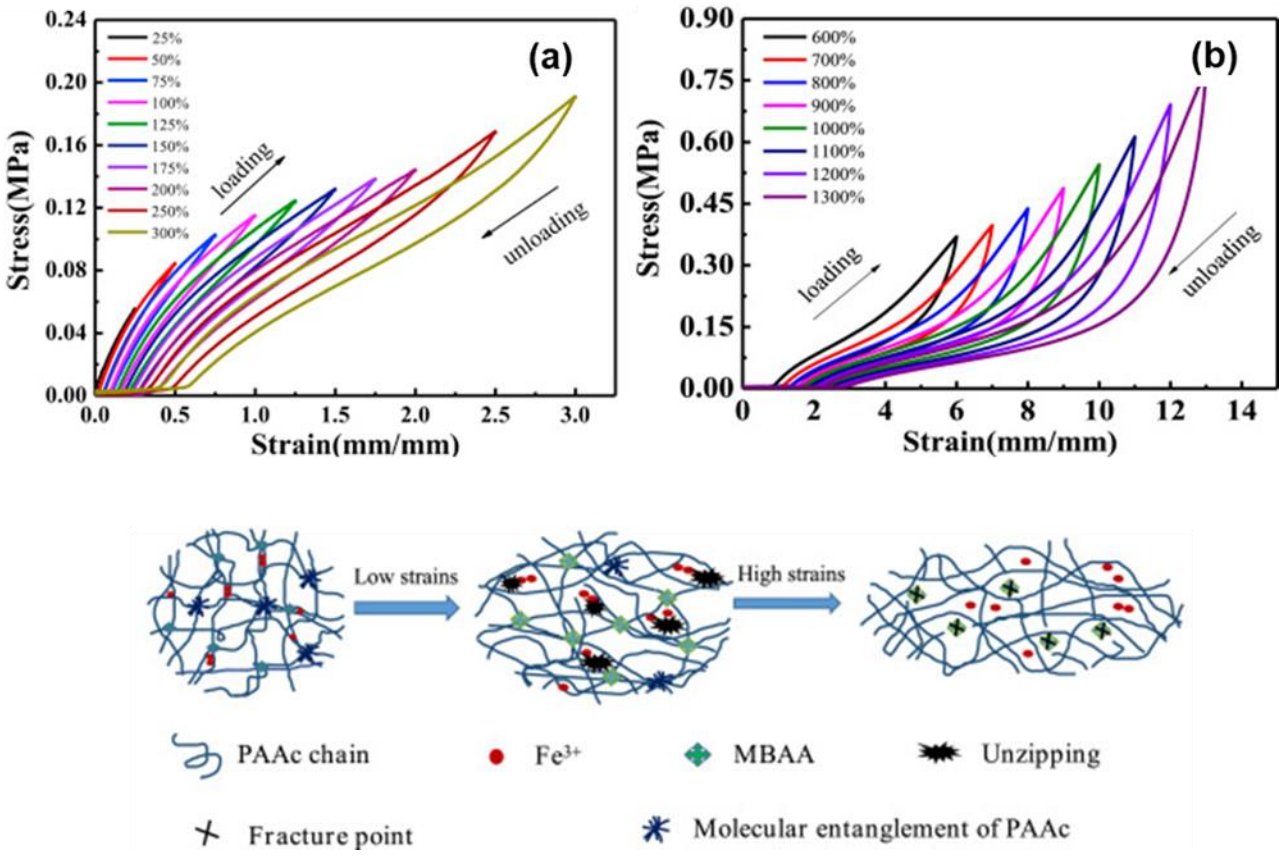

Figure I.9 Cyclic loading-unloading tensile testing of hybrid dual-crosslinked hybrid hydrogels under two different strain levels: (a) low and (b) high (Li et al., 2017).

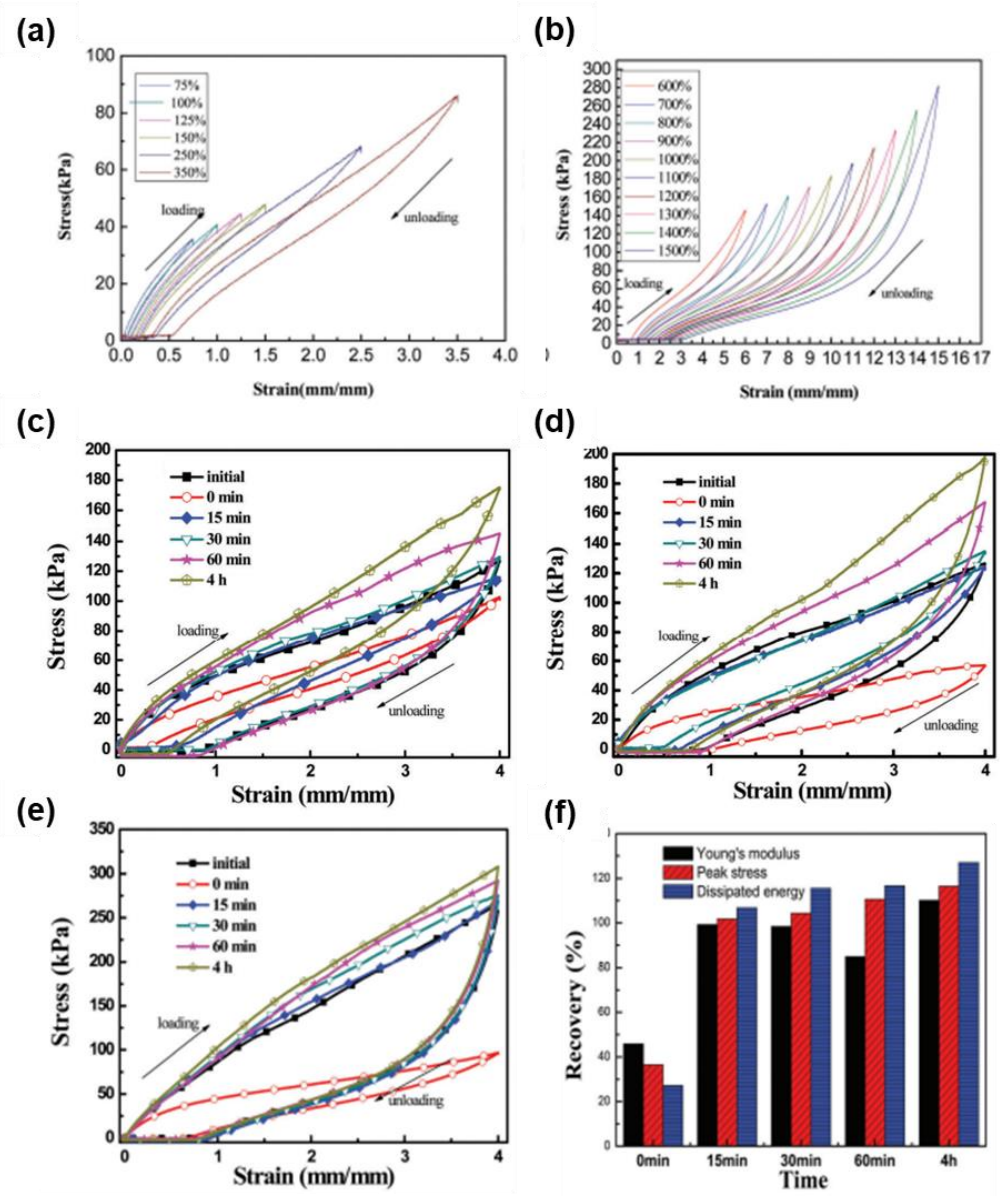

Figure I.10 Tensile hysteresis loops of Agar/PAAc-Fe^{3+} DN gels in (a) the small strain and (b) the large strain measured in a cyclic tensile test, (c) strain-stress curves of Agar/PAAc-Fe^{3+} DN gels recovered from a sealed bag at room temperature without any external stimuli, (d) strain-stress curves of Agar/PAAc-Fe^{3+} DN gels recovered from a ferric iron solution at room temperature, (e) strain-stress curves and (f) the recovery ratio of Agar/PAAc-Fe^{3+} DN gels recovered from a sealed bag at 50 °C without other external stimuli (Li et al., 2017).

In Figure I.10 an example of an Agar/PAAc-Fe^{3+} double network hydrogel which exhibited very favorable mechanical properties (tensile strength 320.7 kPa, work of extension 1520.2 kJ m^{-3}, elongation at break 1130%), fast self-recovery properties in Fe^{3+} solution (100% recovery within 30

min), in 50 °C conditions (100% recovery within 15 min), and under ambient conditions (100% recovery of the initial properties within 60 min), as well as impressive self-healing properties under ambient conditions has been reported by Li et al. (2017).

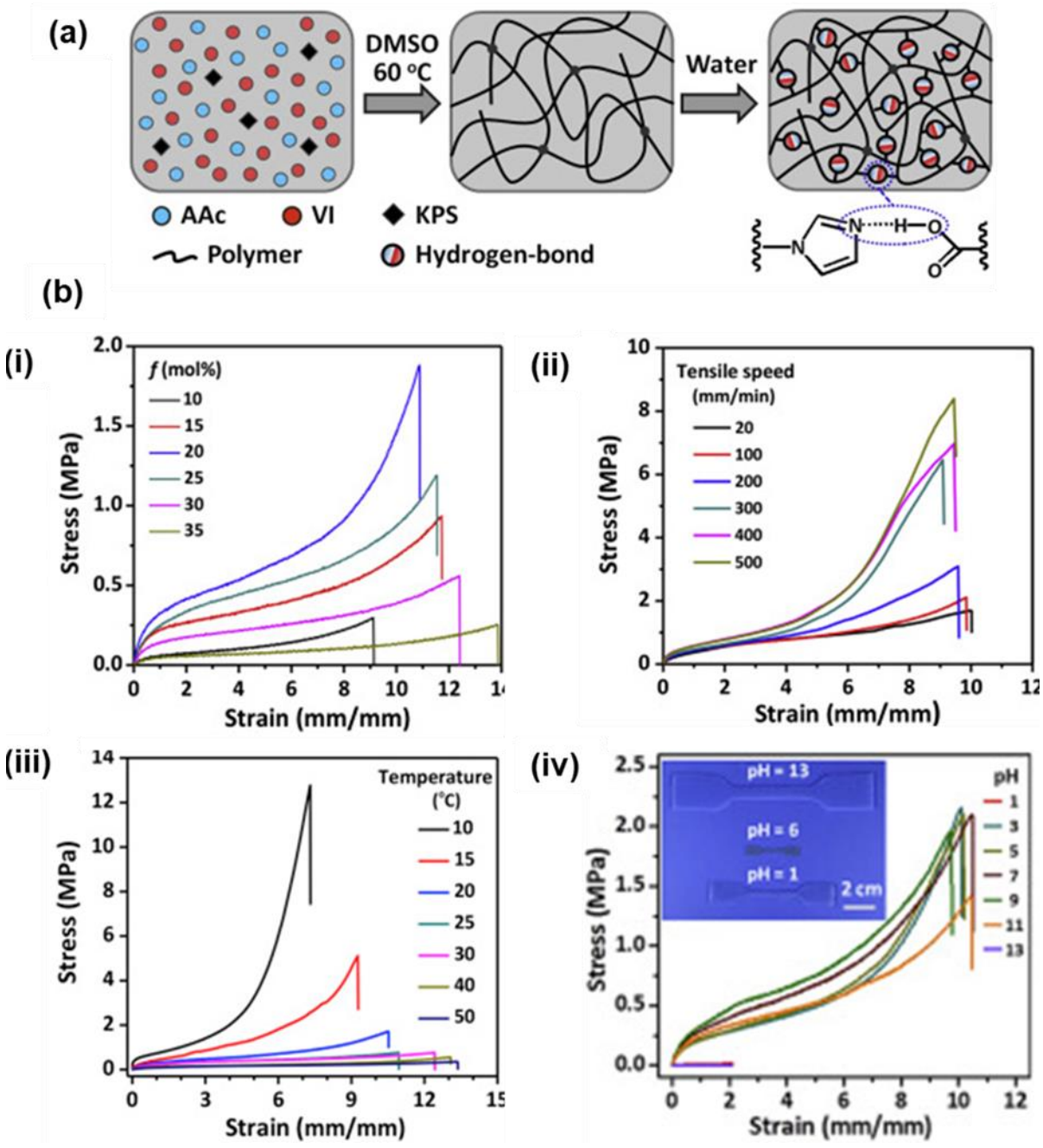

Figure I.11 (a) Schematic for the preparation of P(VI-co-AAc) hydrogels, (b) tensile stress-strain curves with different (i) molar fraction, (ii) displacement rate, (iii) temperatures, (iv) equilibrated in pH (Ding et al., 2017).

Soft materials exhibit a strong time-dependent mechanical behavior, and may change configurations in response to a variety of physical and chemical stimuli. The experiments of Ding et al. (2017) in which a tough (P(VI-co-AAc)) hydrogels (1-vinylimidazole-co-acrylic acid) reinforced by robust hydrogen bonds were synthesized by free-radical copolymerization. Their results demonstrate that the hydrogels with different compositions have excellent mechanical performances. The tough hydrogels also show temperature- and deformation rate dependency. Adding to this, the mechanical properties of the prepared hydrogels can be reversibly tuned by the pH of incubated solutions. In addition, the tough hydrogels also show fast self-recovery ability after unloading due to the dynamic nature of hydrogen bonds (Figure I.11).

I.3.2.2 Electrical properties

For many biomedical applications, the development of electrically conductive materials could be very beneficial. For example, a range of tissues require electrical conductivity including muscle, nerve, and cardiac tissues (Min et al., 2018; Wen et al., 2020). Developing electrically conductive hydrogels could be achieved by incorporating an array of conducting nanomaterials into the polymeric network. Conductive biomaterials could play important roles in drug delivery, biosensor, actuator applications and tissue engineering. The design of these conductive materials leads to biomaterials that better mimic the native tissue. For example, Arslantunali et al. (2014) used MWNT and poly (2-hydroxyethyl methacrylate) (pHEMA) to generate conductive hydrogel nanocomposites intended for nerve regeneration. Mehrali et al. (2017) hypothesize that new synthetic life-like forms with simple cognitive abilities and exceptional locomotive strength could emerge. With regard to future research and special attention should be given to 3D printing of intricate neural circuits or strong hybrid skeletal-muscle tissue from carbon-based hydrogel nanocomposites. By sculpting these parts into hybrid creatures (Figure I.12).

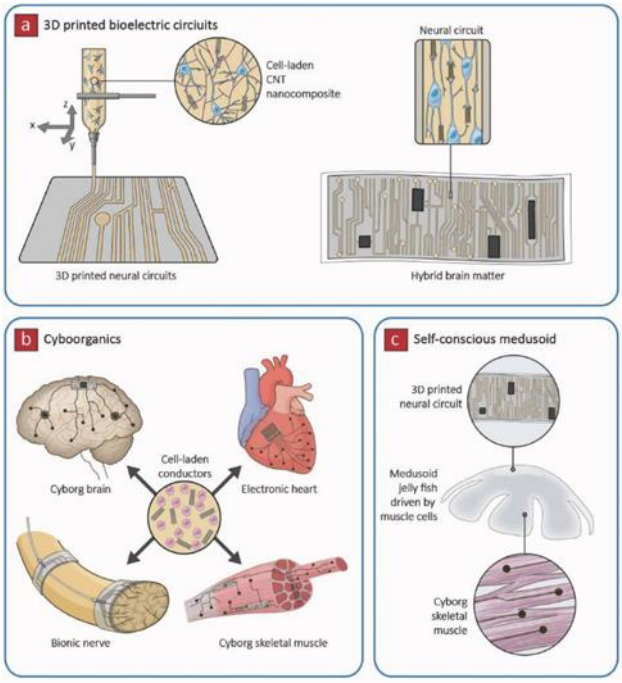

Figure I.12 Future directions: (a) 3D printing of hybrid neural, (b) the potential application of cell-laden conductors in cyborganics, (c) use of 3D-printed neural circuits and cyborg skeletal muscle to generate advanced biorobots (Mehrali et al., 2017).

Liao et al. (2017) Report the fabrication of hybrid mussel-inspired self-adhesive, self-healable, and conductive nanocomposite hydrogels. Hydrogel-based nanocomposites comprising of conductive functionalized single-wall carbon nanotube (FSWCNT), biocompatible polyvinyl alcohol (PVA), and PDA exhibiting excellent and repeatable adhesiveness to the inorganic and organic surface, such as porcine skin for mimicking human skin tissue. Hydrogel-based nanocomposites showed no cytotoxicity and facilitate cell attachment and proliferation, indicating the great promising application of the healable adhesive wearable soft strain sensors with tissue adhesiveness and reliable biocompatibility (Figure I.13).

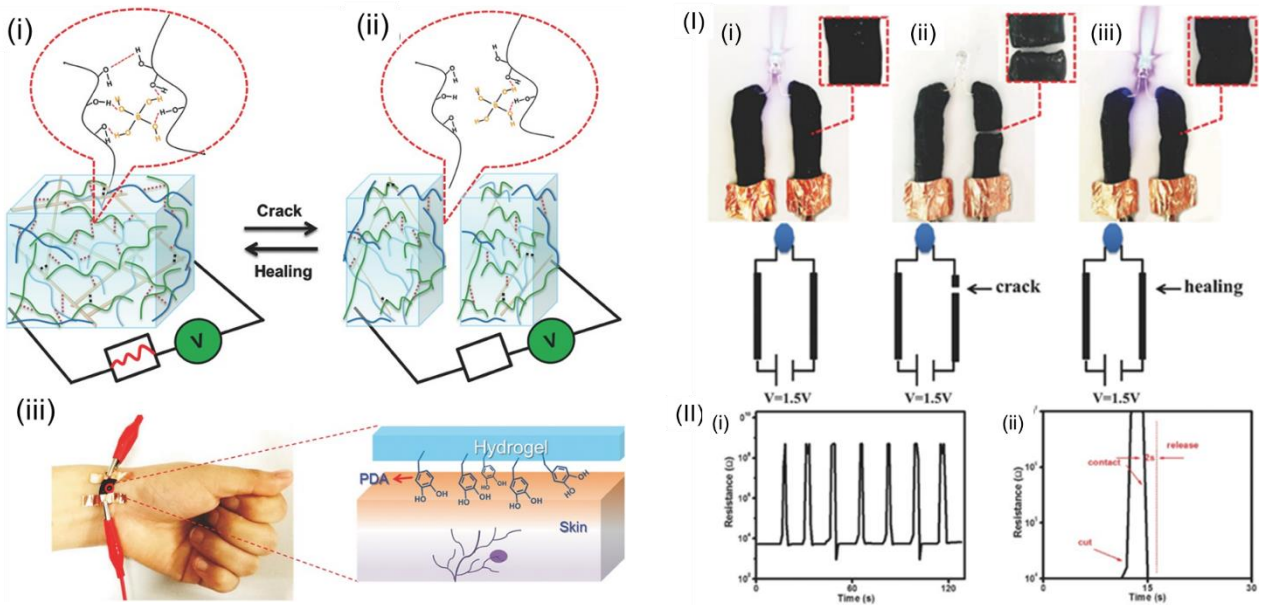

(a) (b)

Figure I.13 Self-healing capability of the conductive PVA-FSWCNT-PDA hydrogel: (a) Schematic representation of the conductive nanocomposite network hydrogels that could be (i,ii) reversibly self-healed, and (i) self-adhered on the wrist during the human–machine interaction and healthcare monitoring, (b) the conductive properties of the PVA-FSWCNT-PDA hydrogel (I) Circuit and cartoon containing self-healing PVA-FSWCNT-PDA hydrogel connected with a blue LED indicator: (i) original, (ii) completely severed (open circuit), and (iii) self-healing. (II) Time evolution of the self-healing process for the conductive PVA-FSWCNT-PDA hydrogel by the real-time resistance measurements: (i) the cutting-healing cycles at the same location and (ii) the magnified self-healing process (Liao et al., 2017).

I.3.2.3 Biological properties

Biological properties of materials are arguably the most important characteristics that ultimately determine their usefulness and biomedical application. Even with superior mechanical and electrical properties, in vivo failure of hydrogels is too often caused by interactions with biological environment. Toxicity and biomaterial/ biological environment are essential biological properties of biomaterials requiring detailed characterization. Incorporation of nanomaterials into hydrogels can significantly improve their biological behavior. For example, Alonci et al., (2018) successfully

developed a nanocomposite poly(amidoamine) hydrogel cross-linked with cystamine. In vitro tests showed that the hydrogel was able to sustain the proliferation of human dermal fibroblasts and to undergo degradation in response to cell-secreted molecules. The material was successfully tested in vivo, in pigs, as a fluid cushion for ESD and demonstrated long-lasting mucosal elevation. The developed injectable hydrogel can solidify in less than 3 minutes upon a supramolecular interaction with type I collagen, which is naturally present in the submucosal layer (Figure I.14).

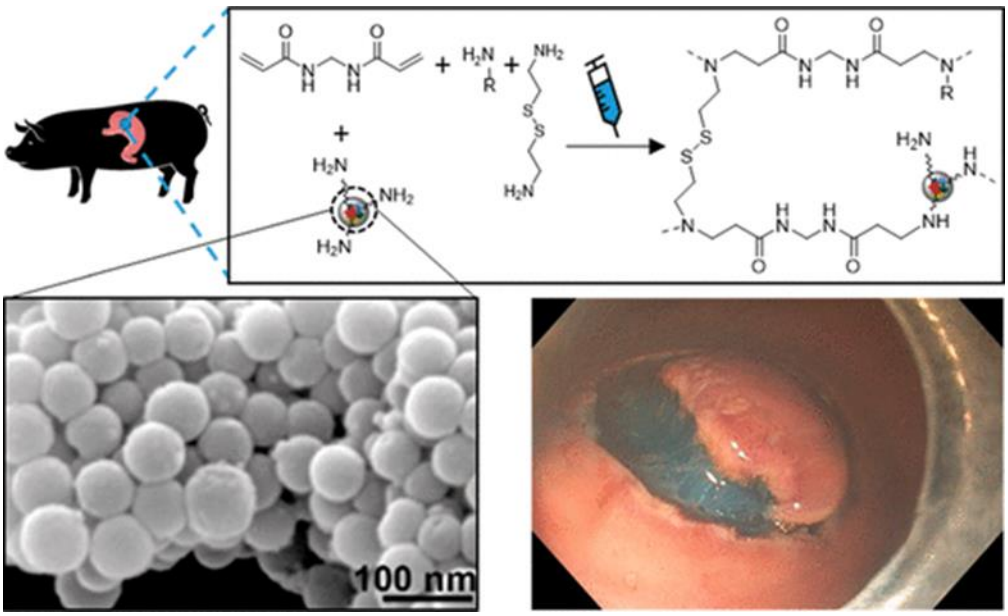

Figure I.14 In vivo gastric endoscopic submucosal dissection. A nanocomposite (silica nanoparticles) hydrogel, injectable, able to quickly (<3 min) jellify forming a solid long-lasting cushion that facilitates en bloc tumor resection (Piantanida et al., 2019).

I.3.2.4 Magnetic properties

One type of remotely controlled stimuli responsiveness is achieved by incorporation of magnetic nanomaterials. These magnetically responsive hydrogel-based nanocomposites have been used for making improved drug delivery systems, magnetic sensors, and diagnostic imaging agents (Figure I.15).

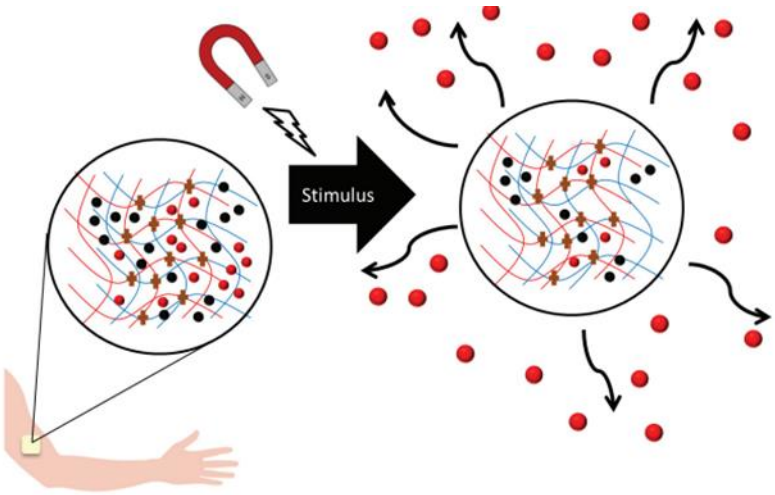

Figure I.15 Schematic representation of drug delivery under external magnetic field. The drug (red spheres) can be loaded in magnetic hydrogels, which can be shaped as patches or injected in vivo (Frachini and Petri, 2019).

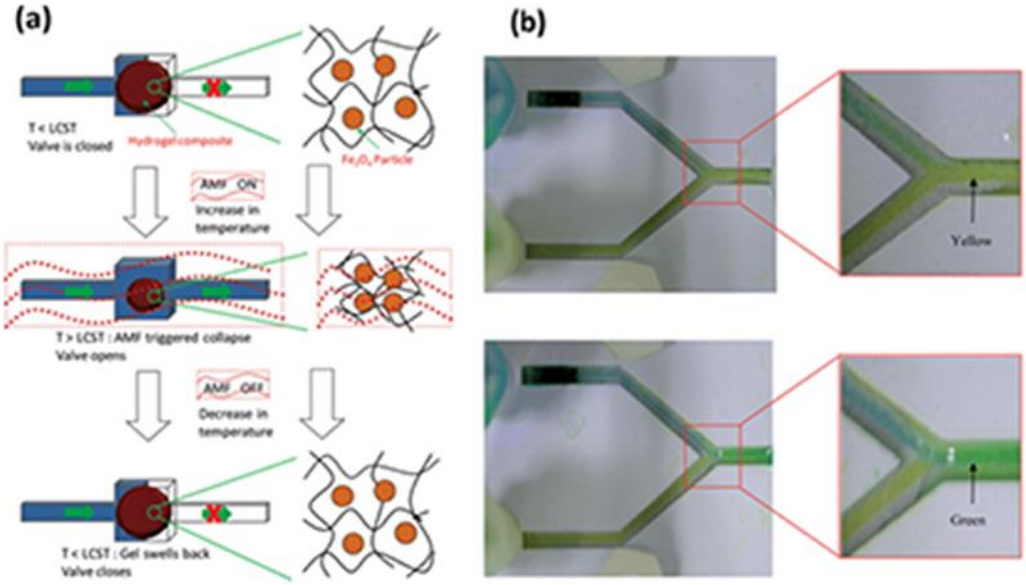

Figure I.16 Stimuli-responsive nanocomposite hydrogels: (a) Schematic of operation of remote-controlled valves with hydrogel-based nanocomposites, (b) alternating the magnetic field results in collapse of the hydrogel, leading to opening or closing of the valve, permitting individual-colored liquid flows (Memic et al., 2015).

To generate magnetically controlled nanocomposite hydrogels, magnetic Fe^3O_4 nanoparticles were incorporated into the NIPAAm hydrogel network (Frimponget al., 2010). This nanocomposite can be used for complex functions such as remote-controlled microfluidic valves. The nanocomposite was

integrated within a microfluidic device at the intersection of the Y-junction, acting as a valve. The collapse and swelling response of the magnetic nanocomposite hydrogel can be triggered with a radio-frequency alternating magnetic field, which permits on-off control of the device flow (Figure I.16).

I.4 Partial conclusion

This literature survey highlights the considerable efforts devoted in the very recent years to the fabrication of advanced soft materials reinforced by nanoparticles. Accurate relationship between structure and properties is fundamental for a reliable design of such new materials. Among all mysterious aspects, the mechanisms of nanofillers reinforcement remain largely misunderstood.

The next chapters will be focused on the mechanics of these materials through the formulation of constitutive models, even if behind the goal will be to provide a more general multiphysics constitutive model mixing the different fascinating phenomena (chemical, physical, mechanical and biological) described in Chapter 1. The developed models will be continuously enriched to provide step by step better predictabilities and understanding of the separate and synergistic effects of key factors that govern the impressive improvements of mechanical properties.

References

Alonci, G., Fiorini, F., Riva, P., Monroy, F., López-Montero, I., Perretta, S., De Cola, L., 2018. Injectable hybrid hydrogels, with cell-responsive degradation, for tumor resection. ACS Applied Bio Materials 1, 1301-1310.

Andrade, F., Roca-Melendres, M.M., Durán-Lara, E.F., Rafael, D., Schwartz Jr, S., 2021. Stimuli-responsive hydrogels for cancer treatment: The role of pH, light, ionic strength and magnetic field. Cancers 13, 1164.

Arrizabalaga, J.H., Smallcomb, M., Abu-Laban, M., Liu, Y., Yeingst, T.J., Dhawan, A., Hayes, D. J., 2022. Ultrasound-responsive hydrogels for on-demand protein release. ACS Applied Bio Materials 5, 3212-3218.

Arslantunali, D., Budak, G., Hasirci, V., 2014. Multiwalled CNT-pHEMA composite conduit for peripheral nerve repair. Journal of Biomedical Materials Research Part A 102, 828-841.

Bach, J.S., Detrez, F., Cherkaoui, M., Cantournet, S., Ku, D.N., Corté, L., 2013. Hydrogel fibers for ACL prosthesis: design and mechanical evaluation of PVA and PVA/UHMWPE fiber constructs. Journal of biomechanics 46, 1463-1470.

Bedoui, F., Blivi, A.S., Fan, B., Kondo, D., 2022. Size effects on physical and mechanical properties of nano-reinforced polymers. Nanocomposites: Preparation, Characterization and Modeling 71-92.

Beldjilali-Labro, M., Garcia Garcia, A., Farhat, F., Bedoui, F., Grosset, J.F., Dufresne, M., Legallais, C., 2018. Biomaterials in tendon and skeletal muscle tissue engineering: current trends and challenges. Materials 11, 1116.

Bouasse, H., Carrière, Z., 1903. Sur les courbes de traction du caoutchouc vulcanisé. Annales de la faculté des sciences de Toulouse 5, 257-283.

Chen, T., Hou, K., Ren, Q., Chen, G., Wei, P., Zhu, M., 2018. Nanoparticle–polymer synergies in nanocomposite hydrogels: from design to application. Macromolecular Rapid Communications 39, 1800337.

Chimene, D., Peak, C.W., Gentry, J.L., Carrow, J. K., Cross, L. M., Mondragon, E., Gaharwar, A. K., 2018. Nanoengineered ionic–covalent entanglement (NICE) bioinks for 3D bioprinting. ACS Applied Materials and Interfaces 10, 9957-9968.

Deng, L., Lu, H., Tu, C., Zhou, T., Cao, W., Gao, C., 2022. A tough synthetic hydrogel with excellent post-loading of drugs for promoting the healing of infected wounds in vivo. Biomaterials Advances 134, 112577.

Ding, H., Zhang, X.N., Zheng, S.Y., Song, Y., Wu, Z.L., Zheng, Q., 2017. Hydrogen bond reinforced poly (1-vinylimidazole-co-acrylic acid) hydrogels with high toughness, fast self-recovery, and dual pH-responsiveness. Polymer 131, 95-103.

Dourado, M.D., Fregolente, P.B., Maciel, M.R.W., Fregolente, L.V., 2021. Screening of hydrogels for water adsorption in biodiesel using crosslinked homopolymers. Chemical Engineering Transactions 86, 1129-1134.

Esmaeili, H., Patino-Guerrero, A., Hasany, M., Ansari, M.O., Memic, A., Dolatshahi-Pirouz, A., Nikkhah, M., 2021. Electroconductive biomaterials for cardiac tissue engineering. Acta Biomaterialia 139, 118-140.

Fox, C.S., Berry, H.A., Pedigo, S., 2020. Development and characterization of calmodulin-based copolymeric hydrogels. Biomacromolecules 21, 2073-2086.

Fragal, E.H., Fragal, V.H., Silva, E.P., Paulino, A.T., da Silva Filho, E.C., Maurício, M. R., Muniz, E.C., 2022. Magnetic-responsive polysaccharide hydrogels as smart biomaterials: Synthesis, properties, and biomedical applications. Carbohydrate Polymers 119665.

Frachini, E.C., Petri, D.F., 2019. Magneto-responsive hydrogels: preparation, characterization, biotechnological and environmental applications. Journal of the Brazilian Chemical Society 30, 2010-2028.

Frimpong, R.A., Hilt, J.Z., 2010. Magnetic nanoparticles in biomedicine: synthesis, functionalization and applications. Nanomedicine 5, 1401-1414.

Gao, G., Du, G., Sun, Y., Fu, J., 2015. Self-healable, tough, and ultrastretchable nanocomposite hydrogels based on reversible polyacrylamide/montmorillonite adsorption. ACS Applied Materials and Interfaces 7, 5029-5037.

Han, I.K., Song, K.I., Jung, S.M., Jo, Y., Kwon, J., Chung, T., Kim, Y. S., 2022. Electroconductive, adhesive, non-swelling, and viscoelastic hydrogels for bioelectronics. Advanced Materials, 2203431.

Haraguchi, K., Farnworth, R., Ohbayashi, A., Takehisa, T., 2003. Compositional effects on mechanical properties of nanocomposite hydrogels composed of poly (N, N-dimethylacrylamide) and clay. Macromolecules 36, 5732-5741.

Haraguchi, K., Li, H.J., 2006. Mechanical properties and structure of polymer− clay nanocomposite gels with high clay content. Macromolecules 39, 1898-1905.

Haraguchi, K., 2007. Nanocomposite hydrogels. Current Opinion in Solid State and Materials Science 11, 47-54.

Holt, W., 1931. Behaviour of rubber under repeated stresses. Industrial and Engineering Chemistry 23, 1471–1475.

Hu, Y., Gao, S., Lu, H., Ying, J.Y., 2022. Acid-resistant and physiological PH-responsive DNA hydrogel composed of a-motif and i-motif toward oral insulin delivery. Journal of the American Chemical Society 144, 5461-5470.

Jiang, H., Zhang, G., Feng, X., Liu, H., Li, F., Wang, M., Li, H., 2017. Room-temperature self-healing tough nanocomposite hydrogel crosslinked by zirconium hydroxide nanoparticles. Composites Science and Technology 140, 54-62.

Jiang, Z., Tan, M.L., Taheri, M., Yan, Q., Tsuzuki, T., Gardiner, M.G., Connal, L. A., 2020. Strong, self-healable, and recyclable visible-light-responsive hydrogel actuators. Angewandte Chemie 132, 7115-7122.

Jiao, Q., Cao, L., Zhao, Z., Zhang, H., Li, J., Wei, Y., 2021. Zwitterionic hydrogel with high transparency, ultrastretchability, and remarkable freezing resistance for wearable strain sensors. Biomacromolecules 22, 1220-1230.

Koetting, M.C., Peters, J.T., Steichen, S.D., Peppas, N.A., 2015. Stimulus-responsive hydrogels: Theory, modern advances, and applications. Materials Science and Engineering: R: Reports 93, 1-49.

Liao, M., Wan, P., Wen, J., Gong, M., Wu, X., Wang, Y., Zhang, L., 2017. Wearable, healable, and adhesive epidermal sensors assembled from mussel-inspired conductive hybrid hydrogel framework. Advanced Functional Materials 27, 1703852.

Li, X., Zhao, Y., Li, D., Zhang, G., Long, S., Wang, H., 2017. Hybrid dual crosslinked polyacrylic acid hydrogels with ultrahigh mechanical strength, toughness and self-healing properties via soaking salt solution. Polymer 121, 55-63.

Li, X., Yang, Q., Zhao, Y., Long, S., Zheng, J., 2017. Dual physically crosslinked double network hydrogels with high toughness and self-healing properties. Soft Matter 13, 911-920.

Li, Y., Liu, C., Lv, X., Sun, S., 2021. A highly sensitive strain sensor based on a silica@ polyaniline core–shell particle reinforced hydrogel with excellent flexibility, stretchability, toughness and conductivity. Soft Matter 17, 2142-2150.

Long, S., Xie, C., Lu, X., 2022. Natural polymer-based adhesive hydrogel for biomedical applications. Biosurface and Biotribology.

Mehrali, M., Thakur, A., Pennisi, C.P., Talebian, S., Arpanaei, A., Nikkhah, M., Dolatshahi-Pirouz, A., 2017. Nanoreinforced hydrogels for tissue engineering: biomaterials that are compatible with load-bearing and electroactive tissues. Advanced Materials 29, 1603612.

Memic, A., Alhadrami, H.A., Hussain, M.A., Aldhahri, M., Al Nowaiser, F., Al-Hazmi, F., Khademhosseini, A., 2015. Hydrogels 2.0: improved properties with nanomaterial composites for biomedical applications. Biomedical Materials 11, 014104.

Min, J.H., Patel, M., Koh, W.G., 2018. Incorporation of conductive materials into hydrogels for tissue engineering applications. Polymers 10, 1078.

Molina, M., Asadian-Birjand, M., Balach, J., Bergueiro, J., Miceli, E., Calderón, M., 2015. Stimuli-responsive nanogel composites and their application in nanomedicine. Chemical Society Reviews 44(17), 6161-6186.

Mullins, L., 1948. Effect of stretching on the properties of rubber. Rubber Chemistry and Technology 21, 281-300.

Mullins, L., 1950. Thixotropic Behavior of Carbon Black in Rubber. Rubber Chemistry and Technology 23, 733-743.

Mullins, L., 1969. Softening of rubber by deformation. Rubber Chemistry and Technology 42, 339-362.

Mullins, L., Tobin, N., 1957. Theoretical model for the elastic behavior of filler-reinforced vulcanized rubbers. Rubber Chemistry and Technology 30, 551-571.

Mullins, L., Tobin, N., 1965. Stress softening in rubber vulcanizates. Part I. Use of a strain amplification factor to describe the elastic behavior of filler-reinforced vulcanized rubber. Journal of Applied Polymer Science 9, 2993–3009

Nguyen, M.K., Huynh, C.T., Gao, G.H., Kim, J.H., Chae, S.Y., Lee, K. C., Lee, D.S., 2011. Biodegradable oligo (amidoamine/β-amino ester) hydrogels for controlled insulin delivery. Soft Matter 7, 2994-3001.

Piantanida, E., Alonci, G., Bertucci, A., De Cola, L., 2019. Design of nanocomposite injectable hydrogels for minimally invasive surgery. Accounts of Chemical Research 52, 2101-2112.

Pita-López, M.L., Fletes-Vargas, G., Espinosa-Andrews, H., Rodriguez-Rodriguez, R., 2021. Physically cross-linked chitosan-based hydrogels for tissue engineering applications: A state-of-the-art review. European Polymer Journal 145, 110176.

Reis, A.C., Dos Santos, L.V., Santos, K.R., Lima-Tenório, M.K., Paludo, K.S., Maurício, M.R., Tenório-Neto, E.T., 2022. Chemically crosslinked guar gum hydrogels: An investigation on the water transport and its relationship with hydrocortisone release. International Journal of Pharmaceutics 617, 121626.

Rungrod, A., Kapanya, A., Punyodom, W., Molloy, R., Mahomed, A., Somsunan, R., 2022. Synthesis and characterization of semi-IPN hydrogels composed of sodium 2-acrylamido-2-methylpropanesulfonate and poly (ε-caprolactone) diol for controlled drug delivery. European Polymer Journal 164, 110978.

Schwartz, A., 1907. "Flexibles", with notes on the testing of rubber. Journal of the Institution of Electrical Engineers 39, 31-100.

Shao, C., Chang, H., Wang, M., Xu, F., Yang, J., 2017. High-strength, tough, and self-healing nanocomposite physical hydrogels based on the synergistic effects of dynamic hydrogen bond and dual coordination bonds. ACS Applied Materials and Interfaces 9, 28305-28318.

Shedd, J., Ingersol, R., 1904. The Elastic Modulus and Elastic Limit of Rubber and their Relation to Change of Temperature. Physical Review 19, 107-116.

Shojaeiarani, J., Shirzadifar, A., Bajwa, D.S., 2021. Robust and porous 3D-printed multifunctional hydrogels for efficient removal of cationic and anionic dyes from aqueous solution. Microporous and Mesoporous Materials 327, 111382.

Thoniyot, P., Tan, M.J., Karim, A.A., Young, D.J., Loh, X.J., 2015. Nanoparticle–hydrogel composites: Concept, design, and applications of these promising, multi-functional materials. Advanced Science 2, 1400010.

Vedadghavami, A., Minooei, F., Mohammadi, M.H., Khetani, S., Kolahchi, A.R., Mashayekhan, S., Sanati-Nezhad, A., 2017. Manufacturing of hydrogel biomaterials with controlled mechanical properties for tissue engineering applications. Acta Biomaterialia 62, 42-63.

Wen, N., Jiang, B., Wang, X., Shang, Z., Jiang, D., Zhang, L., Guo, Z., 2020. Overview of polyvinyl alcohol nanocomposite hydrogels for electro-skin, actuator, supercapacitor and fuel cell. The Chemical Record 20, 773-792.

Xia, Y., Gao, S., Yu, R., Zeng, Z., He, H., Zhou, X., Wang, S., 2021. Near-infrared light induced dynamic structural color change of amorphous photonic hydrogel. ACS Applied Polymer Materials 3, 757-764.

Xu, C., Li, B., Wang, X., 2021. A comparison study on the magneto-responsive properties and swelling behaviors of a polyacrylamide-based hydrogel incorporating with magnetic particles. International Journal of Molecular Sciences 22, 12342.

Xu, C., Sun, Y., Zhang, J., Xu, W., Tian, H., 2022. Adaptable and wearable thermocell based on stretchable hydrogel for body heat harvesting. Advanced Energy Materials 2201542.

Yang, Z., Chen, L., McClements, D.J., Qiu, C., Li, C., Zhang, Z., Jin, Z., 2022. Stimulus-responsive hydrogels in food science: A review. Food Hydrocolloids 124, 107218.

Zhang, D., Ren, B., Zhang, Y., Xu, L., Huang, Q., He, Y., Zheng, J., 2020. From design to applications of stimuli-responsive hydrogel strain sensors. Journal of Materials Chemistry B 8, 3171-3191.

Chapter II

A micromechanics-based model for visco-super-elastic hydrogel-based nanocomposites

CHAPTER II

A micromechanics-based model for visco-super-elastic hydrogel-based nanocomposites[1]

This chapter presents a micromechanics-based model that constitutively relates internal network physics of hydrogel-based nanocomposites with their visco-super-elastic mechanics. The model is based on the Eshelby inclusion theory combined to the concept of cubic material volume to take into account the effective role of inorganic nanoparticles on the finite-strain response of hydrogels. Dynamic bonds between hydrogel chains and nanoparticles allow to describe the impressive time-dependent properties of hydrogel-based nanocomposites such as rate-dependent extreme stretchability, strong hysteresis upon stretching-retraction and room temperature self-healing facility. The model is compared to a few available experimental data of a variety of hydrogel-nanofiller material systems in terms of stress-strain response till failure, hysteresis, continuous relaxation and self-healing. The effects on the hydrogel behavior of loading conditions (strain rate and strain level) and internal network structures (due to variations in reinforcing elements and cross-linker amounts) are examined. The micromechanical model simulations are found in excellent agreement with experimental observations showing the relevance of the proposed approach. The mechanisms of nanofillers reinforcement and failure are discussed with respect to the model. The room temperature self-healing characteristics of hydrogel systems are discussed in connection to loading history and nanostructure. To further illustrate the model capabilities, the behavior of hydrogel systems is finally treated under different biaxial loading conditions.

Keywords: *Hydrogel-based nanocomposites; Micromechanical modeling; Extreme stretchability; History-dependent effects; Self-healing.*

[1] This chapter is based on the following paper: Saadedine, M., Zaïri, F., Ouali, N., Tamoud, A., Mesbah, A., 2021. A micromechanics-based model for visco-super-elastic hydrogel-based nanocomposites. International Journal of Plasticity 144, 103042.

II.1 Partial introduction

Amongst the new cohort of advanced materials, hydrogel-based nanocomposites, designed by incorporating nano-sized second phase into hydrogels, have fascinating properties. They have very recently attracted a lot of attention due to the new extraordinary opportunities that such sophisticated and multifunctional materials offer in a wide range of domains including aerospace, 3D printing, waste-water treatment, biomedical engineering (drug delivery and tissue engineering), sensors, actuators and energy storage (Lima-Tenorio et al., 2015; Merino et al., 2015; Bhattacharya and Samanta, 2016; Farahani et al., 2016; Yang et al., 2016; Thakur et al., 2017a, 2017b; Zhai et al., 2017; Liu et al., 2019; Deng et al., 2019; Guo et al., 2019; Xu et al., 2019; Zhang et al., 2019).

While traditional (organically crosslinked) hydrogels have poor mechanical performances (e.g. low fracture toughness and limited ductility), this new class of nanocomposites is extremely resilient and extremely stretchable with an elongation than can exceed 3000%. Very recent studies have illustrated impressive improvements of mechanical properties, in addition to extreme stretchability, such as high toughness and high mechanical strength (Sun et al., 2012; Shi et al., 2015; Chen et al., 2017; Liu et al., 2019). The reinforcing effect of nanoparticles is attributed to several factors such as hydrogel matrix properties, nature (and amount) of nanoparticles and strength of interactions. Nanofillers considerably improve the structural stability of the hydrogels due to the occurrence of multiple specific interactions between the polar surface of the charges and hydrophilic chains such as hydrogen bonds, van der Waals interactions and electrostatic interactions, to achieve better chemical, electrical, mechanical and biological properties (Sarvestani et al., 2008; Schexnailder and Schmidt, 2009; Kumar et al., 2014). These smart and adaptive materials combine the advantage of the nano-scale reinforcement and the multiphysics (chemical, physical, mechanical and biological) properties of hydrogels including biocompatibility (along with some similarities to biological tissues), stimulating responsiveness,

adsorption performance and facile room temperature self-healing (by restoring initial microstructure and mechanical strength).

Whereas considerable efforts have been devoted to elaboration and characterization of hydrogel-filler material systems, the mechanisms of nanofillers reinforcement remain largely misunderstood. Behind the basic inelastic features illustrated in Figure I.1, a better understanding of the structure-property relationship for such new material systems is of prime importance in order to provide detailed information for their reliable design considering a rigorous set of their various specific characteristics: extreme stretchability and self-healing facility along with a strong viscous consistency. As a meaningful prerequisite of advanced applications of such new materials, the formulation of constitutive models is needed. Such tools would provide a better understanding of the separate and synergistic effects of key factors that govern the impressive improvements of mechanical properties. An exhaustive literature survey shows that the constitutive modeling of hydrogels is rare (Long et al., 2014; Guo et al., 2016; Liu et al., 2016; Wang and Gao, 2016; Mao et al., 2107; Shao et al., 2017; Wang et al., 2017; Vernerey et al., 2017, 2018; Vernerey, 2018; Yu et al., 2018; Kulcu, 2019; Morovati and Dargazany, 2019; Drozdov and Christiansen, 2018, 2020; Lin et al., 2020; Zhu and Zhong, 2020; Xiao et al., 2021). More specifically Morovati and Dargazany (2019) proposed a constitutive model based on the network decomposition along with the detachment mechanism to capture the stress-softening in double network hydrogels. Liu et al. (2016), Kulcu (2019) and Xiao et al. (2021) proposed also inelastic constitutive models for double network hydrogels while Wang and Gao (2016) and Wang et al. (2017) paid attention to the networks crosslinked by nanoparticles. The strong viscous consistency of hydrogels may be represented by using either phenomenological or physically-based approaches. The latter seems more attractive to provide a proper description of the underlying microstructure phenomena in the aim of controlling them (Dargazany et al., 2014; Li et al., 2016; Yang and Li, 2016; Guo et al., 2018; Zhou et al., 2018; Mahjoubi et al., 2019;

Xiang et al., 2019; Guo and Zaïri, 2020, 2021). For example, Mao et al. (2017) developed a constitutive model to describe inelastic behavior and stress-softening in double network hydrogels in which the inelastic damage caused by the rupture of ionic bonds is introduced. The self-healing behavior is also an important feature to control by tailoring the microstructure. Intensive efforts have been done to the thermally-induced strain recovery prediction of more conventional amorphous networks (Su and Peng, 2018; Shen et al., 2019; Cherief et al., 2020; Dai et al., 2020) in relation to previous thermo-mechanical history and heating conditions in terms of recovery temperature and heating rate. Actually, hydrogels are room-temperature self-healable materials and this feature has been considered in a very few constitutive models (Long et al., 2014; Vernerey et al., 2017; Wang et al., 2017; Yu et al., 2018; Lin et al., 2020). Long et al. (2014) developed a rate-dependent phenomenological model for dual cross-linked self-healing hydrogels. Vernerey et al. (2017) provided latter a more direct connection between single chain and macroscopic mechanics. Wang et al. (2017) developed a polymer-network based theory to capture the response of self-healable nanocomposite hydrogels taking into account the particle concentration and chain length distribution. However, the chain-particle interaction has been highly simplified. Lu et al. (2020) and Lin et al. (2020) developed constitutive models, based on the eight-chain model and on a Neo-Hookean formulation, respectively, in which association/dissociation of chains were incorporated to capture the recovery behavior of different hydrogel types. The constitutive models are able to describe the rate-dependent tensile response but the presence of particles is not taken into account.

Despite the important advance accomplished by these models, they cannot connect the nanostructure to the overall recovery behavior of hydrogel-based nanocomposites. A rigorous constitutive representation of the nanofiller-hydrogel material system, including explicit active interactions between nanfillers and hydrogel matrix, would allow to propose physically

consistent explanations of the reinforcement mechanisms in connection to the nonlinear material response (Zaïri et al., 2011) and the room-temperature self-healing facility.

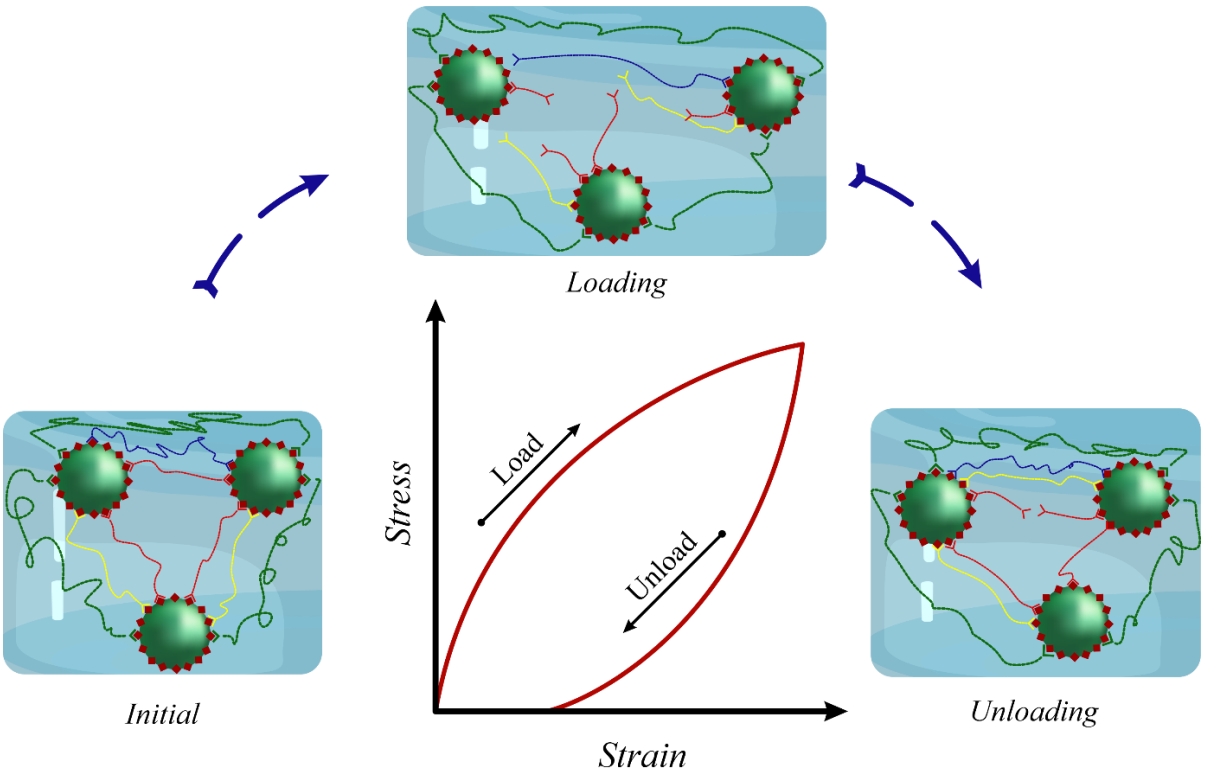

Figure II.1 Dynamic bonds in hydrogel-filler material system upon a stretching-retraction cycle. Each color is associated to a group of chains according to their lengths.

In this regards, only micromechanics-based approaches allow to propose a framework avoiding (or at least limiting) the arbitrary inclusion of heuristic parameters. Such a development would offer a way to gain a better understanding of the reinforcing effect of nanoparticles on the overall properties and to provide detailed information for their design. A constitutive representation that

considers as well history-dependent effects and local matrix-nanoparticle interaction has not yet been developed.

The objective of this chapter is to constitutively correlate the behavior of visco-super-elastic hydrogel-based nanocomposites to their internal network structures in terms of hydrogel matrix and inorganic nanoparticles properties. We present a model based on the Eshelby inclusion theory and the micromechanics framework using the concept of cubic material volume to account for the effective role of nanoparticles on the nonlinear and finite-strain macro-behavior of hydrogel-based nanocomposites. The hydrogel-nanofiller material system is representatively regarded as a cubic unit cell containing nine particles. A central nanoparticle connects eight nanoparticles placed at the cube vertices via a number of hydrogel chains. The model explicitly considers the chains network with dynamic reversible detachable/re-attachable mechanisms of bonds to coherently capture the rate-dependent extreme stretchability and some inelastic features including strong hysteresis upon stretching-retraction and continuous relaxation. A quantitative evaluation of our model is presented by comparisons to a few available experimental data of a variety of hydrogel-nanofiller material systems.

The model is used to discuss some important aspects of the mechanisms of nanofillers reinforcement, failure and room temperature self-healing facility.

The chapter is organized as follows. The micromechanical model is presented in Section II.2 Section II.3 presents and discusses the model results especially regarding the reinforcing effect of inorganic nanoparticles on the visco-super-elastic response of hydrogels. Concluding remarks are finally given in Section II.4.

The following notation is used throughout the text. Tensors and vectors are denoted by normal boldfaced letters and italicized boldfaced letters, respectively, while scalars and individual components of vectors and tensors are denoted by normal italicized letters.

II.2 Model

II.2.1 Cubic material volume

When nanoparticles are embedded into a hydrogel medium, the nano-sized discrete second phase acts as anchoring (crosslinking) points for hydrogel chains and strengthens the chains network (Haraguchi et al., 2002; Liu et al., 2019). A multiscale approach starting from the nanostructure is then required to represent the material system.

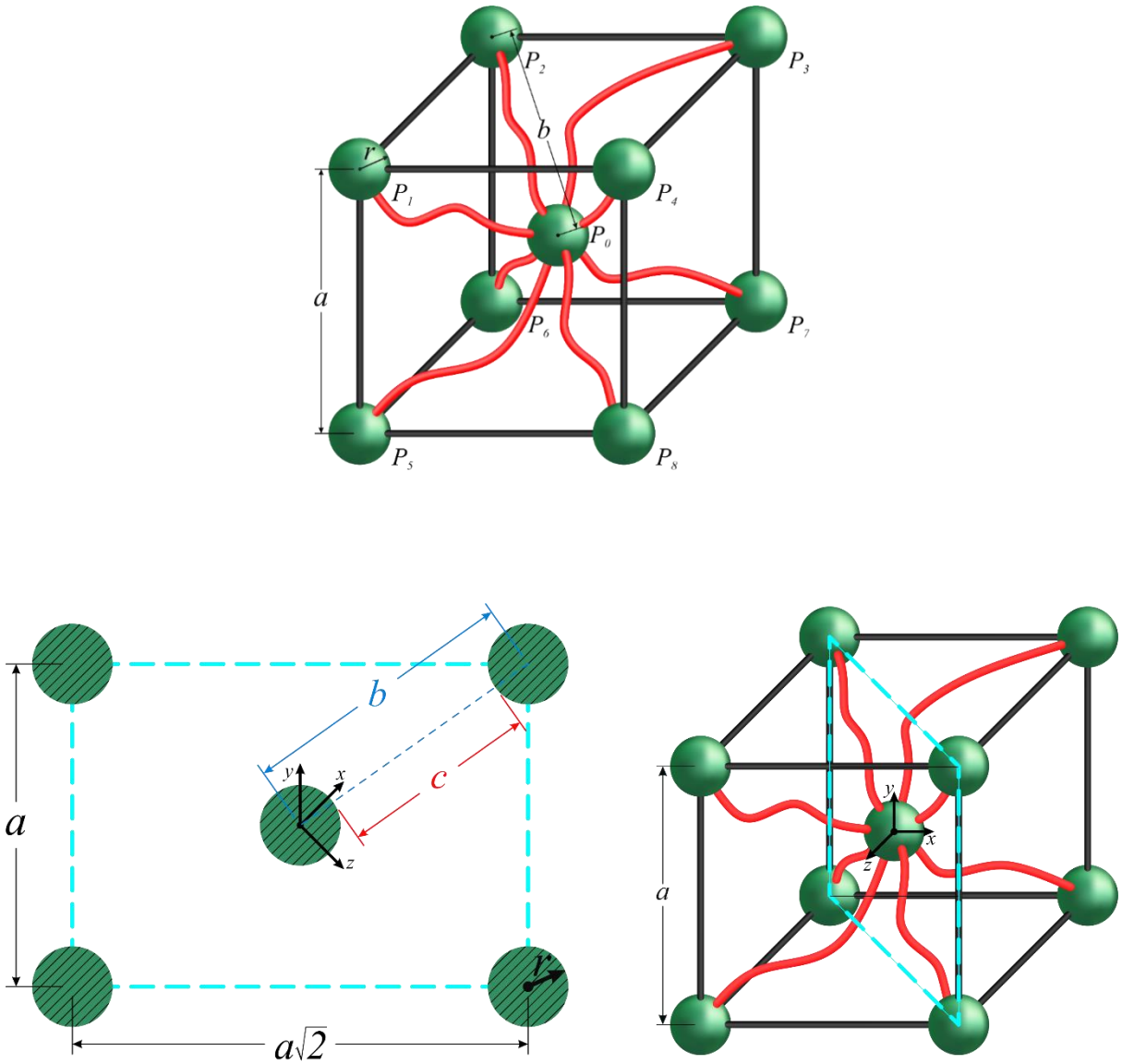

Figure II.2 Unit cell and corresponding geometric setting.

Figure II.2 presents the representative volume element used to derive the model. It arises from the eight-chain cubic material volume of Arruda and Boyce (1993) in which nine nanoparticles are inserted. A central nanoparticle P_0 connects eight nanoparticles (P_1 to P_8) placed at the cube vertices via the eight chains. The hydrogel chains network will be characterized by the mean number of segments in a chain N (mean chain length) and the mean chain density n.

The macroscopic free energy $\bar{\psi}$ from which the stress-strain relationship is obtained may be expressed as a function of the chain free energy ψ_{chain} and the free energy of the nanoparticles ψ_p:

$$\bar{\psi} = \frac{8(b-2r)}{V}\psi_{chain} + \phi\psi_p \tag{II.1}$$

where b is the center-to-center distance between the central nanoparticle and a neighboring nanoparticle, r is the nanoparticle radius, V is the cubic unit cell volume and ϕ is the volume fraction of nanoparticles.

The quantity ψ_{chain} being an energy density per unit chain length, it may be expressed as a function of the strain energy density per unit volume of the hydrogel matrix ψ_m:

$$\psi_{chain} = \frac{V}{8b}\psi_m \tag{II.2}$$

Eq. (II.1) can be re-written as follows:

$$\bar{\psi} = (1-2\rho)\psi_m + \phi\psi_p \tag{II.3}$$

with $\rho = r/b$.

With increasing amount of nanoparticles, the distance between them decreases. The volume fraction of nanoparticles ϕ is defined as the ratio between the volume of domains Ω_p occupied

by the nanoparticles in the cubic unit cell and the total volume V. Since each of the eight nanoparticles P_1 to P_8 occupies a volume of $1/8V_p$ and the central nanoparticle P_0 occupies a volume of V_p, the volume fraction of nanoparticles is given by:

$$\phi = \frac{2V_p}{a^3} = \sqrt{3}\pi\rho^3 \tag{II.4}$$

where $V_p = 4/3\pi r^3$ is the nanoparticle volume and $a = 2b/\sqrt{3}$ is the cube length.

II.2.2 Constitutive equations for the two phases

The proposed multiscale model satisfies the continuum mechanics rules for which the deformation gradient tensor $\mathbf{F}$ is a key quantity to define the kinematics of a continuum body with $J = \det(\mathbf{F})$ the Jacobian. Let us define the tensors $\bar{\mathbf{F}}$, $\mathbf{F}_m$ and $\mathbf{F}_p$ the deformation gradients of the hydrogel-nanofiller material system, of the hydrogel matrix and of the nanoparticles, respectively. Each constitutive phase is supposed to be an isotropic and homogeneous medium with the stiffness tensors $\mathbf{K}_m$ and $\mathbf{K}_p$ defined with their respective shear moduli $\mu_m = nk_BT$ (k_B is the Boltzmann's constant and T is the absolute temperature) and μ_p, and their respective bulk moduli K_m and K_p.

II.2.2.1 Hydrogel matrix

As shown in Figure II.2, the chain end-to-end vector $\boldsymbol{c}$ is defined, in the Cartesian coordinate system, by:

$$\boldsymbol{c} = \frac{b-2r}{\sqrt{3}}\left(\lambda_{m\_1}\boldsymbol{x} + \lambda_{m\_2}\boldsymbol{y} + \lambda_{m\_3}\boldsymbol{z}\right) \tag{II.5}$$

where λ_{m_1}, λ_{m_2} and λ_{m_3} are the principal stretches of the hydrogel matrix.

The vector $\boldsymbol{c}$ may be also defined as follows:

$$\boldsymbol{c} = \boldsymbol{b} - 2\boldsymbol{r} \tag{II.6}$$

in which $\boldsymbol{b}$ and $\boldsymbol{r}$ are vectors given, in the Cartesian coordinate system, by:

$$\boldsymbol{b} = \frac{b}{\sqrt{3}}\left(\bar{\lambda}_1\boldsymbol{x} + \bar{\lambda}_2\boldsymbol{y} + \bar{\lambda}_3\boldsymbol{z}\right) \text{ and } \boldsymbol{r} = \frac{r}{\sqrt{3}}\left(\lambda_{p\_1}\boldsymbol{x} + \lambda_{p\_2}\boldsymbol{y} + \lambda_{p\_3}\boldsymbol{z}\right) \tag{II.7}$$

where $\bar{\lambda}_1$, $\bar{\lambda}_2$ and $\bar{\lambda}_3$ are the principal stretches applied at the macro-level and, λ_{p_1}, λ_{p_2} and λ_{p_3} are the principal stretches of the nanoparticles $\mathbf{F}_p$.

Combining Eqs. (II.5), (II.6) and (II.7), the micro-macro transition is realized. The obtained deformation gradient tensor of the hydrogel matrix $\mathbf{F}_m$ may be expressed as follows:

$$\mathbf{F}_m = \frac{1}{1-2\rho}\left(\bar{\mathbf{F}} - 2\rho\mathbf{F}_p\right) \tag{II.8}$$

The deformation gradient tensor $\mathbf{F}_m$ may be multiplicatively split into a volumetric part $\mathbf{F}_{m\_\mathrm{vol}}$ and an isochoric part $\mathbf{F}_{m\_\mathrm{iso}}$ as:

$$\mathbf{F}_m = \mathbf{F}_{m\_\mathrm{vol}}.\mathbf{F}_{m\_\mathrm{iso}} \tag{II.9}$$

For an isotropic swelling, the two tensors are given by:

$$\mathbf{F}_{m\_\mathrm{vol}} = J_m^{1/3}\mathbf{I} \text{ and } \mathbf{F}_{m\_\mathrm{iso}} = J_m^{-1/3}\mathbf{F}_m \tag{II.10}$$

where $\mathbf{I}$ is the unit tensor.

The viscoelasticity in the material medium is based on the multiplicative decomposition concept of the deformation (Li et al., 2017). The deformation gradient tensor of the hydrogel matrix $\mathbf{F}_{m\_\mathrm{iso}}$ is then further multiplicatively split into an elastic part $\mathbf{F}^e_{m\_\mathrm{iso}}$ and a viscous part $\mathbf{F}^v_{m\_\mathrm{iso}}$ as :

$$\mathbf{F}_{m\_\mathrm{iso}} = \mathbf{F}^e_{m\_\mathrm{iso}}.\mathbf{F}^v_{m\_\mathrm{iso}} \tag{II.11}$$

The velocity gradient tensor of the hydrogel matrix $\mathbf{L}_{m\_\mathrm{iso}} = \dot{\mathbf{F}}_{m\_\mathrm{iso}}.\mathbf{F}_{m\_\mathrm{iso}}^{-1}$ is expressed as:

$$\mathbf{L}_{m\_\mathrm{iso}} = \mathbf{D}_{m\_\mathrm{iso}} + \mathbf{W}_{m\_\mathrm{iso}} \tag{II.12}$$

in which $\mathbf{D}_{m\_\mathrm{iso}}$ is the stretching rate tensor (symmetric part) and $\mathbf{W}_{m\_\mathrm{iso}}$ is the spin tensor (skew-symmetric part):

$$\mathbf{D}_{m\_\mathrm{iso}} = \frac{1}{2}\left(\mathbf{L}_{m\_\mathrm{iso}} + \mathbf{L}_{m\_\mathrm{iso}}^{T}\right) \text{ and } \mathbf{W}_{m\_\mathrm{iso}} = \frac{1}{2}\left(\mathbf{L}_{m\_\mathrm{iso}} - \mathbf{L}_{m\_\mathrm{iso}}^{T}\right) \tag{II.13}$$

Using the irrotationality hypothesis for the viscous flow (Gurtin and Anand, 2005), the viscous spin tensor is null $\mathbf{W}_{m\_\mathrm{iso}} = \mathbf{0}$ and the viscous deformation gradient tensor $\mathbf{F}_{m\_\mathrm{iso}}^{v}$ is governed by a differential equation of the general form:

$$\dot{\mathbf{F}}_{m\_\mathrm{iso}}^{v} = \mathbf{F}_{m\_\mathrm{iso}}^{e^{-1}}.\mathbf{D}_{m}^{v}.\mathbf{F}_{m\_\mathrm{iso}} \tag{II.14}$$

in which $\mathbf{D}_{m}^{v}$ is the viscous stretching rate tensor of the hydrogel matrix given by the following flow rule:

$$\mathbf{D}_{m}^{v} = \dot{\gamma}_{m}^{v}\frac{\boldsymbol{\sigma}_{m\_\mathrm{iso}}}{\left\|\boldsymbol{\sigma}_{m}\right\|} \tag{II.15}$$

where $\dot{\gamma}_{m}^{v}$ is the accumulated viscous strain rate, $\boldsymbol{\sigma}_{m\_\mathrm{iso}}$ is the isochoric part of the Cauchy stress tensor $\boldsymbol{\sigma}_{m}$ and $\left\|\boldsymbol{\sigma}_{m}\right\|$ is the effective stress expressed by the Frobenius norm:

$$\boldsymbol{\sigma}_{m\_\mathrm{iso}} = \boldsymbol{\sigma}_{m} - 1/3\,\mathrm{trace}\left(\boldsymbol{\sigma}_{m}\right)\mathbf{I} \text{ and } \left\|\boldsymbol{\sigma}_{m}\right\| = \sqrt{\mathrm{trace}\left(\boldsymbol{\sigma}_{m\_\mathrm{iso}}.\boldsymbol{\sigma}_{m\_\mathrm{iso}}^{T}\right)} \tag{II.16}$$

The accumulated viscous strain rate $\dot{\gamma}_{m}^{v}$ is expressed using a Bergstrom and Boyce (1998) formulation:

$$\dot{\gamma}_m^v = \frac{k_v}{\left(\sqrt{I_{1m}^v/3}-1\right)^{\alpha}}\left\|\boldsymbol{\sigma}_m\right\| \tag{II.17}$$

where $I_{1m}^v = \mathrm{trace}\left(\boldsymbol{\varepsilon}_{m\_\mathrm{iso}}^v.\boldsymbol{\varepsilon}_{m\_\mathrm{iso}}^{v^T}\right)$ is the first invariant of the viscous part of the isochoric Hencky strain tensor $\boldsymbol{\varepsilon}_{m\_\mathrm{iso}} = \ln \mathbf{F}_{m\_\mathrm{iso}}$, k_v is the chains relaxation parameter and α is the stretch-dependency parameter.

The free energy of the hydrogel matrix ψ_m is additively split into a volumetric part ψ_{m_vol} and an isochoric part ψ_{m_iso} as:

$$\psi_m = \psi_{m\_\mathrm{vol}}\left(\varepsilon_{m\_\mathrm{vol}}\right) + \psi_{m\_\mathrm{iso}}\left(\mathbf{F}_{m\_\mathrm{iso}}^e\right) \tag{II.18}$$

The volumetric free energy of the hydrogel matrix ψ_{m_vol} is a function of the Hencky volumetric strain $\varepsilon_{m\_\mathrm{vol}} = \ln J_m$ (Holzapfel and Simo, 1996):

$$\psi_{m\_\mathrm{vol}} = \frac{1}{4}K_m\left(\exp\left(2\varepsilon_{m\_\mathrm{vol}}\right)-1-2\varepsilon_{m\_\mathrm{vol}}\right) \tag{II.19}$$

The isochoric free energy of the hydrogel matrix ψ_{m_iso} is expressed as (Arruda and Boyce, 1993):

$$\psi_{m\_\mathrm{iso}} = \frac{n(t)k_\mathrm{B}T}{6}\int_{I_{1m0}^e}^{I_{1m}^e}\mathcal{L}^{-1}\left(\sqrt{\frac{I_{1m}^e}{3N(t)}}\right)\sqrt{\frac{3N(t)}{I_{1m}^e}}dI_{1m}^e \tag{II.20}$$

where $I_{1m}^e = \mathrm{trace}\left(\mathbf{C}_{m\_\mathrm{iso}}^e\right)$ is the first invariant of the elastic part of the isochoric Cauchy-Green deformation tensor $\mathbf{C}_{m\_\mathrm{iso}}$ of the matrix and $\mathcal{L}^{-1}(x)$ is the inverse Langevin function given by a Padé approximant $\mathcal{L}^{-1}(x) \approx x\left(3-x^2\right)/\left(1-x^2\right)$.

II.2.2.2 Nanoparticles

The description of the nanoparticles requires to take into consideration the local interaction between hydrogel matrix and inorganic reinforcement through the micromechanics framework. The Eshelbian homogenization provides an approximate solution for the problem of one particle embedded in an infinite domain. The Eshelby equivalent inclusion method consists to replace the particle domain by the matrix material by the introduction of an eigenstrain replacing the perturbed strain induced by the inhomogeneity. Following this method, Yin et al. (2002) obtained the averaged eigenstrain of a particle interacting with its neighboring nanoparticles by means of the Green function technique. Appendix II.A provides a summarize of the procedure.

The finite-strain kinematics of the particles are derived from Eq. (II. A12) of the equivalent homogeneous medium of the linear elastic two-phase media given in Appendix II.A. In virtue of the Saint Venant-Kirchhoff assumption on hyperelastic media, the velocity gradient tensor of the particles $\mathbf{L}_p = \dot{\mathbf{F}}_p.\mathbf{F}_p^{-1}$ is expressed as:

$$\mathbf{L}_p = \mathbf{A}.\boldsymbol{\Gamma}.\left(\mathbf{I} - \phi\boldsymbol{\Gamma}\right)^{-1} : \bar{\mathbf{L}} \tag{II.21}$$

where $\bar{\mathbf{L}} = \dot{\bar{\mathbf{F}}}.\bar{\mathbf{F}}^{-1}$ is the macroscopic velocity gradient tensor of the nanocomposite, $\boldsymbol{\Gamma}$ is a tensor provided in Appendix I.A and $\mathbf{A}$ is the mismatch tensor:

$$\mathbf{A} = \left(\mathbf{K}_p - \mathbf{K}_m\right)^{-1}.\mathbf{K}_m \tag{II.22}$$

The free energy of the nanoparticles ψ_p is expressed through an ensemble-volume averaged homogenization procedure (Yin et al., 2002). It may be additively split into a volumetric part and an isochoric part as:

$$\psi_p = \left(\frac{\lambda_p}{2}\left(\chi_1 + 3\chi_2\right)^2 + \mu_p\left(2\chi_1\chi_2 + 3\chi_2^2\right)^2\right)\bar{\varepsilon}_{\text{vol}}^2 + \mu_p\chi_1^2\bar{\boldsymbol{\varepsilon}}_{\text{iso}} : \bar{\boldsymbol{\varepsilon}}_{\text{iso}} \tag{II.23}$$

where $\bar{\varepsilon}_{\text{vol}}$ is the Hencky volumetric strain, $\bar{\boldsymbol{\varepsilon}}_{\text{iso}} = \ln \bar{\mathbf{F}}_{\text{iso}}$ is the isochoric Hencky strain tensor, λ_p is the Lame's constant and, χ_1 and χ_1 are given by:

$$\chi_1 = \frac{1}{2w - M - \phi} \frac{\mu_m}{\mu_p - \mu_m} \text{ and } \chi_2 = \frac{1}{3\left(2w + 3m - M - \phi\right)} \frac{K_m}{K_p - K_m} - \frac{1}{3}\chi_1 \tag{II.24}$$

It is worth noticing that the local stress-strain response of the nanoparticles depends explicitly on the hydrogel matrix properties. Any perturbation of the local structure and dynamics of the hydrogel chains will affect the response of the nanoparticles as a result in changes of the near-field direct interactions.

II.2.3 Dynamic bonds

II.2.3.1 Stretching-retraction

Due to the large nanoparticle interfacial area, the nanoparticle surface contains a huge number of attaching groups which bond hydrogel chains having a chain length distribution (Haraguchi et al., 2002) with a mean length N . The basic inelastic features in the material system during the course of a stretching followed by a retraction are illustrated in Figure II.1 The detachment mechanism is a progressive process, beginning with the shorter chains and progressing into the longer ones. At the initial stage, all links are intact. During the stretching stage, a number of chains may be detached from the nanoparticle surface leading to changes in chain length. The chains detachment mechanism acts first in the shorter chains (see the yellow, blue and red chains in the illustration) attached between nanoparticles pair whereas the longer chains (see the green chains in the illustration) continue to sustain the chains network integrity. A hysteresis loop is then formed due to the concomitant contribution upon retraction of the chain re-attachment mechanism and the viscous effects. The re-attachment mechanism may be done in new positions (see the yellow chains in the illustration). The mean length of the elastically active chains $N\left(t\right)$

should be always larger than its reference $N_0 = N(t=0)$ whereas the mean chain density of the elastically active chains $n(t)$ should be always smaller than its reference $n_0 = n(t=0)$. We express these two physical quantities as follows:

$$N(t) = \frac{N_0}{N_{on/off}} \text{ and } n(t) = n_0 N_{on/off} \tag{II.25}$$

where the term $N_{on/off}$ is defined by the following kinetics:

$$\dot{N}_{on/off} = 1 - N_{on/off}\left(1 + k_{on/off}\right) \tag{II.26}$$

in which $k_{on/off}$ is the rate of attachable and detachable bonds given by:

$$k_{on/off} = k_{on/off\_0} \exp\left(\frac{\|\boldsymbol{\sigma}_m\|}{\sigma_{off} N_{on/off}}\right) \tag{II.27}$$

where k_{on/off_0} is a material constant and σ_{off} is a scale factor controlling the bonds strength.

A key point of our theory, the quantity $N_{on/off}$ is a decreasing function of the applied strain upon stretching and an increasing function of the applied strain upon retraction. The stress in the hydrogel matrix drives these opposite evolutions of $N_{on/off}$ by the rate of attachable and detachable bonds $k_{on/off}$. The evolutions affect in turn the interfacial characteristics and thus the bond strength between the two phases. At the end of the stretching-retraction process applied to the nanocomposite, the network recovers its initial features such that:

$$N(t) = N_0 \text{ and } n(t) = n_0 \tag{II. 28}$$

Nonetheless, the equilibrium state is not reached at the end of the mechanical loading since a strain amount remains retained in the hydrogel system at the loading time-scale.

To disclose some important indications concerning the chains behavior in interaction with the particles features, Figure II.3 presents an illustrative example of the chain force evolution with the applied strain for different particle radii while the particle amount is kept constant. The model parameters are those used for Figure II.4b. The model shows that the chain stiffness decreases distinctly with the decrease in particle radius and particle amount. Whereas in the case of a purely elastic response the chain force will become infinite at the limiting extension, the detachment mechanism leads to the progressive stiffness reduction and the appearance of a peak in the chain force evolution. When the particle amount increases, the chain damage occurs earlier and the critical strain involved in the peak force is distinctly decreased.

II.2.3.2 Self-healing

When the nanocomposite is unloaded down to a free stress, i.e. $\bar{\boldsymbol{\sigma}} = \mathbf{0}$, an amount of the strain is instantaneously recovered whereas another amount necessitates a longer recovery time (see the illustration in Figure II.1). The different parts of the deformation gradient tensors $\bar{\mathbf{F}} \neq \mathbf{I}$, $\mathbf{F}^{v}_{m\_\mathrm{iso}} \neq \mathbf{I}$, $\mathbf{F}^{e}_{m\_\mathrm{iso}} \neq \mathbf{I}$ and $\mathbf{F}_{p} \neq \mathbf{I}$ are related by using Eq. (II.8):

$$\mathbf{F}^{v}_{m\_\mathrm{iso}}\mathbf{F}^{e}_{m\_\mathrm{iso}} = \frac{1}{1-2\rho}\left(\bar{\mathbf{F}} - 2\rho\mathbf{F}_{p}\right) \tag{II.29}$$

Considering volume preserving, Eq. (II.3) is re-written as:

$$(1-2\rho)\boldsymbol{\sigma}_{m\_\mathrm{iso}} + \phi\boldsymbol{\sigma}_{p\_\mathrm{iso}} = \mathbf{0} \tag{II.30}$$

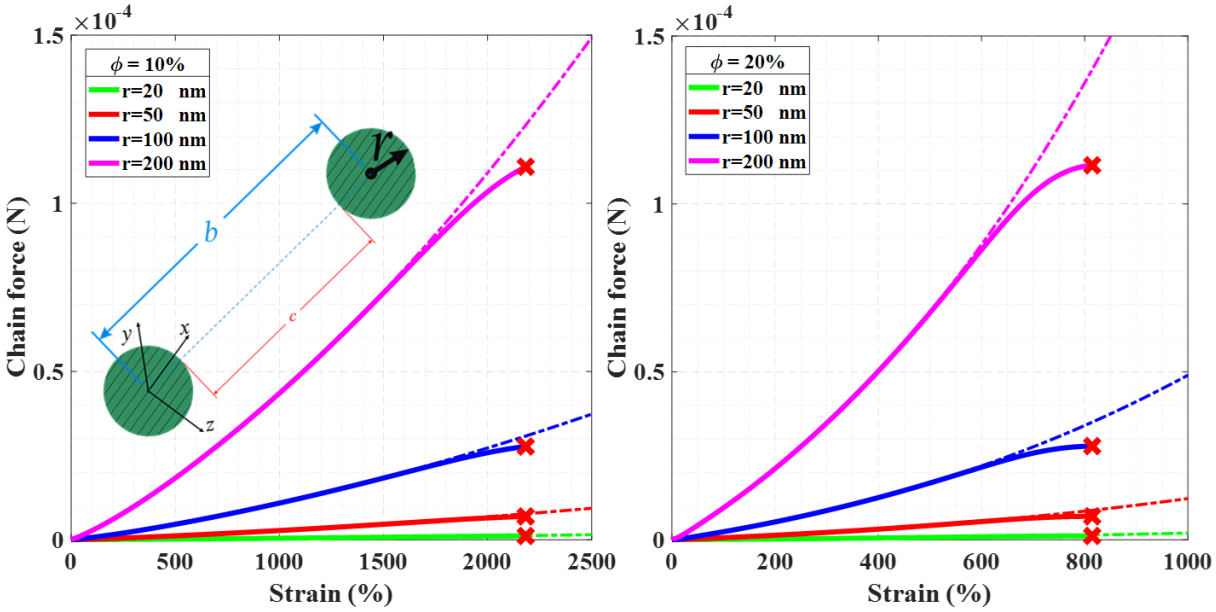

(a) (b)

Figure II.3 Model results for the chain force evolution at different particle radii considering a purely elastic response (dashed lines) and detachment mechanism (solid lines): (a) 10% filler amount, (b) 20% filler amount.

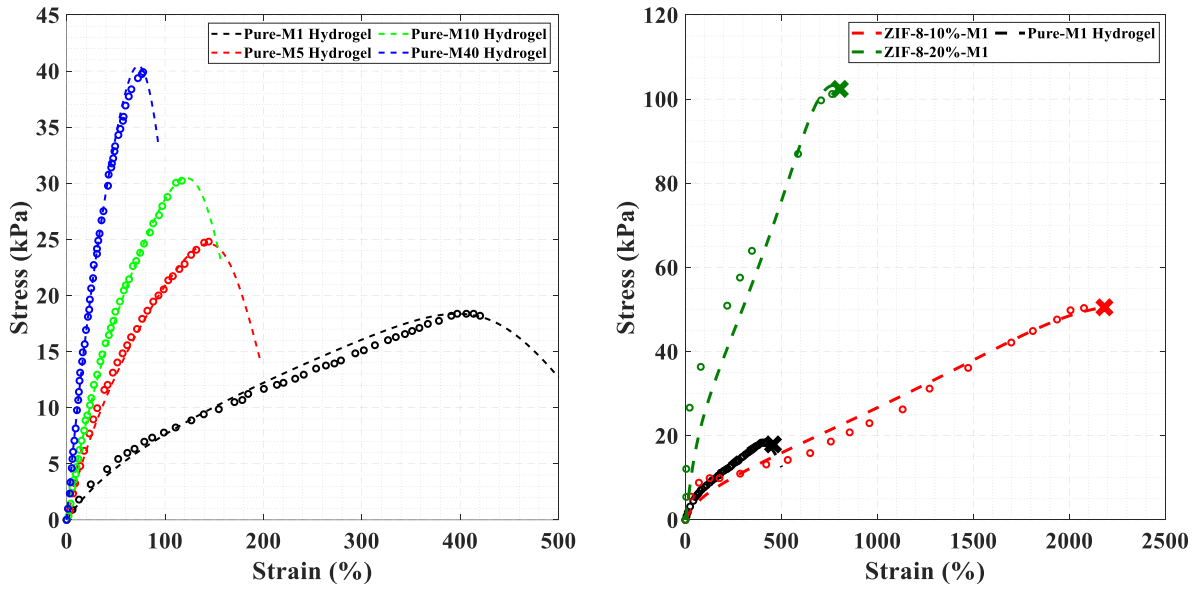

(a) (b)

Figure II.4 Stress-strain curves of the pure hydrogel and the hydrogel-based nanocomposites: (a) pure hydrogel for different cross-linker amounts, (b) hydrogel-ZIF-8 systems for different filler amounts (lines: model calibration results, symbols: experiments).

where the Cauchy stress tensors $\boldsymbol{\sigma}_{m\_\mathrm{iso}}$ and $\boldsymbol{\sigma}_{p\_\mathrm{iso}}$ may be expressed as:

$$\left[\boldsymbol{\sigma}_{m\_\mathrm{iso}}\right]_i = \frac{\lambda^e_{m\_i}}{J_m}\frac{\partial \psi_{m\_\mathrm{iso}}}{\partial \lambda^e_{m\_i}} = \frac{\lambda^e_{m\_i}}{J_m}\frac{\partial \psi_{m\_\mathrm{iso}}}{\partial I^e_{1m}}\frac{\partial I^e_{1m}}{\partial \lambda^e_{m\_i}} \text{ and } \left[\boldsymbol{\sigma}_{p\_\mathrm{iso}}\right]_i = \frac{\lambda_{p\_i}}{J_p}\frac{\partial \psi_{p\_\mathrm{iso}}}{\partial \lambda_{p\_i}} \tag{II.31}$$

No summation on *i* is implied in this equation.

From Eqs. (I.14), (I.15), (I.17) and (I.30), the viscous deformation gradient tensor $\mathbf{F}^v_{m\_\mathrm{iso}}$ can be extracted:

$$\dot{\mathbf{F}}^v_{m\_\mathrm{iso}} = -\frac{k_v}{\left(\sqrt{I^v_{1m}/3}-1\right)^{\alpha}}\frac{\phi}{1-2\rho}\mathbf{F}^v_{m\_\mathrm{iso}}.\boldsymbol{\sigma}_{p\_\mathrm{iso}} \tag{II.32}$$

Using Eq. (II.29) and (I.30), $\mathbf{F}^e_{m\_\mathrm{iso}}$ and $\bar{\mathbf{F}}$ are calculated upon a creep condition at zero-stress. The parameter k_v controls the hydrogel chains relaxation during the different loading stages. To consider the stretching-retraction asymmetry of the gel rate-sensitivity, the following expression is retained (Lin et al., 2020):

$$k_v = k_{v\_0}\left(1+\left|\frac{\dot{\lambda}}{\dot{\lambda}_0}\right|\right)^{\tau}\exp\left(\mathrm{sgn}\left(\dot{\lambda}\right)\right) \tag{II.33}$$

in which k_{v_0} is the viscous multiplier, τ is the rate-dependency factor and $\dot{\lambda}_0$ is the reference loading rate. The term $\mathrm{sgn}\left(\dot{\lambda}\right)$ signifies:

$$\mathrm{sgn}\left(\dot{\lambda}\right) = \begin{cases} +1 & \text{for stretching} \quad \left(\dot{\lambda}>0\right) \\ -1 & \text{for retraction} \quad \left(\dot{\lambda}<0\right) \\ 0 & \text{for recovery} \quad \left(\dot{\lambda}=0\right) \end{cases} \tag{II.34}$$

By constitutively relating the nanostructure and the overall nanocomposite behavior, the model may be employed to better understand the mechanisms of mechanical property enhancement. To

this goal, the following important features will be examined by comparisons with available experimental data of a variety of nanocomposite systems:

- The stretching-retraction cycle of nanocomposite system in connection to the chains detachment-attachment mechanism and the nanoparticle-matrix interaction as illustrated in Figure II. 1.
- The complete failure of nanocomposite system when the network losses all connectivity.
- The self-healing response of nanocomposite system when the network recovers its equilibrium state.

II.3 Comparison with experiments

The model contains very few inputs listed in Table II.1 for which the physical meaning is provided. Some of them (elastic constants of phases, chains network features and amount of phases) have direct physical meaning while others (related to viscosity and bonds dissociation/re-association) are physically interpretable.

In what follows, the effects of various microstructures on the macro-response are considered by examining nanofiller type, nanofiller concentration and hydrogel chains network features. The examined macro-behaviors include monotonic stress-strain response till failure and some inelastic features such as rate-dependency, hysteresis, continuous relaxation and room temperature self-healing facility. Some data are used to fit the model parameters while others are used to verify the model predictability. All stress and strain quantities are defined in their nominal form.

II.3.1 Stretchability and strength

In this section, the model calibrations are compared to monotonic stress-strain experimental data taken from the work of Liu et al. (2019). The hydrogel systems are made of metal-organic

framework (MOF) (ZIF-8, ZIF-67, UiO-66) and SiO_2. The hydrogel systems are designated as X-Y-Z (X being the filler type, Y the filler amount and Z the cross-linker amount). The tests have been performed at room temperature under a constant stretch rate of 30 min^{-1}. Figures. II.4 and II.5 present the comparison between micromechanical model simulations and experimental data in which several microstructure factors having a significant impact are examined. Model simulations are presented as lines while experimental data are presented as symbols. The computed stress is presented till failure that is defined as the local maximum stress. Unless explicitly otherwise stated, the model inputs are those listed in Table II.1. They correspond to a cross-linker amount of 1 mg and a filler amount of 10%. They were obtained through a fitting optimization based on the minimization of differences between model simulations and experimental data. Figures. II.6 and II.7 completes the identification results with the parameters affected by the cross-linker and filler amounts. The values must be seen as average values incorporating variability effects and the trends will be used to bring a better understanding of reinforcement mechanisms.

				Hydrogel-based nanocomposites (ϕ = 10%)				
Parameter	Significance	Matrix-1	Matrix-2	ZIF-8	ZIF-67	UiO-66	SiO_2	Fe^{3+}
N	Mean chain length	30	10	47	35	22	30	3
n (m^{-3})	Mean chain density	1.05×10^{27}	$1.34x10^{26}$	1.46×10^{27}	1.46×10^{27}	2.36×10^{27}	8.26×10^{27}	2.19×10^{27}
ν_m	Matrix Poisson's ratio	0.49	0.49	0.49	0.49	0.49	0.49	0.49
$\mu_p/\mu_m = K_p/K_m$	Moduli mismatch	0	0	60	60	60	30	50
$\dot{\kappa}_{on/off\_0}$ (s^{-1})	Dynamic bonds	5×10^{-5}	5×10^{-5}	5×10^{-5}	5×10^{-5}	5×10^{-5}	5×10^{-5}	5×10^{-5}
σ_{off} (MPa)	Bonds strength	12	0.69	150	165	150	380	Eq. (II.35)
$\dot{\kappa}_{v\_0}$ ($MPa^{-1}\ s^{-1}$)	Viscous multiplier	6×10^{-5}	1.24×10^{-4}	1.087×10^{-4}	1.087×10^{-4}	1.087×10^{-4}	8.7×10^{-5}	Eq. (II.36)
$\dot{\lambda}_0$	Reference loading rate	0.01	0.01	0.01	0.01	0.01	0.01	0.01
τ	Rate-dependency	0.8	0.8	0.8	0.8	0.8	0.8	0.8
α	Stretch-dependency	1.2	1.8	2.1	2.1	2.1	0.9	0.69

Table II.1 Model parameters for various hydrogel-based systems with cross-linker amount of 1 mg.

II.3.1.1 Pure hydrogel

Prior to compare with the data of nanocomposites, Figure II.4a. presents the comparison between model simulations and stress-strain experimental data of the pure hydrogel (designated as matrix-1 in Table II.1) including different cross-linker amounts (1, 5, 10 and 40 mg).

The obvious increase in stiffness and decrease in stretchability with the increase in cross-linker amount is the direct consequence of chemical microstructure change, that is, an increase in mean density and strength of elastically active chains (along with a decrease in mean length of elastically active chains) as shown in Figure II.6a.

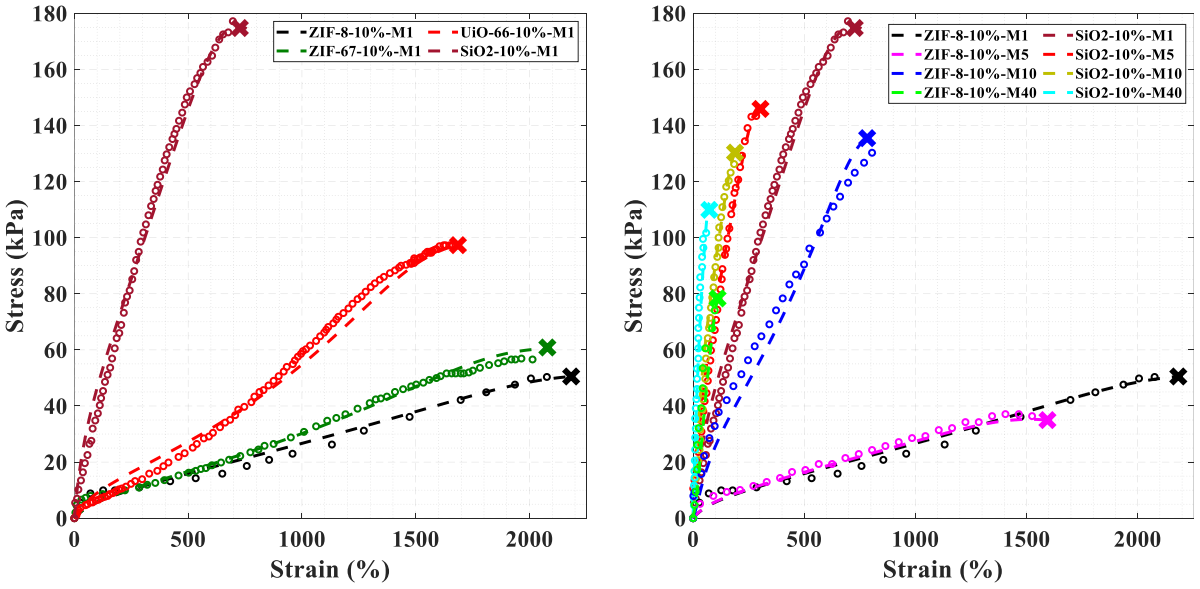

(a) (b)

Figure II.5 Stress-strain curves of the hydrogel-based nanocomposites for different filler types: (a) ZIF-8, ZIF-67, UiO-66 and SiO2 (b) ZIF-8 and SiO_2 for different cross-linker amounts (lines: model calibration results, symbols: experiments).

Bonds strength in pure hydrogel is slightly modified with the variation in cross-linker amount but chains viscosity remains constant as evidenced in Figure II.7a.

II.3.1.2 Filler amount

Figure II.4b presents the stress-strain curves of the hydrogel-ZIF-8 systems for different filler amounts using hydrogel as the matrix. The presence of nanoparticles is likely to modify the molecular organization and dynamics of the hydrogel chains as compared to the pure hydrogel.

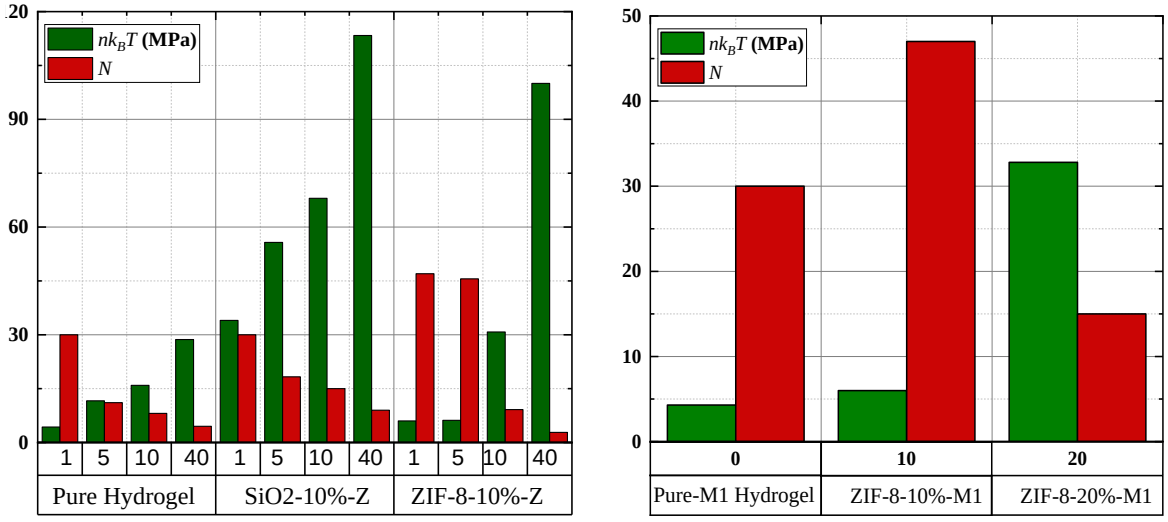

(a) (b)

Figure II.6 Mean chain density *n* and mean chain length *N*: (a) Effect of the cross-linker amount (in mg with Z = 1, 5, 10 and 40), (b) effect of the filler amount (in %).

The dispersion of 10% nanoparticles in the hydrogel leads to a remarkable increase of ductility. When the amount of nanoparticles increases from 10% to 20%, the contact area between nanoparticles and hydrogel matrix is extremely magnified. As a consequence, the stretchability decreases but the mechanical strength significantly increases, indicating that adding more ZIF-8 nanofillers leads to a loss of mobility of hydrogel chains in the vicinity of nanofillers that strengthens the whole hydrogel network (Figure II.6b and II.7b). Due to the increased level of interactions between the hydrogel chains and the nanoparticles, the chains viscosity is also increased.

II.3.1.3 Filler type

The application of our model is extended to the other types of reinforcing elements (namely ZIF-67, UiO-66 and SiO_2) in Figure II.5. While the model is capable of fitting the experimental data

reasonably well, it can bring some physical interpretations in particular on the complex interaction between nanofillers and hydrogel matrix.

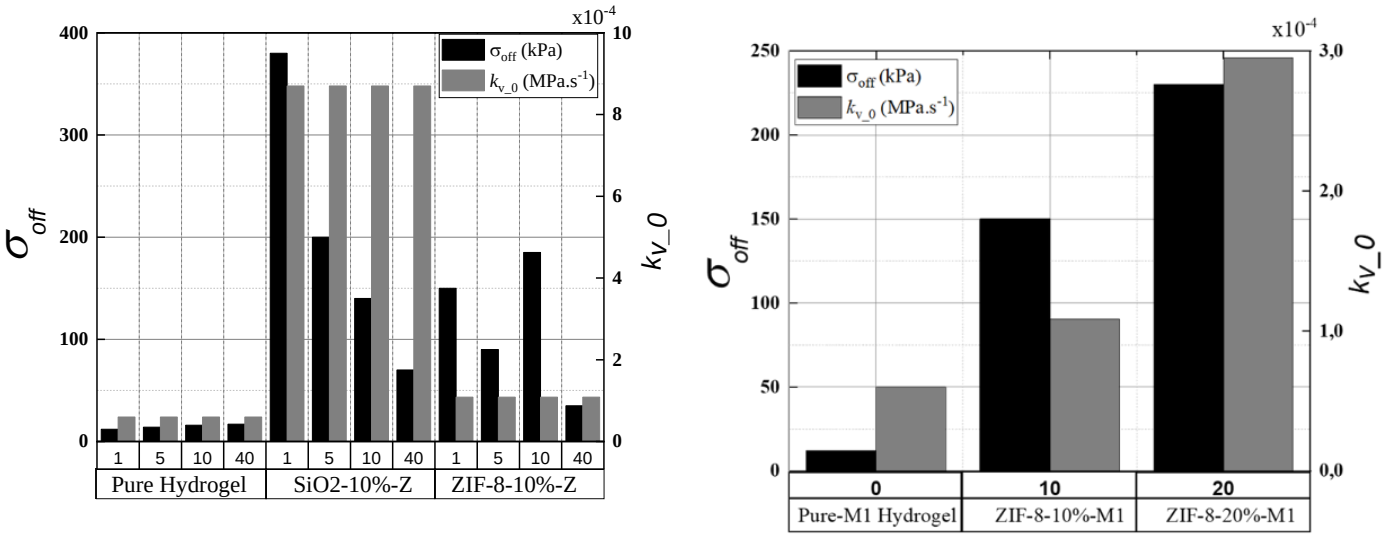

(a) (b)

Figure II.7 Bonds strength σ_{off} and chains viscosity k_{v_0}: (a) Effect of the cross-linker amount (in mg with Z = 1, 5, 10 and 40), (b) effect of the filler amount (in %).

The level of overall property enhancement is controlled by the strong nanoparticle-matrix interactions and the mobility changes at the nano-scale. Inevitably, the higher level of interaction, the larger the perturbed region of polymer matrix surrounding the nanoparticle (Boutaleb et al., 2009). Table II.1 shows a modification of the properties of the hydrogel inside the nanocomposite, as compared to those of the neat hydrogel. The nanoparticles act as additional crosslinking points to strengthen the network but the strength of interactions varies from a nanofiller type to another which impacts differently the stretchability and the mechanical strength of the nanocomposite. The evolution of the chains network due to progressive chains detachment mechanism is presented in Figure II.8a till its complete loss of load-bearing capability. Also, the interfacial interaction between hydrogel matrix and nanoparticles is affected by the hydrogel

response evolution that in turn affects the nanoparticles response. As shown in Figure II.8b, the stress magnitude in the nanoparticles depends on their nature and the gradual weakening of bonds between the two phases.

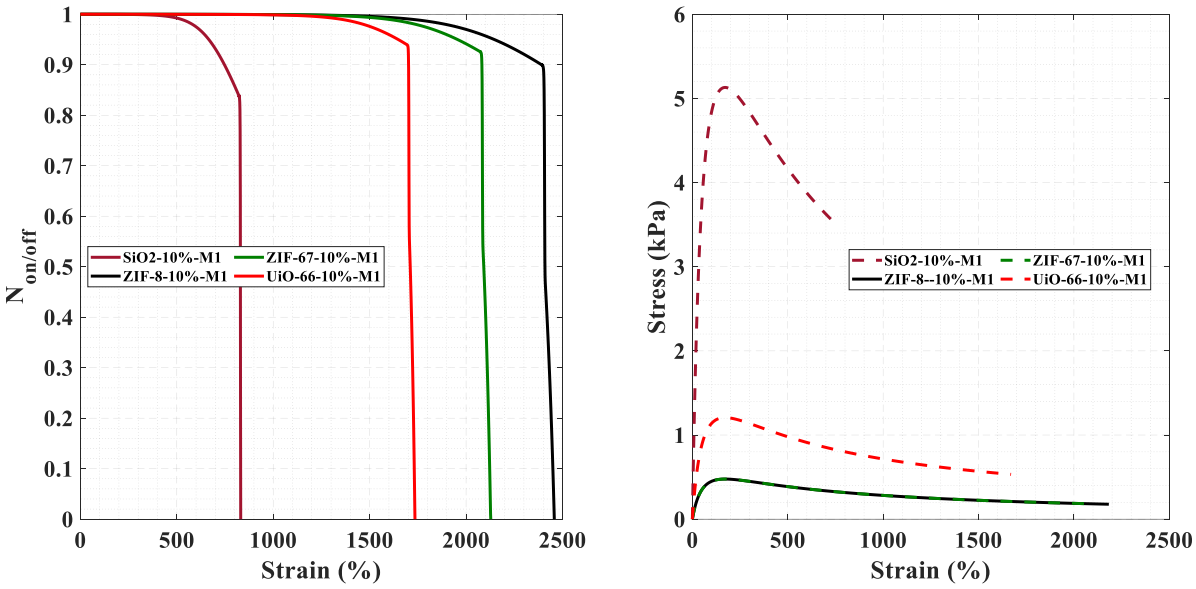

(a) (b)

Figure II.8 Evolution as a function of strain of (a) chains network translated by $N_{on/off}$ and (b) stress in nanoparticles for different filler types.

This local response can be connected to the macroscopic mechanical properties given in Figure II.5a in particular to the maximum strain and stress levels reached by the nanocomposite before final failure. The ZIF-8-10%-M1 and ZIF-67-10%-M1 hydrogels exhibit quite similar stretchability whereas the UiO-66-10%-M1 hydrogel is slightly less stretchable than the ZIF systems but with a significantly higher mechanical strength. The SiO_2-10%-M1 hydrogel has the lowest ductility but the highest toughening effects with a great mechanical strength improvement. The reinforcement mechanisms are generally ascribed to electrostatic interactions between the hydrogel chains and the nanofillers. Stronger near-field direct interactions result in better mechanical properties of the hydrogel-based nanocomposites. In MOF nanofillers (ZIF and UiO),

the polar groups and cationic metal centers on the nanoparticle surface act as anchoring points for hydrogel chains (Liu et al., 2019). The latter results in an increase in mean chain density (see Table II.1 and Figure II.6). The insolubility and aggregation of SiO_2 nanofillers leads to higher crosslinking points in hydrogel, compared to MOF nanofillers, and to a higher mean chain density. The ZIF-8 and SiO_2 nanofillers reinforcement is also examined in Figure II.5b. for different cross-linker amounts. The increase in cross-linker amount profoundly modifies the chains network properties as reported in Figures II.6a. and II.7a. Both mean length and density evolve with cross-linker amount but in an opposite manner. The toughening effects of the hydrogels are also largely determined by the strength of nanofillers-matrix interactions and the competition between elasticity and strength of the temporarily attached chains. Note that the effects of the cross-linker amount on the macro-stress are directly connected to the local properties evolution in the hydrogel and depends on the nanofiller type. The monotonic macro-stress evolution of the SiO_2 hydrogel with cross-linker amount implies a monotonic evolution of the network properties as observed in the plots of Figures. II.6a and II.7a. The network monotonic evolution is not expected for the ZIF-8 hydrogel since its macro-stress at failure increases with the cross-linker amount to reach a maximum value and falls beyond this value. Figure II.6a shows that the bonds strength in the ZIF-8 hydrogel follows the same trends. Also, the nanofiller-matrix interaction leads to an alteration of the network properties, amplified by the filler amount as observed in the plots of Figures II.6b and II.7b.

II.3.2 Inelastic features

In this section, the model is applied to some history-dependent features (such as rate-dependent stress-strain till failure, hysteresis and continuous relaxation) of hydrogel-based nanocomposites with metal-coordinated Fe^{3+} bonds taken from the work of Lin et al. (2020).

II.3.2.1 Rate-dependent stretchability and strength

Figure II.9 shows that our model is able to provide a good representation of the monotonic stress-strain response for the different stretching rates. Again, the micromechanical model results are presented till failure that is defined as the local maximum stress.

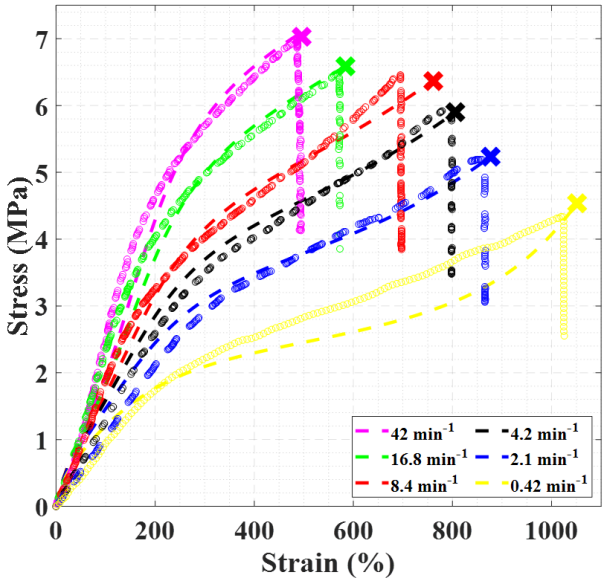

Figure II.9 Stress-strain curves of the hydrogel-based Fe^{3+} nanocomposites for different stretch rates (lines: model calibration results, symbols: experiments).

The inputs required by the modeling are listed in Table II.1 in which the bonds strength parameter σ_{off} and the viscous multiplier k_{v_0} are expressed as follows:

$$\sigma_{off} = -3.73\exp\left(-2.9\times10^{-1}\dot{\lambda}\right)+6.40 \tag{I.35}$$

$$k_{v\_0} = -2.34\exp\left(-4.2\times10^{-2}\dot{\lambda}\right)-2.48 \tag{I.36}$$

While these data provide a good first verification of the model, Figures II.10- II.14 present some model predictions for various key loading conditions governing the hydrogel mechanics. The

goal is to further verify the predictive capacities of the model and to better understand the relation between macro-response and mechanisms of nanofillers reinforcement.

II.3.2.2 Stress hysteresis

Figure II.10 shows how the model can reproduce the hydrogel mechanics during stretching-retraction cycles at different maximum stretch levels and stretch rates, respectively. In these simulations, the macroscopic stretch is ramped to a pre-determined level at a constant rate and then ramped down to zero-stress at the same absolute constant rate. The pronounced hysteresis loops displayed by the material upon the cyclic loading is well captured by the model along with the increase in loop area (along with the related dissipated energy) with increasing applied strain. During the hydrogel retraction stage, the unloading path shape is not well replicated by the model what a fine analysis of the model results has attributed to the particles response. The effect of the applied strain on the recovery extent at the end of the retraction segment is nonetheless well captured by the model. It is therefore able to connect the nanostructure, the dissociation and re-association mechanism of the shorter hydrogel chains and the macroscopic stress hysteresis of the nanocomposite system (see Figure II.1).

II.3.2.3 Stress relaxation

We examine also the model capabilities under continuous relaxation. In these simulations, the macroscopic stretch is ramped to a pre-determined level at a constant rate and then kept constant for a prescribed delay. As depicted in Figure II.11, the model is able to reproduce the different features of the Fe^{3+} hydrogel mechanics upon continuous relaxation at different maximum stretch levels and stretch rates, respectively. These adequate agreements further confirm the validity of our approach.

II.3.2.4 Self-healing

To illustrate further the model capabilities, the capacity of the hydrogels to restore, by self-healing, initial microstructure and mechanical strength, in relation to loading conditions and microstructure features, is now treated. Figure II.12 shows the capability of our model to evaluate the room temperature self-healing of the Fe^{3+} hydrogel for different recovery times. In the simulations, a creep at zero-stress is carried out for a prescribed waiting delay between each stretching-retraction cycle. The second cycle is reported in the Figure order to replicate the same conditions than the experiments of Lin et al. (2020), an amount of remanent strain (at zero-stress) still remaining after the partial strain recovery. The creep process, corresponding to the course of the recovery from non-equilibrium state (at the retraction instant) to equilibrium state when the hydrogel recovers its initial conformation, is driven in our theory by the formulae of Section II.2.3.2. In agreement with the experimental observations, the model simulations show that the mechanical strength and the hysteresis loop become progressively larger with the waiting time, indicating the gradual recovery of the hydrogel-based nanocomposite. It is satisfactory to point out that the waiting time of eight hours for the nearly full recovery is well captured by the model. The proper description of the stress-strain curves till failure as well the hysteresis, the continuous relaxation and the room temperature self-healing facility demonstrates that the microstructure monitoring via the model seems physically realistic.

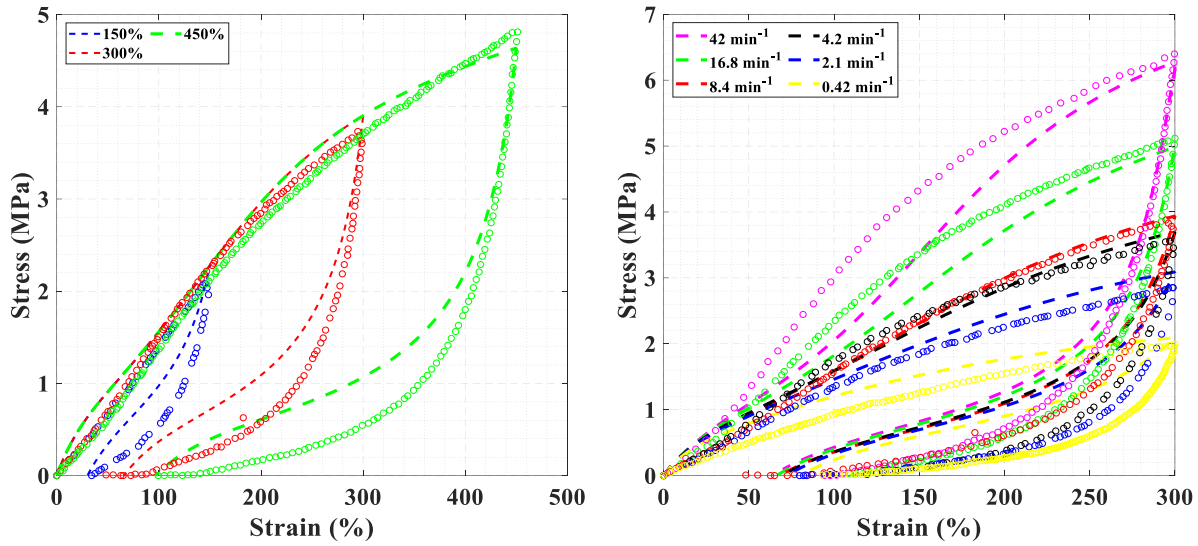

(a) (b)

Figure II.10 Stress-strain curves of the hydrogel-based Fe^{3+} nanocomposites upon a stretching-retraction cycle at (a) a stretch rate of 8.4 min^{-1} and at different stretch levels, (b) different stretch rates and a strain level of 300% (lines: model, symbols: experiments).

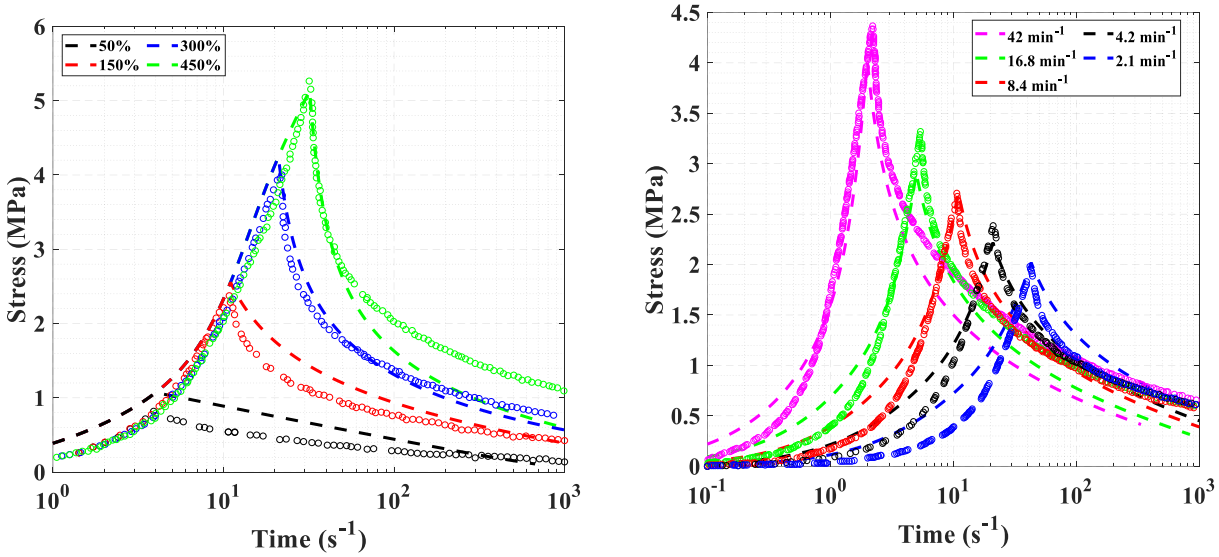

(a) (b)

Figure II.11 Temporal stress changes of the hydrogel-based Fe^{3+} nanocomposites upon a stretching followed by a relaxation at (a) different strain levels and a stretch rate of 8.4 min^{-1}, (b) a strain level of 150% and different stretch rates (lines: model, symbols: experiments).

It should be emphasized that one of the most important capabilities of the proposed model is related to self-healing predictions that may be related to loading histories and microstructure features.

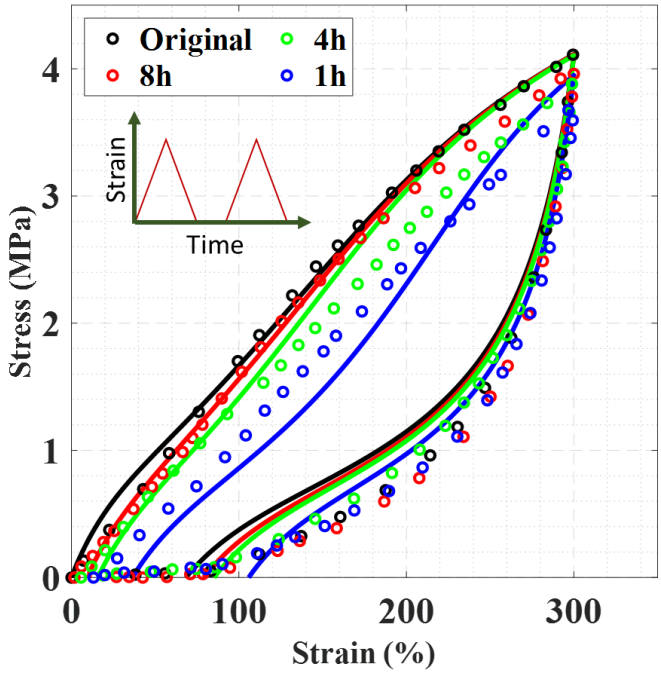

Figure II.12 Recovery time effect on the second stretching-retraction cycles of the hydrogel-based Fe^{3+} nanocomposites at a stretch rate of 8.4 min^{-1} and a strain level of 300% (lines: model, symbols: experiments).

The strain evolution during recovery at zero-stress of the hydrogel-based $Fe3^{+}$ nanocomposites is plotted in Figure II.13 as a function of recovery time such that a curved profile is obtained by considering the following expression for the strain recovery R :

$$R = \left(1 - \frac{\varepsilon}{\varepsilon_{max}}\right) \times 100 \tag{I.37}$$

where ε and ε_{max} are, respectively, the nominal strain stored in the hydrogel and its maximum value. The strain recovery starts to increase linearly with the recovery time and rapidly exhibits a curved profile which tends towards a stabilized state for which there is no strain recovery

change. The reached maximum recovery extent corresponds to the equilibrium state. Similar profiles are obtained in other traditional polymeric systems (Su and Peng, 2018; Shen et al., 2019; Cherief et al., 2020; Dai et al., 2020) but with a strain recovery requiring a quasi-infinite duration at room temperature.

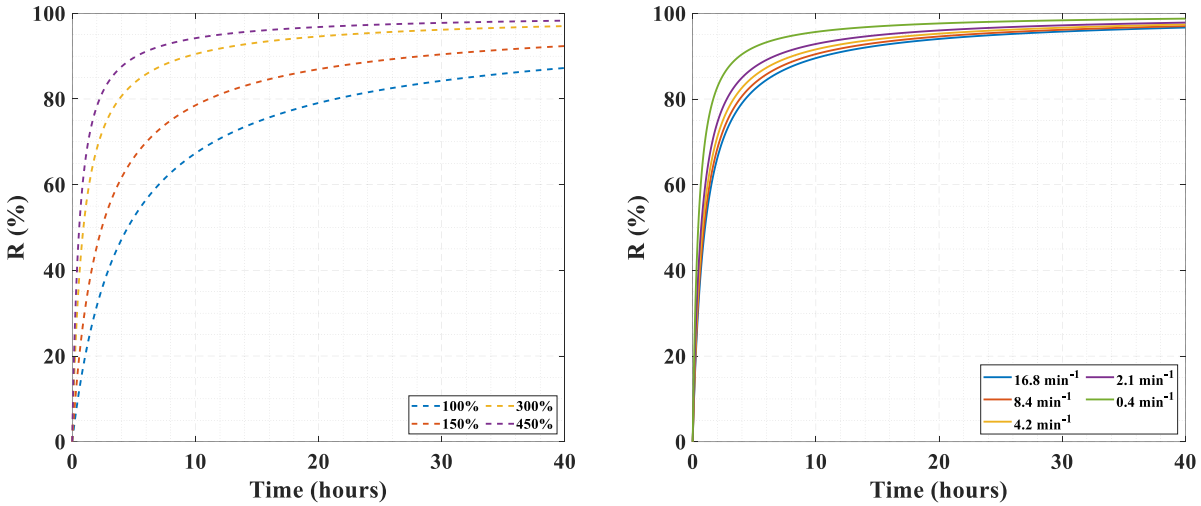

(a) (b)

Figure II.13 Recovery behavior of the hydrogel-based Fe^{3+} nanocomposites previously stretched at (a) different stretch levels at a stretch rate of 8.4 min^{-1}, (b) different stretch rates at a strain level of 300%.

Figure II.13 depicts the effect of loading conditions (stretch levels and stretch rates) on the self-healing response. It can be observed that the higher the strain level, the higher the recovery extent. Due to higher hydrogel chains relaxation at the lowest stretch rate, the time-dependent recovery becomes significantly higher with less elastic energy.

Numerical simulations are carried out to address the influence of microstructure features on the self-healing facility of hydrogel systems examined in Section II.3.1. Figure II.14 provides important indications concerning the complex nanofiller-matrix interaction on the self-healing facility due to variations in nanofiller type and cross-linker amount. Figure II.14a shows that the

recovery extent varies from a nanofiller type to another which indicates the great complexity of the history-dependent features of hydrogel systems. This prediction is possible because the reinforcing effect of nanoparticles is introduced in the model. The micromechanical model results in Figure II.14b show that the cross-linker amount is also another key microstructure parameter governing the response.

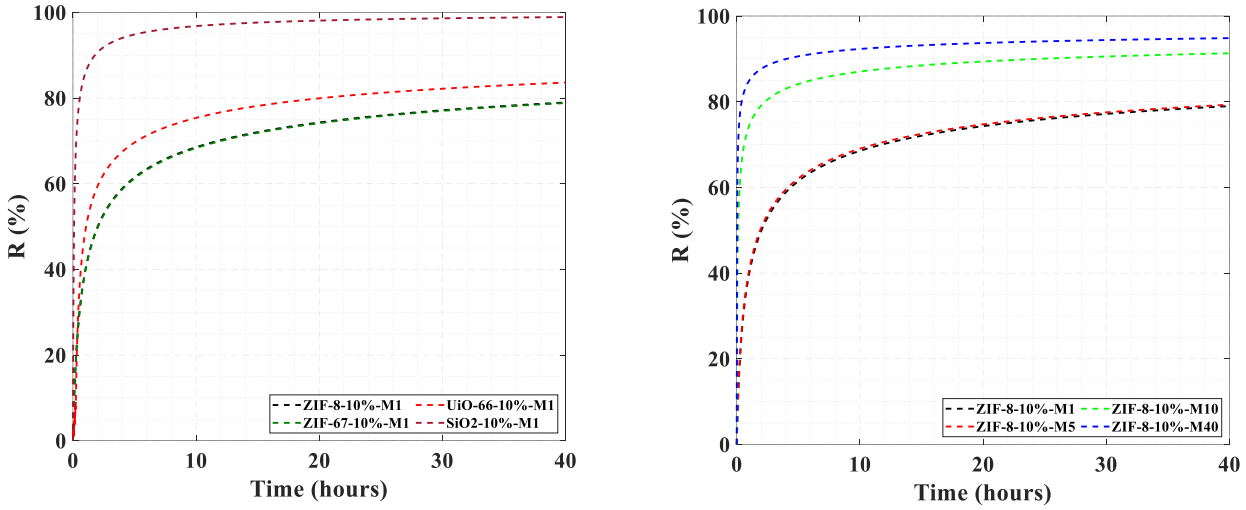

(a) (b)

Figure II.14 Recovery behavior of the hydrogel-based nanocomposites previously stretched at a stretch rate of 30 min^{-1} and a strain level of 300%: (a) different filler types, (b) different cross-linker amounts.

It can be observed that the increase in cross-linker amount enhances the self-healing ability. The micromechanical model simulations demonstrate that for the evaluation of the self-healing response, it is fundamental to consider the simultaneous effects of the different internal network features related to the nanoparticles and the hydrogel matrix. This prediction can only be made if they are explicit inputs of the modeling approach.

II.3.3 Biaxial loading effect

As a final point of discussion, the model capabilities to describe the biaxial behavior of hydrogel systems is presented. The model is expected to predict the visco-super-elastic response under any biaxial loading path. Nonetheless, multiaxial experiments on hydrogel systems are rarely documented in the literature. As far as we know, only the work of Mai et al. (2018) exists to date and only for a pure hydrogel stretched under equibiaxial (EB), unequal biaxial (UB) with a 0.5 biaxiality ratio and planar (P) loadings. Figure II.15 provides a schematic representation of these biaxial loading paths. All experiments have been performed at room temperature under a constant stretch rate of 1.2 min^{-1}. Figure II.15 provides the experimental data of Mai et al. (2018) and the computed stress as a function of the applied strain along the maximum principal direction. The model parameters were identified from the EB response of the pure hydrogel (designated as matrix-2 in Table II.1) and the same model parameters were then used to predict the UB and P curves. It is satisfactory to observe that the model provides an acceptable description of the nonlinear stress response and the peak (failure) stress. The predicted stretches at failure are plotted in Figure II.16 under a wider range of biaxiality ratios such that a failure envelope is obtained with a symmetry relative to the main bisectrix.

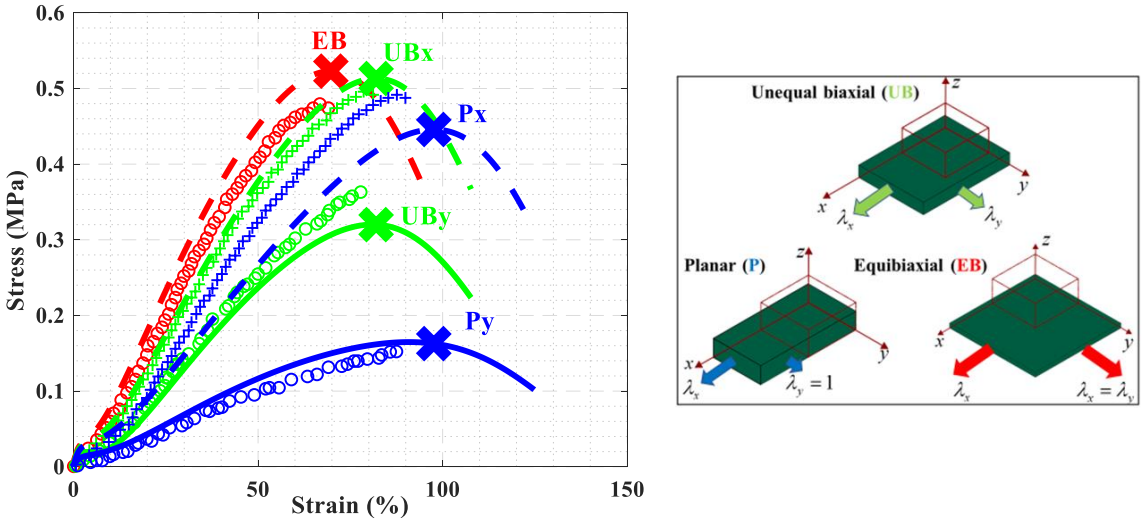

Figure II.15 Stress-strain curves of the pure hydrogel under different biaxial loading conditions (lines: model, symbols: experiments).

The model is also used in Figure II.16 to predict the effect of nanofillers reinforcement on the biaxial failure envelope. The insertion of inorganic nanoparticles into the matrix-2 is performed using the same amplifying effect obtained for the matrix-1 properties for the nanofiller types examined in Section II.3.1. The larger failure envelope is obtained for the ZIF-8 hydrogel and the smaller one for the the SiO_2 hydrogel.

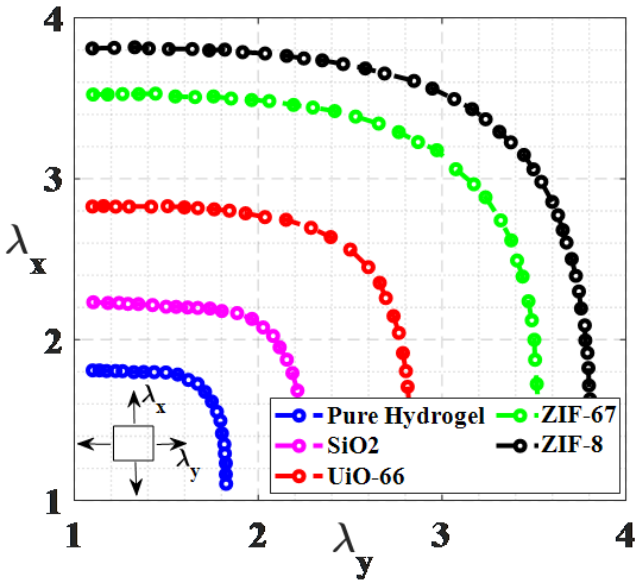

Figure II.16 Model results for the biaxial failure envelope of the pure hydrogel and the hydrogel-based nanocomposites (with cross-linker amount of 1 mg and filler amount of 10%).

II.4 Partial conclusion

The aim of this chapter was to propose a quantitative prediction of the mechanics of visco-super-elastic hydrogel-based nanocomposites. Using the concept of cubic material volume combined with the Eshelby equivalent inclusion method, the continuum-based model connects the macro-response to internal network physics starting from the nanostructure. The model is used to relate the reinforcing effect of nanoparticles to overall properties such as stretchability, mechanical

strength, stress hysteresis and self-healing response. Quantitative comparisons with available experiments show the relevance of the model for a variety of hydrogel-nanofiller material systems. The model contains very few physically interpretable material constants and appears as a valuable tool for the reliable design of such new material systems.

Appendix II.A. Volumetric free energy function

From the Eshelby equivalent inclusion method under infinitesimal elastic theory, the local strain fields $\boldsymbol{\varepsilon}$ may be expressed at any local point $\boldsymbol{r}$ of the domain occupied by the nanoparticles Ω_p and by the hydrogel matrix Ω_m (Ju and Sun, 1999):

$$\boldsymbol{\varepsilon}(\boldsymbol{r}) = \mathbf{K}_m^{-1} : \boldsymbol{\sigma}(\boldsymbol{r}) + \boldsymbol{\varepsilon}^*(\boldsymbol{r}) \text{ for } \boldsymbol{r} \in \Omega_p \text{ and } \boldsymbol{\varepsilon}(\boldsymbol{r}) = \mathbf{K}_m^{-1} : \boldsymbol{\sigma}(\boldsymbol{r}) \text{ for } \boldsymbol{r} \in \Omega_m \tag{II.A1}$$

where $\boldsymbol{\sigma}(\boldsymbol{r})$ is the local stress and $\boldsymbol{\varepsilon}^*$ is the equivalent eigenstrain.

The interaction of the central nanoparticle with its eight neighboring nanoparticles is considered by means of the Green function technique. At any local point $\boldsymbol{r}$ of the central nanoparticle P_0, the perturbed strain $\boldsymbol{\varepsilon}'(\boldsymbol{r})$ can be related to the eigenstrain $\boldsymbol{\varepsilon}^*(\boldsymbol{r})$ as the sum of the perturbation contribution from the central nanoparticle itself and the effect from the local points $\boldsymbol{r}'$ in the eight neighboring nanoparticles:

$$\boldsymbol{\varepsilon}'(\boldsymbol{r}) = \mathbf{S} : \boldsymbol{\varepsilon}^*(\boldsymbol{r}) + \sum_{i=1}^{n=8} \int_{\Omega_i} \mathbf{G}(\boldsymbol{r} - \boldsymbol{r}') : \boldsymbol{\varepsilon}^*(\boldsymbol{r}') \mathrm{d}\boldsymbol{r}' \tag{II.A2}$$

where $\mathbf{S}$ is the Eshelby tensor and $\mathbf{G}$ is the fourth-rank Green function:

$$G_{ijkl}(\boldsymbol{r} - \boldsymbol{r}') = \frac{1}{8\pi(1-\nu_m)\bar{r}^3} \begin{bmatrix} (1-2\nu_m)(\delta_{ik}\delta_{jl} + \delta_{il}\delta_{jk} - \delta_{ij}\delta_{kl}) \\ +3\nu_m(\delta_{ik}n_j n_l + \delta_{il}n_j n_k + \delta_{jk}n_i n_l + \delta_{jl}n_i n_k) \\ +3\delta_{ij}n_k n_l + 3(1-2\nu_m)\delta_{kl}n_i n_j - 15 n_i n_j n_k n_l \end{bmatrix} \tag{II.A3}$$

in which δ_{ij} is the Kronecker delta, $\bar{r} = \|\boldsymbol{r} - \boldsymbol{r}'\|$, $\boldsymbol{n} = (\boldsymbol{r} - \boldsymbol{r}')/\bar{r}$ and ν_m is the Poisson's ratio of the hydrogel matrix.

The volume averaged eigenstrain $\overline{\boldsymbol{\varepsilon}}^{*}_{\Omega_0}$ over the domain occupied by the central nanoparticle is:

$$-\mathbf{A}:\overline{\boldsymbol{\varepsilon}}^{*}_{\Omega_0}=\boldsymbol{\varepsilon}_0+\mathbf{S}:\overline{\boldsymbol{\varepsilon}}^{*}_{\Omega_0}+\mathbf{g}:\overline{\boldsymbol{\varepsilon}}^{*}_{\Omega_0} \tag{II.A4}$$

where $\boldsymbol{\varepsilon}_0$ is the far-field strain ($\boldsymbol{\varepsilon}_0=\mathbf{K}_m^{-1}:\boldsymbol{\sigma}_0$ with $\boldsymbol{\sigma}_0$ the far-field stress) and $\boldsymbol{g}$ is the interaction term:

$$\boldsymbol{g}=\frac{1}{\Omega_m}\sum_{i=1}^{n=8}\int_{\Omega_m}\int_{\Omega_i}\mathbf{G}\left(\boldsymbol{r}-\boldsymbol{r}'\right)\mathrm{d}\boldsymbol{r}\,\mathrm{d}\boldsymbol{r}' \tag{II.A5}$$

Yin et al. (2002) derived the following relationship of the volume averaged eigenstrain $\overline{\boldsymbol{\varepsilon}}^{*}_{\Omega_0}$:

$$\overline{\boldsymbol{\varepsilon}}^{*}_{\Omega_0}=-\boldsymbol{\Gamma}:\boldsymbol{\varepsilon}_0 \tag{II.A6}$$

where $\boldsymbol{\Gamma}$ is a tensor given by:

$$\Gamma_{ijkl}=\left(\frac{-m}{\left(2w-M\right)\left(2w+3m-M\right)}+\frac{M}{2w\left(2w-M\right)}\delta_{IK}\right)\delta_{ij}\delta_{kl}+\frac{1}{4w}\left(\delta_{ik}\delta_{jl}+\delta_{il}\delta_{jk}\right) \tag{II.A7}$$

in which m, w and M are given by:

$$m=\frac{1}{3}\left(\frac{K_m}{K_p-K_m}-\frac{\mu_m}{\mu_p-\mu_m}\right)+\frac{5\nu_m-1}{15\left(1-\nu_m\right)}+\frac{M}{5} \tag{II.A8}$$

$$w=\frac{1}{2}\frac{\mu_m}{\mu_p-\mu_m}+\frac{4-5\nu_m}{15\left(1-\nu_m\right)}+\frac{M}{5} \tag{II.A9}$$

$$M=\frac{40\left(14\rho^2-5\right)\rho^3}{45\left(1-\nu_m\right)} \tag{II.A10}$$

The governing constitutive equations of the equivalent homogeneous medium of the linear elastic two-phase medium are given by the following relationships (Yin et al., 2002):

$$\bar{\boldsymbol{\sigma}} = \bar{\mathbf{K}} : \bar{\boldsymbol{\varepsilon}}^{e} = \mathbf{K}_{m} : \boldsymbol{\varepsilon}_{0} \tag{II.A11}$$

$$\bar{\boldsymbol{\varepsilon}}^{e} = \left(\mathbf{I} - \phi\boldsymbol{\Gamma}\right).\boldsymbol{\Gamma}^{-1}.\mathbf{A}^{-1} : \boldsymbol{\varepsilon}_{p} \tag{II.A12}$$

$$\boldsymbol{\varepsilon}_{0} = \left(\mathbf{I} - \phi\boldsymbol{\Gamma}\right)^{-1} : \bar{\boldsymbol{\varepsilon}}^{e} \tag{II.A13}$$

where $\bar{\boldsymbol{\sigma}}$ and $\bar{\boldsymbol{\varepsilon}}^{e}$ are the ensemble-volume averaged (macroscopic) stress and elastic strain tensors and $\bar{\mathbf{K}}$ is the macroscopic stiffness tensor.

References

Arruda, E.M., Boyce, M.C., 1993. A three-dimensional constitutive model for the large stretch behavior of rubber elastic materials. Journal of the Mechanics and Physics of Solids 41, 389-412.

Bergstrom, J.S, Boyce, M.C., 1998. Constitutive modeling of the large strain time-dependent behavior of elastomers. Journal of the Mechanics and Physics of Solids 46, 931-954.

Bhattacharya, S., Samanta, S.K., 2016. Soft-nanocomposites of nanoparticles and nanocarbons with supramolecular and polymer gels and their applications. Chemical Reviews 116, 11967-12028.

Boutaleb, S., Zaïri, F., Mesbah, A., Naït-Abdelaziz, M., Gloaguen, J.M., Boukharouba, T., Lefebvre, J.M., 2009. Micromechanics-based modelling of stiffness and yield stress for silica/polymer nanocomposites. International Journal of Solids and Structures 46, 1716-1726.

Chen, H., Liu, Y., Ren, B., Zhang, Y., Ma, J., Xu, L., Chen, Q., Zheng, J., 2017. Super bulk and interfacial toughness of physically crosslinked double-network hydrogels. Advanced Functional Materials 27, 1703086.

Cherief, M.N.D., Zaïri, F., Ding, N., Gloaguen, J.M., Naït-Abdelaziz, M., Benguediab, M., 2020. Plasticity and thermally-induced recovery in polycarbonate. Mechanics of Materials 148, 103515.

Dai, L., Tian, C., Xiao, R., 2020. Modeling the thermo-mechanical behavior and constrained recovery performance of cold-programmed amorphous shape-memory polymers. International Journal of Plasticity 127, 102654.

Dargazany, R., Khiem, V.N., Itskov, M., 2014. A generalized network decomposition model for the quasi-static inelastic behavior of filled elastomers. International Journal of Plasticity 63, 94-109.

Deng, Z., Hu, T., Lei, Q., He, J., Ma, P.X., Guo, B., 2019. Stimuli-responsive conductive nanocomposite hydrogels with high stretchability, self-healing, adhesiveness, and 3D printability for human motion sensing. ACS Applied Materials and Interfaces 11, 6796–6808.

Drozdov, A.D., Christiansen, J.D., 2018. Nanocomposite gels with permanent and transient junctions under cyclic loading. Macromolecules 51, 1462-1473.

Drozdov, A.D., Christiansen, J. de C., 2020. Tension-compression asymmetry in the mechanical response of hydrogels. Journal of the Mechanical Behavior of Biomedical Materials 110, 103851.

Farahani, R.D., Dubé, M., Therriault, D., 2016. Three-dimensional printing of multifunctional nanocomposites: Manufacturing techniques and applications. Advanced Materials 28, 5794-821.

Guo, Q., Zaïri, F., 2021. A micromechanics-based model for deformation-induced damage and failure in elastomeric media. International Journal of Plasticity 140, 102976.

Guo, Q., Zaïri, F., 2020. A physically-based thermo-mechanical model for stretch-induced crystallizable rubbers: Crystallization thermodynamics and chain-network crystallization anisotropy. International Journal of Plasticity 131, 102724.

Guo, Y., Bae, J., Zhao, F., Yu, G., 2019. Functional hydrogels for next-generation batteries and supercapacitors. Trends in Chemistry 1, 335-348.

Guo, Q., Zaïri, F., Guo, X., 2018. A thermo-viscoelastic-damage constitutive model for cyclically loaded rubbers. Part I: Model formulation and numerical examples. International Journal of Plasticity 101, 106-124.

Guo, J., Long, R., Mayumi, K., Hui, C.Y., 2016. Mechanics of a dual cross-link gel with dynamic bonds: Steady state kinetics and large deformation effects. Macromolecules 49, 3497-3507.

Gurtin, M.E., Anand, L., 2005. The decomposition F=FeFp, material symmetry, and plastic irrotationality for solids that are isotropic-viscoplastic or amorphous. International Journal of Plasticity 21, 1686-1719.

Haraguchi, K., Takehisa, T., Fan, S., 2002. Effects of clay content on the properties of nanocomposite hydrogels composed of poly (N-isopropylacrylamide) and clay. Macromolecules 35, 10162-10171.

Holzapfel, G., Simo, J., 1996. Entropy elasticity of isotropic rubber-like solids at finite strains. Computer Methods in Applied Mechanics and Engineering 132, 17-44.

Ju, J.W., Sun, L.Z., 1999. A novel formulation for exterior point Eshelby's tensor of an ellipsoidal inclusion. Journal of Applied Mechanics 66, 570-574.

Kulcu, I.D., 2019. Characterization of stress softening and self-healing in a double network hydrogel. Results in Physics 12, 1826-1833.

Kumar, G.G., Hashmi, S., Karthikeyan, C., GhavamiNejad, A., Vatankhah-Varnoosfaderani, M., Stadler, F.J., 2014. Graphene oxide/carbon nanotube composite hydrogels-versatile materials for microbial fuel cell applications. Macromolecular Rapid Communications 35, 1861-1865.

Li, Y., He, Y., Liu, Z., 2017. A viscoelastic constitutive model for shape memory polymers based on multiplicative decompositions of the deformation gradient. International Journal of Plasticity 91, 300-317.

Li, Y., Tang, S., Kroger, M., Liu, W.K., 2016. Molecular simulation guided constitutive modeling on finite strain viscoelasticity of elastomers. Journal of the Mechanics and Physics of Solids 88, 204-226

Lima-Tenorio, M.K., Tenorio-Neto, E.T., Guilherme, M.R., Garcia, F.P., Nakamura, C.V., Pineda, E.A.G., Rubira, A.F., 2015. Water transport properties through starch-based hydrogel nanocomposites responding to both pH and a remote magnetic field. Chemical Engineering Journal 259, 620-629.

Lin, J., Zheng, S.Y., Xiao, R., Yin, J., Wu, Z.L., Zheng, Q., Qian, J., 2020. Constitutive behaviors of tough physical hydrogels with dynamic metal-coordinated bonds. Journal of the Mechanics and Physics of Solids 139, 103935.

Liu, Y., Zhang, H., Zheng, Y., 2016. A micromechanically based constitutive model for the inelastic and swelling behaviors in double network hydrogels. Journal of Applied Mechanics 83, 021008.

Liu, H., Peng, H., Xin, Y., Zhang, J., 2019. Metal-organic frameworks: A universal strategy towards super-elastic hydrogels. Polymer Chemistry 10, 2263-2272.

Long, R., K. Mayumi, C., Creton, T., Narita, Hui C.Y., 2014. Time dependent behavior of a dual cross-link self-healing gel: Theory and experiments. Macromolecules, 47, 7243-7250.

Lu, T., Wang, Z., Tang, J., Zhang, W., Wang, T., 2020. A pseudo-elasticity theory to model the strain-softening behavior of tough hydrogels. Journal of the Mechanics and Physics of Solids 2020, 103832.

Mahjoubi, H., Zaïri, F., Tourki, Z., 2019. A micro-macro constitutive model for strain-induced molecular ordering in biopolymers: application to polylactide over a wide range of temperatures. International Journal of Plasticity 123, 38-55.

Mai, T.T., Matsuda, T., Nakajima, T., Gong, J.P., Urayama, K., 2018. Distinctive characteristics of internal fracture in tough double network hydrogels revealed by various modes of stretching. Macromolecules 51, 5245-5257.

Mao, Y., Lin, S., Zhao, X., Anand, L., 2017. A large deformation viscoelastic model for double-network hydrogels. Journal of the Mechanics and Physics of Solids 100, 103-130.

Merino, S., Martin, C., Kostarelos, K., Prato, M., Vazquez, E., 2015. Nanocomposite hydrogels: 3D polymer-nanoparticle synergies for on-demand drug delivery. ACS Nano 9, 4686-4697.

Morovati, V., Dargazany, R., 2019. Micro-mechanical modeling of the stress softening in double-network hydrogels. International Journal of Solids and Structures 164, 1-11.

Sarvestani, A.S., He, X., Jabbari, E., 2008. The role of filler-matrix interaction on viscoelastic response of biomimetic nanocomposite hydrogels. Journal of Nanomaterials 2008, 1-9.

Schexnailder, P., Schmidt, G., 2009. Nanocomposite polymer hydrogels. Colloid and Polymer Science 287, 1-11.

Shao, C., Chang, H., Wang, M., Xu, F., Yang, J., 2017. High-strength, tough, and self-healing nnocomposite physical hydrogels based on the synergistic effects of dynamic hydrogen bond and dual coordination bonds. ACS Applied Materials and Interfaces 9, 28305-28318.

Shen, F., Kang, G., Lam, Y.C., Liu, Y., Zhou, K., 2019. Thermo-elastic-viscoplastic-damage model for self-heating and mechanical behavior of thermoplastic polymers. International Journal of Plasticity 121, 227-243.

Shi, F.K., Wang, X.P., Guo, R.H., Zhong, M., Xie, X.M., 2015. Highly stretchable and super tough nanocomposite physical hydrogels facilitated by the coupling of intermolecular hydrogen bonds and analogous chemical crosslinking of nanoparticles. Journal of Materials Chemistry B 3, 1187-1192.

Su, X., Peng, X., 2018. A 3D finite strain viscoelastic constitutive model for thermally induced shape memory polymers based on energy decomposition. International Journal of Plasticity 110, 166-182.

Sun, J.Y., Zhao, X., Illeperuma, W.R.K., Chaudhuri, O., Oh, K.H., Mooney, D.J., Vlassak, J.J., Suo, Z., 2012. Highly stretchable and tough hydrogels. Nature 489, 133-136.

Thakur, S., Govender, P.P., Mamo, M.A., Tamulevicius, S., Mishra, Y.K., Thakur, V.K., 2017a. Progress in lignin hydrogels and nanocomposites for water purification: Future perspectives. Vacuum 146, 342-355.

Thakur, S., Govender, P.P., Mamo, M.A., Tamulevicius, S., Thakur, V.K., 2017b. Recent progress in gelatin hydrogel nanocomposites for water purification and beyond. Vacuum 146, 396-408.

Vernerey, F.J., Long, R., Brighenti, R., 2017. A statistically-based continuum theory for polymers with transient networks. Journal of the Mechanics and Physics of Solids 107, 1-20.

Vernerey, F.J., 2018. Transient response of nonlinear polymer networks: A kinetic theory. Journal of the Mechanics and Physics of Solids 115, 230-247.

Vernerey, F.J., Brighenti, R., Long, R., Shen, T., 2018. Statistical damage mechanics of polymer networks. Macromolecules 51, 6609-6622.

Wang, Q., Gao, Z., 2016. A constitutive model of nanocomposite hydrogels with nanoparticle crosslinkers. Journal of the Mechanics and Physics of Solids 94, 127-147.

Wang, Q., Gao, Z., Yu, K., 2017. Interfacial self-healing of nanocomposite hydrogels: Theory and experiment. Journal of the Mechanics and Physics of Solids 109, 288-306.

Xiang, Y., Zhong, D., Wang, P., Yin, T., Zhou, H., Yu, H., Baliga, C., Qu, S., Yang, W., 2019. A physically based visco-hyperelastic constitutive model for soft materials. Journal of the Mechanics and Physics of Solids 128, 208-218.

Xiao, R., Mai, T.T., Urayama, K., Gong, J.P., Qu, S., 2021. Micromechanical modeling of the multi-axial deformation behavior in double network hydrogels. International Journal of Plasticity 137, 102901.

Xu, C., Dai, G., Hong, Y., 2019. Recent advances in high-strength and elastic hydrogels for 3D printing in biomedical applications. Acta Biomaterialia 5, 50-59.

Yang, Q., Li, G., 2016. Temperature and rate dependent thermomechanical modeling of shape memory polymers with physics based phase evolution law. International Journal of Plasticity 80, 168-186.

Yang, B., Yao, F., Hao, T., Fang, W., Ye, L., Zhang, Y., Wang, Y., Li, J., Wang, C., 2016. Development of electrically conductive double-network hydrogels via one-step facile strategy for cardiac tissue engineering. Advanced Healthcare Materials 5, 474-488.

Yin, H.M., Sun, L.Z., Chen, J.S., 2002. Micromechanics-based hyperelastic constitutive modeling of magnetostrictive particle-filled elastomers. Mechanics of Materials 34, 505-516.

Yu, K., Xin, A., Wang, Q., 2018. Mechanics of self-healing polymer networks crosslinked by dynamic bonds. Journal of the Mechanics and Physics of Solids 121, 409-431

Zaïri, F., Gloaguen, J.M., Naït-Abdelaziz, M., Mesbah, A., Lefebvre, J.M., 2011. Study of the effect of size and clay structural parameters on the yield and post-yield response of polymer/clay nanocomposites via a multiscale micromechanical modelling. Acta Materialia 59, 3851-3863.

Zhai, X., Ma, Y., Hou, C., Gao, F., Zhang, Y., Ruan, C., Pan, H., Lu, W.W., Liu, W., 2017. 3D-printed high strength bioactive supramolecular polymer/clay nanocomposite hydrogel scaffold for bone regeneration. ACS Biomaterials Science and Engineering 3, 1109-1118.

Zhang, W., Feng, P., Chen, J., Sun, Z., Zhao, B., 2019. Electrically conductive hydrogels for flexible energy storage systems. Progress in Polymer Science 88, 220-240.

Zhou, J., Jiang, L., Khayat, R.E., 2018. A micro-macro constitutive model for finite-deformation viscoelasticity of elastomers with nonlinear viscosity. Journal of the Mechanics and Physics of Solids 110, 137-154.

Zhu, P., Zhong, Z., 2020. Modelling the mechanical behaviors of double-network hydrogels. International Journal of Solids and Structures 193-194, 492-501.

Chapter III

A micromechanical model for the swelling effect on visco-super-elastic and damage self-healing behaviors of hydrogels reinforced by nanoparticles

CHAPTER III

A micromechanical model for the swelling effect on visco-super-elastic and damage self-healing behaviors of hydrogels reinforced by nanoparticles [2]

In the present chapter, a micromechanical model is developed for the visco-super-elastic behavior of swollen hydrogel-based nanocomposites. The model formulated in a finite strain context introduces explicitly the hydrogel network features in terms of swelling and dynamic breaking-recombination. The effective interactions between the nanoparticles and the swollen hydrogel network are considered using a micro-macro scale transition within the Eshelby inclusion theory. The model is compared to experimental observations of a high-swelling capacity hydrogel-based nanocomposite reinforced with different concentrations of nanoparticles. The model is firstly identified using experimental data at an initial swelling state in terms of stress-strain response, energy dissipation and ultimate properties. The predictive capability of the model is then verified on a wide range of swelling ratios for a given nanofiller concentration. The efficiency of the model is further critically discussed by comparisons with history-dependent data under stretching-retraction and self-healing. The effects of nanoparticles and swelling on the self-healing behavior are shown thanks to the model.

Keywords: *Hydrogel-based nanocomposites; Multiscale modeling; Swelling; Visco-super-elastic behavior; Damage self-healing.*

[2] This chapter is based on the following paper: Saadedine, M., Zaïri, F., Ouali, N., Tamoud, A., Ding, N., Mesbah, A., 2022. A micromechanical model for the swelling effect on visco-super-elastic and damage self-healing behaviors of hydrogels reinforced by nanoparticles. Mechanics of Materials 104511.

III.1 Partial introduction

Hydrogel-based nanocomposites are three-dimensional cross-linked polymer networks immersed in a solvent and reinforced by a nano-sized inorganic second phase. The nano-scale reinforcement leads to impressive improvements of mechanical properties including extreme resilience, extreme stretchability, strong mechanical strength and extreme facile room temperature self-healing (Sun et al., 2012; Shi et al., 2015; Chen et al., 2017; Liu et al., 2019). Numerous experimental studies established a correlation between the swelling effects and the mechanical properties of hydrogels (Urayama et al., 2008; Zhao et al., 2010; Konda et al., 2011; Lou et al., 2012). The interplay between the effects of cross-linked hydrogel network features and swelling capacity, i.e. physical association between the chains and the solvent molecules, is qualitatively well understood. Nonetheless, the mechanisms of nanofillers reinforcement and their changes due to the hydrogel swelling state are far to be fully understood.

Over the years, constitutive models of swollen hydrogel mechanics were proposed. Wineman and Rajagopal (1992) proposed a particular free energy function for polymer gels based on the Mooney-Rivlin model and the Flory-Huggins mixing theory, which was also used by Deng and Pence (2010, 2010) to examine the mechanical reactions of saturated and unsaturated polymer gels. Dolbow et al. (2004) modified the Neo-Hookean model to study the chemical-induced swelling of hydrogels. Hong et al. (2008) formulated a constitutive model taking into account the nonlinear large deformation based on the Flory-Rehner equation, which was widely adopted to study the chemo-mechanical coupling in hydrogels (Wang and Wu, 2013; Guo et al., 2016; Lai and Hu, 2017). Drozdov and Christiansen (2013) derived a novel expression for free energy density of a swollen elastomer based on the Flory theory of polymer networks with constrained junctions. Several researchers proposed to model the chemo-mechanical behavior of hydrogels in the framework of the multiplicative decomposition of the deformation into mechanical and swelling parts (Duda et al., 2010; Chester and Anand, 2010).

Chester and Anand (2010, 2011) introduced the Arruda-Boyce model to the Flory-Rehner theory taking the chain extensibility into account to study the effect of the transient swelling response of a constrained gel predicted by Gaussian and non-Gaussian network theories. Li et al. (2014) integrates the Gent model to the Flory-Rehner theory to investigate the effect of limiting chain extensibility. Okumura et al. (2016, 2018) used two scaling exponents to estimate the strain energy functions separated into isochoric and volumetric parts. Their model successfully reproduced the effect of swelling on Young's modulus for several combinations of elastomer and solvent. Recently, they incorporate the Arruda-Boyce and Gent models using limiting chain extensibility into the Flory-Rehner theory to study the ultimate swelling of elastomers (Okumura and Chester, 2018).

Most of constitutive models consider the mechanics of the neat hydrogel and only a very few introduced the presence of fillers (Wang and Gao, 2016; Wang et al., 2017; Saadedine et al., 2021). In order to constitutively describe the overall visco-super-elastic response of hydrogels reinforced by inorganic nanoparticles, we formulated in a previous chapter (Saadedine et al., 2021) a micromechanics-based model in which the effective interactions with the nanoparticles were integrated by means of the Eshelby equivalent inclusion method within a finite strain context and the eight-chain cube context to consider as well the internal hydrogel network structure and the large nonlinear response. The objective of this chapter is to further develop the model by taking into account the hydrogel swelling state in order to provide a quantitative prediction of the visco-super-elastic response of swollen hydrogel-based nanocomposites. The model is applied on a high-swelling capacity hydrogel-based nanocomposite reinforced with different concentrations of nanoparticles. Monotonic stretching till failure, stretching-retraction and self-healing properties, all largely depend on the swelling state, are used to verify the model capacities. The swelling-induced changes in both dynamic breaking-recombination mechanism and strength of interactions with nanofillers are pointed out thanks to the model.

.

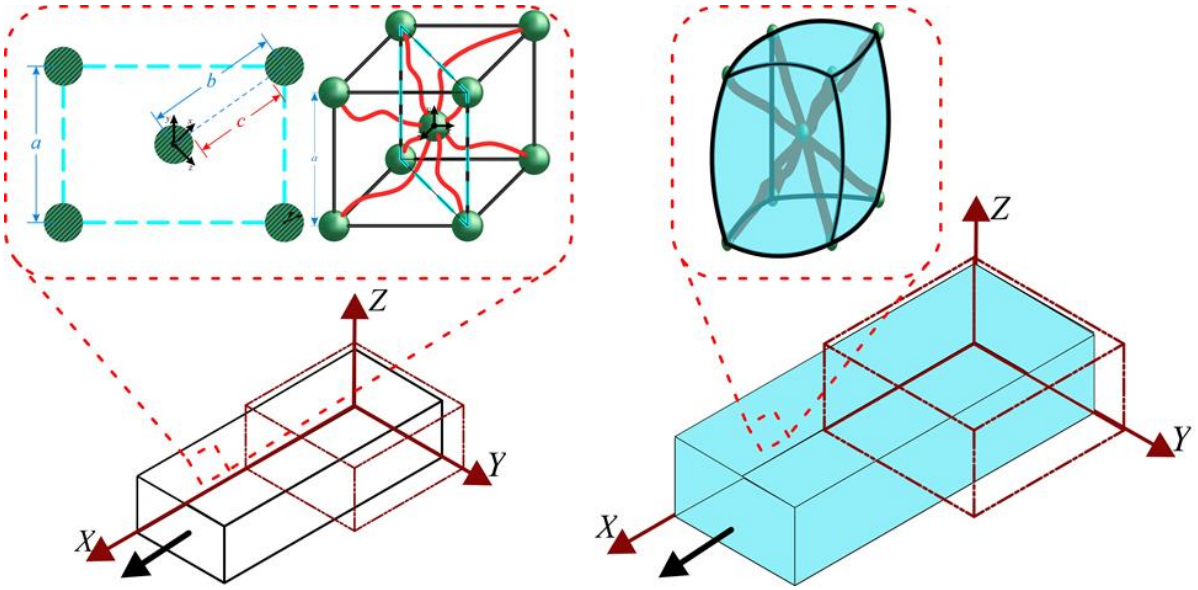

(a)

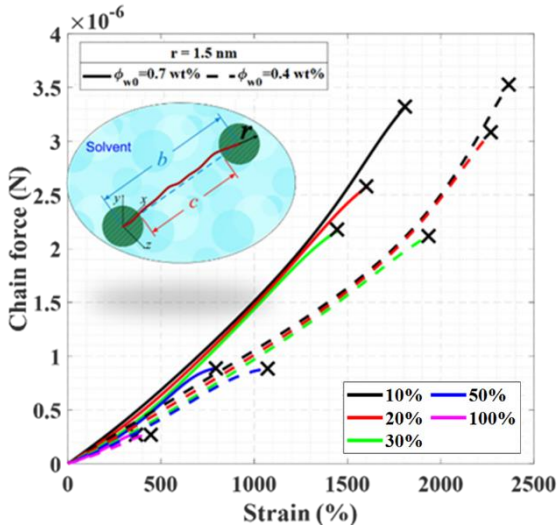

(b)

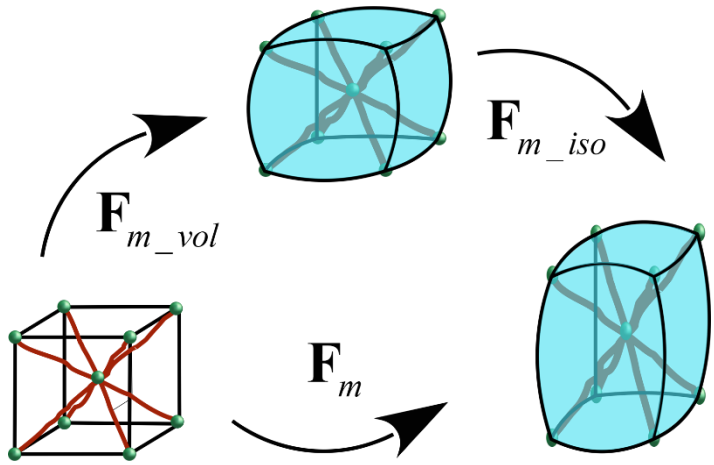

(c)

Figure III.1 Hydrogel-based nanocomposites seen as (a) a cubic material volume containing eight chains interconnected to nine spherical nanoparticles and accounting for the swelling-induced volume change (b) which acts locally on the chain response by inducing a loss of stretchability (the chain force is plotted, until the peak appearance corresponding to the failure, for two amounts of nanoparticles at a given radius and different swelling ratios) and (c) which is described within the finite strain kinematics framework via the multiplicative decomposition concept of the deformation gradient.

The following notation is used throughout the text. Tensors and vectors are denoted by normal boldfaced letters and italicized boldfaced letters, respectively, while scalars and individual components of vectors and tensors are denoted by normal italicized letters. The superposed dot designates the time derivative. The superscript T indicates the transpose quantity. The overbar defines the macroscopic quantities of the nanocomposite while the subscripts *m* and *p* are used to differentiate matrix and nanoparticles, respectively.

III.2 Model formulation

In our previous work (Saadedine et al., 2021), we constitutively represented the hydrogel-based nanocomposite by the cubic unit cell illustrated in (Figure III.1a) Eight chains are interconnected to nine spherical nanoparticles, eight nanoparticles being located in the vertices of the cube and one in the center. The microstructure of the swollen hydrogel-based nanocomposite is defined by four key elements: the average number of chains per unit unswelled volume n, the average number of statistical links in a chain N, the nanoparticles volume fraction in the dry nanocomposite ϕ_0 and the volume change of the gel J. Each hydrogel chain has ultrahigh elongation capacities and is viewed as viscoelastic in accordance with the tube-constraints concept. Dynamic bonds between hydrogel chains and nanoparticles are integrated to capture the damage behavior and self-healing of the nanocomposite. The whole will confer to the overall response visco-super-elastic properties. We propose here to incorporate the swelling for a more accurate description of the visco-super-elastic behavior by considering the swelling-induced loss of chain extensibility and of reinforcement efficiency. An illustrative example of the interplay between the swelling and the chain behavior can be observed in (Figure III.1b) for two nanoparticle amounts while the radius is kept constant.

III.2.1 Free energy

From a simple topological-based analysis of the cubic unit cell for the micro-macro mapping, the free energy of the nanocomposite $\bar{\psi}$ may be expressed as a function of the free energy of the swollen hydrogel matrix ψ_m and the free energy of the nanoparticles ψ_p (Saadedine et al., 2021):

$$\bar{\psi} = (1-2\rho)\psi_m + \phi\psi_p \tag{III.1}$$

where $\phi = \phi_0 / J$ is the actual nanoparticles volume fraction and ρ is the ratio between the nanoparticle radius r and the center-to-center distance b between the central nanoparticle and a neighboring nanoparticle (see Figure III.1). To consider the increasing inter-particle distance with the swelling, the latter is re-written as a function of the initial nanoparticles volume fraction as:

$$\rho = \left(\frac{\phi_0}{\sqrt{3}\pi J} \right)^{1/3} \tag{III.2}$$

After a series of straightforward derivations of the relation between the chain end-to-end vector $\boldsymbol{c}$ and the vectors $\boldsymbol{b}$ and $\boldsymbol{r}$ using a simple topological-based analysis of the cubic unit cell, the deformation of the nanocomposite is given by (Saadedine et al., 2021):

$$\bar{\mathbf{F}} = (1-2\rho)\mathbf{F}_m + 2\rho\mathbf{F}_p \tag{III.3}$$

where $\mathbf{F}_m$ is the deformation gradient of the swollen hydrogel matrix and $\mathbf{F}_p$ is the deformation gradient of the nanoparticles.

III.2.1.1 Swollen hydrogel matrix

The finite strain kinematics of swollen hydrogels is introduced via the multiplicative decomposition concept illustrated in (Figure III.1c) The free energy of the swollen hydrogel matrix ψ_m is expressed with the formulation developed by Boyce and Arruda (2001) to consider the changes in configurational entropy due to the combined effect of swelling and mechanical stretching in limiting chain extensibility:

$$\psi_m = \upsilon_m n k_B T N \left(\beta_{\text{iso}} \frac{\sqrt{I^e_{1m\_\text{iso}}/3}}{\sqrt{N}} + \ln\left(\frac{\beta_{\text{iso}}}{\sinh \beta_{\text{iso}}} \right) - \beta_{\text{vol}} \frac{\sqrt{I_{1m\_\text{vol}}/3}}{\sqrt{N}} - \ln\left(\frac{\beta_{\text{vol}}}{\sinh \beta_{\text{vol}}} \right) \right) \quad \text{(III.4)}$$

where k_B is the Boltzmann constant, T is the temperature and υ_m is the volume fraction of polymer matrix relative to the dry state defined here as follows: $\upsilon_m = \left((1-\phi)/\sqrt{3}J \right)^2$. The functions β_{iso} and β_{vol} are defined, respectively, as:

$$\beta_{\text{iso}} = \mathcal{L}^{-1}\left(\sqrt{I^e_{1m\_\text{iso}}/3} \Big/ \sqrt{N} \right) \text{ and } \beta_{\text{vol}} = \mathcal{L}^{-1}\left(\sqrt{I_{1m\_\text{vol}}/3} \Big/ \sqrt{N} \right) \quad \text{(III.5)}$$

in which β_{iso} and β_{vol} define the inverse of the Langevin function $\mathcal{L}(x) = \coth(x) - 1/x$ which can be treated by a Padé approximation: $\mathcal{L}^{-1}(x) \approx x(3-x^2)/(1-x^2)$, $I^e_{1m\_\text{iso}} = \text{trace}\left(\mathbf{C}^e_{m\_\text{iso}} \right)$ and $I_{1m\_\text{vol}} = \text{trace}\left(\mathbf{C}_{m\_\text{vol}} \right)$ are the first invariants of the isochoric part $\mathbf{C}^e_{m\_\text{iso}} = \mathbf{F}^{e^T}_{m\_\text{iso}} . \mathbf{F}^e_{m\_\text{iso}}$ and the volumetric part $\mathbf{C}_{m\_\text{vol}} = \mathbf{F}^T_{m\_\text{vol}} . \mathbf{F}_{m\_\text{vol}}$ of the right Cauchy-Green deformation tensor with the deformation gradients $\mathbf{F}^e_{m\_\text{iso}}$ and $\mathbf{F}_{m\_\text{vol}}$ coming from the multiplicative decomposition: $\mathbf{F}_m = \mathbf{F}_{m\_\text{iso}} . \mathbf{F}_{m\_\text{vol}}$ and $\mathbf{F}_{m\_\text{iso}} = \mathbf{F}^e_{m\_\text{iso}} . \mathbf{F}^v_{m\_\text{iso}}$. The superscripts *e* and *v* denote the elastic and viscous components, respectively. In view of these transformations, the volume change is defined as $J_m = J_{m\_\text{vol}}$ since $J_{m\_\text{iso}} = 1$ for the isochoric part and $\mathbf{F}_{m\_\text{vol}} = J_m^{1/3}\mathbf{I}$ and $\mathbf{F}_{m\_\text{iso}} = J_m^{-1/3}\mathbf{F}_m$ where $\mathbf{I}$ is the unit tensor. The time derivative of the deformation gradient writes $\dot{\mathbf{F}}_{m\_\text{iso}} = \mathbf{L}_{m\_\text{iso}} \mathbf{F}_{m\_\text{iso}}$ where $\mathbf{L}_{m\_\text{iso}} = \mathbf{L}^e_{m\_\text{iso}} + \mathbf{L}^v_{m\_\text{iso}}$ is the gradient of the spatial velocity with $\mathbf{L}^e_{m\_\text{iso}} = \dot{\mathbf{F}}^e_{m\_\text{iso}} \mathbf{F}^{e^{-1}}_{m\_\text{iso}}$ and $\mathbf{L}^v_{m\_\text{iso}} = \mathbf{F}^e_{m\_\text{iso}} \dot{\mathbf{F}}^v_{m\_\text{iso}} \mathbf{F}^{v^{-1}}_{m\_\text{iso}} \mathbf{F}^{e^{-1}}_{m\_\text{iso}}$. The latter tensor is further additively decomposed into a symmetric part $\mathbf{D}^v_{m\_\text{iso}} = \left(\mathbf{L}^v_{m\_\text{iso}} + \mathbf{L}^{v^T}_{m\_\text{iso}} \right)/2$ (viscous stretching rate) and a skew-symmetric part $\mathbf{W}^v_{m\_\text{iso}} = \left(\mathbf{L}^v_{m\_\text{iso}} - \mathbf{L}^{v^T}_{m\_\text{iso}} \right)/2$ (viscous spin).

By choosing the viscous flow irrotational (Gurtin and Anand, 2005), i.e. $\mathbf{W}^{v}_{m\_\mathrm{iso}} = \mathbf{0}$, the evolution equation of the viscous deformation gradient is given by:

$$\dot{\mathbf{F}}^{v}_{m\_\mathrm{iso}} = \mathbf{F}^{e^{-1}}_{m\_\mathrm{iso}} \mathbf{D}^{v}_{m\_\mathrm{iso}} \mathbf{F}^{e}_{m\_\mathrm{iso}} \mathbf{F}^{v}_{m\_\mathrm{iso}} \tag{III.6}$$

The elastic deformation gradient is then extracted from the multiplicative decomposition: $\mathbf{F}^{e}_{m\_\mathrm{iso}} = \mathbf{F}_{m\_\mathrm{iso}} \mathbf{F}^{v^{-1}}_{m\_\mathrm{iso}}$. The viscous stretching rate tensor $\mathbf{D}^{v}_{m\_\mathrm{iso}}$ is given by the following flow rule:

$$\mathbf{D}^{v}_{m\_\mathrm{iso}} = \dot{\gamma}^{v}_{m} \frac{\boldsymbol{\sigma}_{m\_\mathrm{iso}}}{\|\boldsymbol{\sigma}_{m}\|} \text{ with } \|\boldsymbol{\sigma}_{m}\| = \sqrt{\mathrm{trace}\left(\boldsymbol{\sigma}_{m\_\mathrm{iso}} . \boldsymbol{\sigma}^{T}_{m\_\mathrm{iso}}\right)} \tag{III.7}$$

where $\boldsymbol{\sigma}_{m\_\mathrm{iso}} = \boldsymbol{\sigma}_{m} - 1/3\,\mathrm{trace}\left(\boldsymbol{\sigma}_{m}\right)\mathbf{I}$ is the isochoric part of the Cauchy stress tensor $\boldsymbol{\sigma}_{m}$, $\|\boldsymbol{\sigma}_{m}\|$ is the effective stress by the Frobenius norm and $\dot{\gamma}^{v}_{m}$ is the accumulated viscous strain rate that can be expressed as a function of the effective stress using the viscoplasticity theory but without yield surface such that the elastic and inelastic strain rates are non-zero at all deformation stages (Zaïri et al., 2007): $\dot{\gamma}^{v}_{m} = \dot{\gamma}^{v}_{m}\left(\|\boldsymbol{\sigma}_{m}\|\right)$.

III.2.1.2 Nanoparticles

Empirical approaches are largely used in the literature to deal with reinforced polymers by considering the inorganic reinforcement only through the volume fraction concept, possibly coupled with an empirical amplification factor (Ovalle-Rodas et al., 2015; Guo et al., 2018). Although the effective effect of the volume fraction is well considered, the local interaction between matrix and inorganic reinforcement is not physically consistent or completely disregarded. In the present approach, the local interaction is considered through micromechanical assessments and the Eshelby equivalent inclusion method providing an approximate solution for the problem of one particle embedded in an infinite domain. The Eshelbian homogenization

framework consists to replace the particle domain by the matrix material via the introduction of an eigenstrain replacing the perturbed strain induced by the inhomogeneity, the averaged eigenstrain of a particle interacting with its neighboring nanoparticles being obtained by means of the Green function technique. Dealing with large-strain mechanical response of hydrogel nanocomposites, the theoretical framework is here provided within the finite-strain kinematics framework More details on the developments are given in the Appendix of the previous chapter. The following formulation is used for the free energy of the nanoparticles ψ_p (Yin et al., 2002):

$$\psi_p = \left(\frac{\lambda_p}{2} \left(\chi_1 + 3\chi_2 \right)^2 + \mu_p \left(2\chi_1\chi_2 + 3\chi_2^2 \right)^2 \right) \bar{\varepsilon}_{\text{vol}}^2 + \mu_p \chi_1^2 \bar{\boldsymbol{\varepsilon}}_{\text{iso}} : \bar{\boldsymbol{\varepsilon}}_{\text{iso}} \tag{III.8}$$

where $\bar{\varepsilon}_{\text{vol}}$ is the Hencky volumetric strain, $\bar{\boldsymbol{\varepsilon}}_{\text{iso}} = \ln \bar{\mathbf{F}}_{\text{iso}}$ is the isochoric Hencky strain tensor, λ_p and μ_p are the Lame's constants and, χ_1 and χ_2 are given by:

$$\chi_1 = \frac{1}{2w - M - \phi} \frac{\mu_m}{\mu_p - \mu_m} \text{ and } \chi_2 = \frac{1}{3\left(2w + 3m - M - \phi\right)} \frac{K_m}{K_p - K_m} - \frac{1}{3}\chi_1 \tag{III.9}$$

where K_m and K_p are the bulk moduli, $\mu_m = \upsilon_m n k_B T$ and μ_p are the shear moduli and, m, w and M are given by:

$$m = \frac{1}{3}\left(K_{mp} - \mu_{mp} \right) + \frac{5\nu_m - 1}{15\left(1 - \nu_m\right)} + \frac{M}{5},\ w = \frac{\mu_{mp}}{2} + \frac{4 - 5\nu_m}{15\left(1 - \nu_m\right)} + \frac{M}{5},\ M = \frac{40\left(14\rho^2 - 5\right)\rho^3}{45\left(1 - \nu_m\right)} \tag{III.10}$$

with $K_{mp} = K_m / \left(K_p - K_m \right)$, $\mu_{mp} = \mu_m / \left(\mu_p - \mu_m \right)$ and ν_m is the Poisson's ratio.

The time derivative of the deformation gradient is $\dot{\mathbf{F}}_p = \mathbf{L}_p \mathbf{F}_p$ with $\mathbf{L}_p$ the gradient of the spatial velocity that may be expressed through the Eshelbian homogenization solution in the finite strain context using the Saint Venant-Kirchhoff assumption (Yin et al., 2002):

$$\mathbf{L}_p = \mathbf{A}.\boldsymbol{\Gamma}.\left(\mathbf{I} - \phi\boldsymbol{\Gamma} \right)^{-1} : \bar{\mathbf{L}} \tag{III.11}$$

where $\mathbf{A}$ is the mismatch tensor:

$$\mathbf{A} = \left(\mathbf{K}_p - \mathbf{K}_m\right)^{-1}.\mathbf{K}_m \tag{III.12}$$

in which $\mathbf{K}_m$ and $\mathbf{K}_p$ are the stiffness tensors.

The term $\boldsymbol{\Gamma}$ is a tensor given by:

$$\Gamma_{ijkl} = \left(\frac{-m}{\left(2w - M\right)\left(2w + 3m - M\right)} + \frac{M}{2w\left(2w - M\right)}\delta_{IK} \right)\delta_{ij}\delta_{kl} + \frac{1}{4w}\left(\delta_{ik}\delta_{jl} + \delta_{il}\delta_{jk}\right) \tag{III.13}$$

in which δ_{ij} is the Kronecker delta.

III.2.2 Chains network

In our previous work (Saadedine et al., 2021), the chains network kinetics were formulated to take into account the dynamic breaking and recombination of bonds participating to energy dissipation and quick reconstruction in the recovering. In this work, some refinements are brought to take into account the detachment-reattachment mechanism changes due the presence of the solvent in the hydrogel. The extension of the molecular chains caused by the solvent-induced swelling results in an earlier strain hardening onset and a decrease in extensibility (Figure III.1b). This mechanism may be captured by managing the limiting chain extensibility into our model. For this purpose, the average number of statistical links in a chain N may be expressed as follows (Saadedine et al., 2021):

$$N\left(t\right) = \frac{N\left(t=0\right)}{N_{on/off}} \tag{III.14}$$

where the constraint of *conservation of monomers imposes* $n\left(t\right) = n\left(t=0\right)N_{on/off}$, the quantities $N\left(t=0\right)$ and $n\left(t=0\right)$ being the original values and $N_{on/off}$ is here expressed by the following kinetics:

$$\dot{N}_{on/off} = \upsilon_m\left(1 - N_{on/off}\left(1 + k_{on/off}\right)\right) \tag{III.15}$$

in which $k_{on/off}$ controls the rate of the detachment-reattachment mechanism:

$$k_{on/off} = k_{on/off\_0} \exp\left(\frac{\left\| \boldsymbol{\sigma}_m \right\|}{\sigma_{off} N_{on/off}} \right) \tag{III.16}$$

in which k_{on/off_0} is a material constant and σ_{off} is a scale factor controlling the bonds strength.

To consider the destruction of bonds due to the presence of the solvent and thereby the strength loss, the following relation is here proposed:

$$\sigma_{off} = \frac{1}{3}\sigma_{off\_0} \ln\left(\upsilon_m\right) + \sigma_{off\_0} \tag{III.17}$$

where σ_{off_0} is the initial value.

The swelling state reduces also the inter-chain interaction and thereby the topological constrain of surrounding chains on an individual chain translated by its viscous resistance. The viscous deformation may be understood in the Doi-Edwards tube framework in which the reptational Brownian motion is described as lateral motion restriction of individual chains due to the interaction of the neighboring chains. The accumulated viscous strain rate $\dot{\gamma}_m^v$ takes the form of the Bergstrom-Boyce power law (Bergstrom and Boyce, 1998):

$$\dot{\gamma}_m^v = \frac{k_v}{\left(\sqrt{I_{1m}^v/3} - 1\right)^{\alpha}} \left\| \boldsymbol{\sigma}_m \right\| \tag{III.18}$$

where $I_{1m}^v = \text{trace}\left(\boldsymbol{\varepsilon}_{m\_\text{iso}}^v . \boldsymbol{\varepsilon}_{m\_\text{iso}}^{v^T}\right)$ is the viscous first invariant with $\boldsymbol{\varepsilon}_{m\_\text{iso}}^v = \ln \mathbf{F}_{m\_\text{iso}}^v$ the viscous isochoric Hencky strain tensor, α is the stretch-dependency parameter and k_v is the chains relaxation parameter expressed as follows (Saadedine et al., 2021):

$$k_v = k_{v\_0}\left(1 + \left|\frac{\dot{\lambda}_{\max}}{\dot{\lambda}_0}\right|\right)^{\tau} \exp\left(\text{sgn}\left(\dot{\lambda}_{\max}\right)\right) \tag{III.19}$$

in which k_{v_0} is the viscous multiplier, τ is the rate-dependency factor, $\dot{\lambda}_{\max} = \max\left(\dot{\lambda}_{11}, \dot{\lambda}_{22}, \dot{\lambda}_{33}\right)$ is the maximum stretch rate and $\dot{\lambda}_0$ is the reference loading rate. The term $\text{sgn}\left(\dot{\lambda}_{\max}\right)$ signifies:

$$\mathrm{sgn}\left(\dot{\lambda}_{\max}\right)=\begin{cases}+1 & \text{for stretching} \quad \left(\dot{\lambda}_{\max}>0\right)\\ -1 & \text{for retraction} \quad \left(\dot{\lambda}_{\max}<0\right)\\ 0 & \text{for recovery} \quad \left(\dot{\lambda}_{\max}=0\right)\end{cases} \tag{III.20}$$

When the external load is removed, the dynamic nature of bonds renders the hydrogel with self-healing ability without any external stimulus. The temporarily broken bonds re-attach by following the relations (III.14- III.17) and the strain recovery is simulated by a creep at zero-stress using the following formulae (Saadedine et al., 2021):

$$\left(1-2\rho\right)\boldsymbol{\sigma}_m+\phi\boldsymbol{\sigma}_p=\mathbf{0} \text{ and } \mathbf{F}_m=\frac{1}{1-2\rho}\left(\bar{\mathbf{F}}-2\rho\mathbf{F}_p\right) \tag{III.21}$$

with $\mathbf{F}_m=\mathbf{F}^e_{m\_\mathrm{iso}}.\mathbf{F}^v_{m\_\mathrm{iso}}.\mathbf{F}_{m\_\mathrm{vol}}$. The volume preserving is assumed during the creep process and the viscous deformation gradient tensor $\mathbf{F}^v_{m\_\mathrm{iso}}$ is computed using the following formula (Saadedine et al., 2021):

$$\dot{\mathbf{F}}^v_{m\_\mathrm{iso}}=-\frac{k_v}{\left(\sqrt{I^v_{1m}/3}-1\right)^{\alpha}}\frac{\phi}{1-2\rho}\mathbf{F}^v_{m\_\mathrm{iso}}.\boldsymbol{\sigma}_{p\_\mathrm{iso}} \tag{III.22}$$

Energy dissipation, failure and self-healing properties can be all assessed by the model while the effect of swelling is considered. So, the model can be employed to better understand the changes of the hydrogel swelling state on the mechanisms of nanofillers reinforcement and thus the changes of the interactions with the nanoparticles hindering the relative motion of chains and modifying the intrinsic viscosity. Besides, the bonds tending to preferentially breaking and maximizing the energy dissipation can see their activity modified by the hydrogel swelling state.

III.3 Model application

The micromechanical model has been coded in MATLAB software. The model capacities are checked by comparisons with the available time-dependent data reported by Zhong et al. (2016) of a poly(acrylic acid) hydrogel-based nanocomposite exhibiting strong swelling capacities and

reinforced by vinyl-hybrid silica nanoparticles over a nanofiller amount range from 0 to 1.5 wt%[3]. The initial swelling state corresponds to a swelling ratio of 67%. The model efficiency is checked

Parameter	Significance	Value
μ_p (GPa)	Particle shear modulus	3.2
K_p (GPa)	Particle bulk modulus	160
k_{on/off_0} (s^{-1})	Dynamic bonds	5×10^{-5}
$\dot{\lambda}_0$ (s^{-1})	Reference loading rate	0.01
τ	Rate-dependency	0.2
α	Stretch-dependency	1.4

Table III.2 Model parameters.

on data obtained under different mechanical loading conditions at a constant stretch rate of 0.1 /s and at room temperature. Table III.1 provides a summarize of the available data for the present model application. They include monotonic stretching till failure at different swelling ratios and, stretching-retraction and self-healing measurements at the initial swelling state.

		Nanoparticle weight fraction (wt%)						
		0	0.05	0.1	0.4	0.7	1	1.5
Initial swelling state	Monotonic stretching till failure	MI	MI	MI	MI	MI	MI	MI
	Stretching-retraction			PV	PV	PV		
	Stretching-retraction after recovery period					PV		
	Recovery	MP				MP		
Swollen state	Monotonic stretching till failure					PV		
	Stretching-retraction					MP		
	Stretching-retraction after recovery period					MP		
	Recovery	MP				MP		

Table III.2 Model identification (MI) using monotonic data, model predictability verification (PV) using non-monotonic data and model predictions (MP) showing the swelling effect on microstructure-mechanics relationship.

[3] The nanoparticle weight fraction ϕ_{w0} at the initial swelling state was converted to the nanoparticle volume fraction ϕ_0 by using the following formula: $\phi_0 = \phi_{w0}\left(\phi_{w0} + (1-\phi_{w0})\rho_p/\rho_m\right)^{-1}$ where ρ_p = 2.0 g/cm^3 is the vinyl-hybrid silica nanoparticle density (Sakamoto et al., 2018) and ρ_m = 1.4 g/cm^3 is the *poly(acrylic acid)* hydrogel matrix density (Lira et al., 2009).

The monotonic data at the initial swelling state are used to fit the model. After verification of the model predictability using data not used in the identification exercise, some predictions are performed to highlight the link between microstructure, swelling and overall mechanical response. Unless explicitly otherwise stated, the simulation results are presented at the constant stretch rate of 0.1 /s.

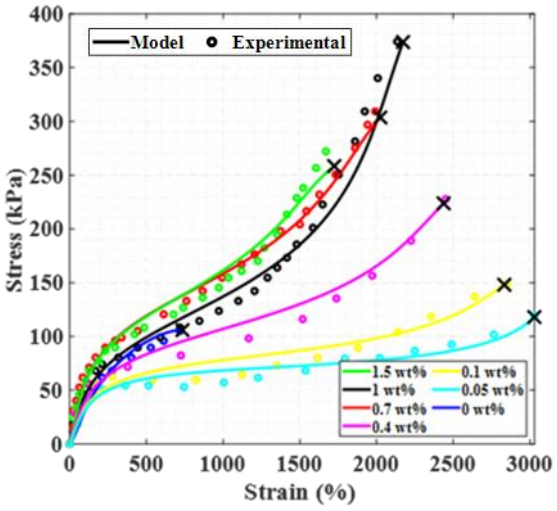

(a)

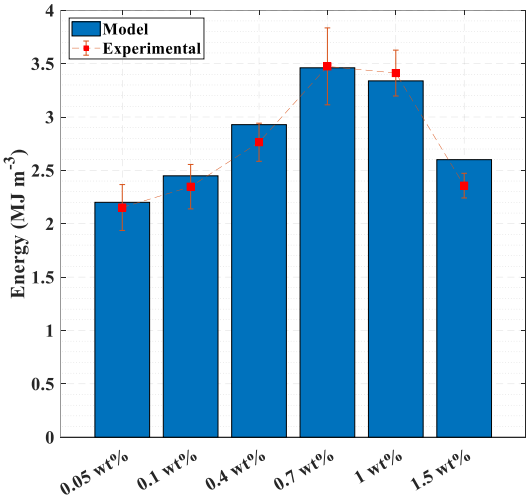

(b)

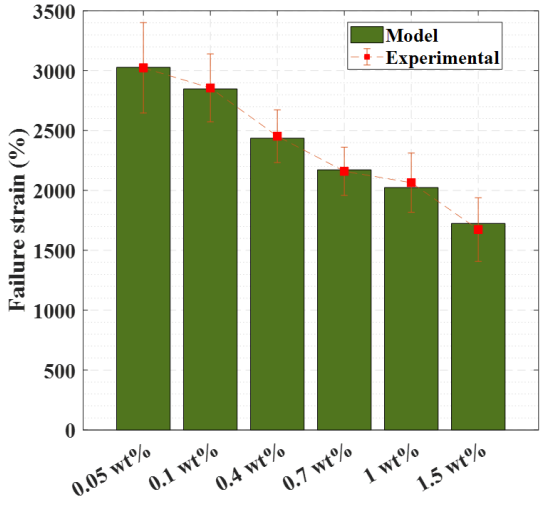

(c)

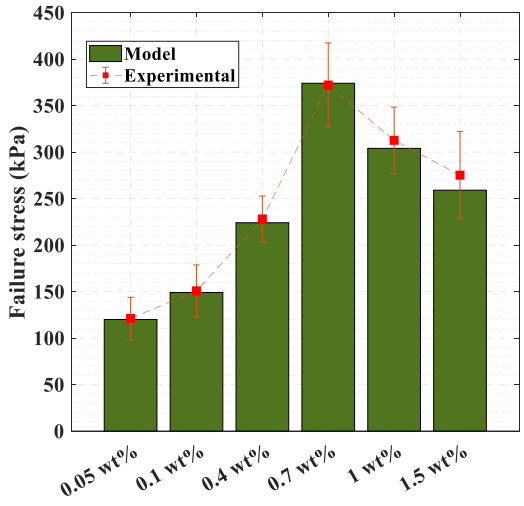

(d)

Figure III.2 Model vs. experimental under monotonic stretching at the initial swelling state for different nanofiller amounts: (a) stress-strain response, (b) toughness, (c) failure strain and (d) failure stress.

III.3.1 Strengthening effect

Figure III.2 presents the computed results of the macro-stress evolution under monotonic stretching at the initial swelling ratio. The model simulations are conducted until the complete loss of load-bearing capability corresponding to the local maximum stress level reached as indicated by the cross. The identified model parameters are provided in Table III.2 and Figure III.3. The values of the experimental data and model outputs are also reported in Table III.3 along with the relative error quantifying the discrepancy.

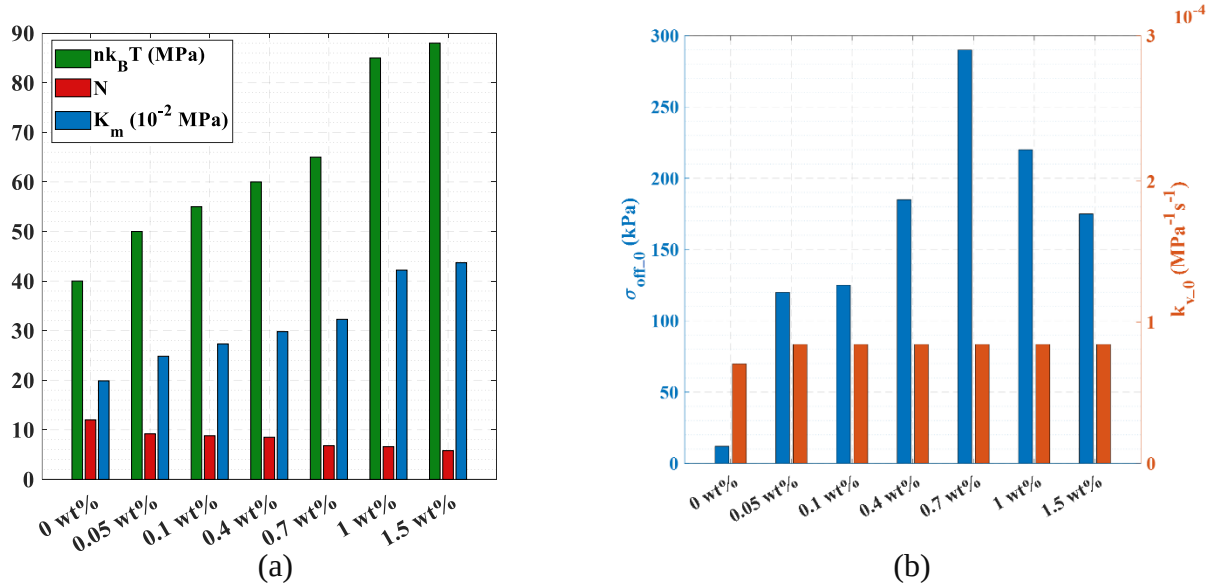

(a) (b)

Figure III.3. Hydrogel matrix characteristics at the initial swelling state for different nanofiller amounts: (a) mean chain density, mean chain length and bulk modulus, (b) bonds strength and viscous multiplier.

	Failure strain (%)		Failure stress (kPa)		Energy (MJ m^{-3})	
Nanoparticle weight fraction (wt%)	Experimental	Model (Errors)	Experimental	Model (Errors)	Experimental	Model (Errors)
0.05	3024	3028 (0.12%)	121	120 (0.85%)	2.15	2.20 (2.25%)
0.1	2857	2848 (0.29%)	151	149 (1.16%)	2.34	2.44 (4.33%)
0.4	2454	2436 (0.71%)	228	224 (1.77%)	2.76	2.92 (5.95%)
0.1	2160	2172 (0.54%)	372	374 (0.50%)	3.47	3.46 (0.39%)
1.0	2065	2024 (1.99%)	313	304 (2.76%)	3.41	3.33 (2.15%)
1.5	1674	1724 (2.98%)	275	259 (5.80%)	2.35	2.60 (10.32%)

Table III.3 Experimental data and model outputs under a monotonic stretching at the initial swelling state for different nanofiller amounts.

The model simulations are in good agreement with the tendencies observed in the experimental observations in terms of nonlinear behavior, stored elastic energy W_0 and ultimate properties.

Both stiffening and loss of stretchability evolve in a monotonic manner with the nanofiller content increase while the tensile strength reaches a maximum at 0.7 wt% nanofiller concentration. The evolution of the material properties with the nanofiller concentration may be correlated to effective strengthening mechanisms and underlying changes of the hydrogel structural features.

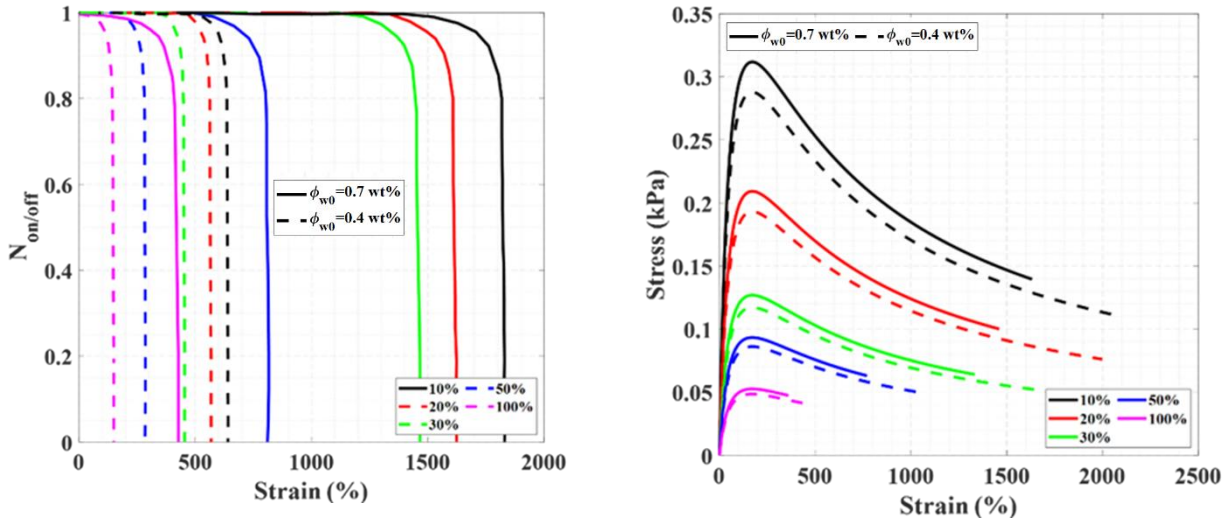

(a) (b)

Figure III.4 Swelling effect on (a) chains network evolution and (a) nanoparticle stress.

The latter intensify with the increase in the total interfacial area when the amount of the dispersed second phase increases. The hydrogel structural changes are clarified by the model results reported in Figures III.3 and III.4. Increasing nanofiller content leads to the mean chain length reduction (Figure III.3a). Indeed, increasing the amount of nanofillers reduces the overall molecular weight in the hydrogel matrix as experimentally evidenced by Shi et al. (2015) for the same material system, in turn reducing the chain flexibility and thus the bonds strength governing the failure stress (Figure III.3b). It is worth noticing that the value found for *N* does not correspond to the expected value of a physically cross-linked system. In spite of its physical meaning, this parameter only leads

to a phenomenological description of the polymer chains behavior (Guo and Zaïri, 2021). The uultrahigh toughness of the nanocomposite compared to its pristine counterpart may be directed related to the reorganization of the chains upon the mechanical history (Figure 4a). Besides, the extremely large surface area of the nanoparticles promotes strong physical contact and strong near-field direct interactions leading to more efficient stress transfer (Figure III.4b). The enhanced toughening effects, with a great mechanical strength improvement but lowest stretchability, as the nanofiller content is increased may be interpreted by the increase in local events of detachment-reattachment mechanism (Figure III.4a). Also, if the reinforcement mechanism is ascribed to strong near-field direct interactions, the nanofillers act also as entanglement attractors in the cross-linked network modifying the topological constrain (Figure III.3b). Indeed, the role of the nanofillers is not limited to their ability to reinforce the hydrogel network, they play an important role in energy dissipation capacity.

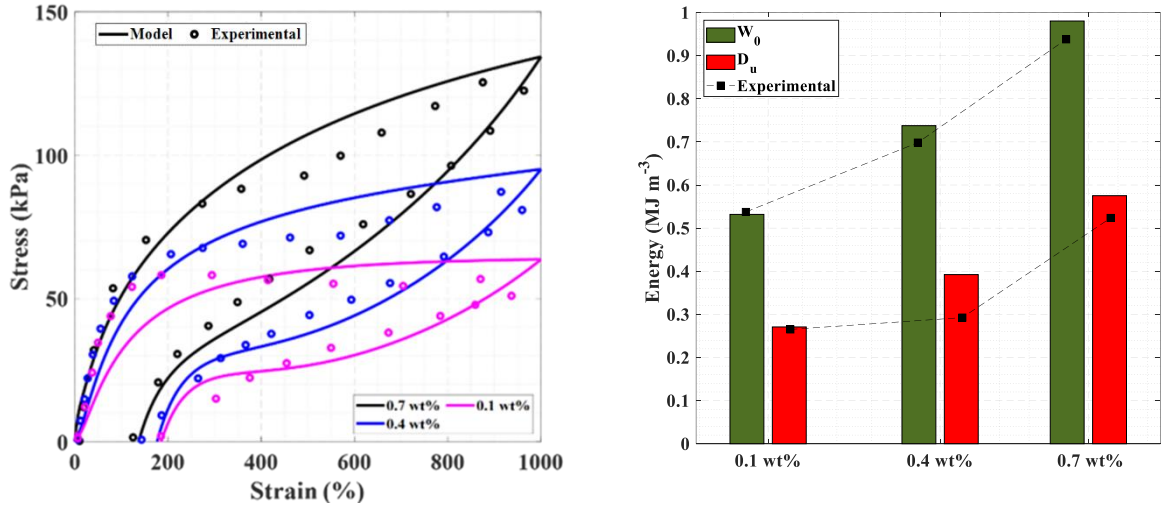

(a) (b)

Figure III.5 Model vs. experimental under a stretching-retraction cycle at the initial swelling state for different nanofiller amounts: (a) stress-strain response and (b) dissipated energy.

Figure III.5a shows the model ability to predict the nonlinear mechanical response under a stretching-retraction cycle with a maximum strain of 1000%. Both the pronounced stress-strain hysteresis and the residual strain at zero-stress are adequately captured by the model for the different nanofiller amounts.

	Failure strain (%)		Failure stress (kPa)		Energy (MJ m^{-3})	
Nanoparticle weight fraction (wt%)	Experimental	Model (Errors)	Experimental	Model (Errors)	Experimental	Model (Errors)
0.05	3024	3028 (0.12%)	121	120 (0.85%)	2.15	2.20 (2.25%)
0.1	2857	2848 (0.29%)	151	149 (1.16%)	2.34	2.44 (4.33%)
0.4	2454	2436 (0.71%)	228	224 (1.77%)	2.76	2.92 (5.95%)
0.1	2160	2172 (0.54%)	372	374 (0.50%)	3.47	3.46 (0.39%)
1.0	2065	2024 (1.99%)	313	304 (2.76%)	3.41	3.33 (2.15%)
1.5	1674	1724 (2.98%)	275	259 (5.80%)	2.35	2.60 (10.32%)

Table III.3 Experimental data and model outputs under a monotonic stretching at the initial swelling state for different nanofiller amounts.

Both stored elastic energy W_0 and dissipated energy D_u are plotted in Figure III.5b. The latter is calculated as $D_u = W_0 - W_u$ in which W_u is the released energy, i.e. area under the unloading segment. The experimental energy data along with the associated outputs of the model are also reported in Table III.4. It can be noticed that the model is favorably compared to the large amount of energy dissipated during the loading process and its variation with the nanofiller amount.

III.3.2 Swelling effect Multiaxial energy dissipation

The predictive capacities of the model regarding the swelling effect is now examined[4]. Figure III.6 and Table III.5 present the model predictions for a 0.7 wt% filler concentration at different swelling ratios. The stress is computed till failure; it is defined as the local maximum stress level reached as indicated by the cross.

[4] The weight swelling ratio ϕ_{sw} is defined as the fractional increase in the hydrogel weight due to solvent absorption: $\phi_{sw} = (m - m_0)/m_0$ where m_0 and m are the weights at the initial swelling state and at the swollen state, respectively. The weight swelling ratio ϕ_{sw} is used as a direct model input by using the following relationship with the volume change: $J = 1 + \left(1 + \phi_{sw}^{-1} \rho_m / \rho_{solvent}\right)^{-1}$ where ρ_m = 1.4 g/cm^3 is the poly(acrylic acid) hydrogel matrix density (Lira et al., 2009) and $\rho_{solvent}$ = 1.0 g/cm^3 is the solvent density.

	W_0 (MJ m^{-3})		D_u (MJ m^{-3})	
Nanoparticle weight fraction (wt%)	Experimental	Model (Errors)	Experimental	Model (Errors)
0.1	0.54	0.53 (1.06%)	0.27	0.27 (2.15%)
0.4	0.70	0.73 (5.62%)	0.29	0.39 (34.09%)
0.7	0.94	0.98 (4.53%)	0.52	0.57 (9.85%)

Table III.4 Experimental data and model outputs under a stretching-retraction cycle at the initial swelling state for different nanofiller amounts.

	Failure strain (%)		Failure stress (kPa)		Energy (MJ m^{-3})	
Swelling ratios	Experimental	Model (Errors)	Experimental	Model (Errors)	Experimental	Model (Errors)
10	1733.7	1807 (4.22%)	61.32	65.56 (%)	0.45	0.49 (8.4%)
20	1547.3	1600 (3.40%)	40.12	43.36 (%)	0.28	0.30 (7.96%)
30	1413.5	1443 (2.08%)	18.34	29 (%)	0.14	0.14 (1.48%)
50	778.7	794 (1.69%)	7.65	10.75 (%)	0.03	0.02 (17.70%)
100	351.9	343 (2.52%)	3.29	3.57 (%)	0.01	0.01 (11.39%)

Table III.5 Experimental data and model outputs under a monotonic stretching at different swelling ratios for a 0.7 wt% nanofiller amount.

The model predicts perfectly the serious reduction of the stiffness with the swelling ratio increase. This is a direct consequence of the chain density reduction with increasing water content. The model adequately captures the effective energy dissipation exhibited at low swelling ratio and its significant reduction with increasing water content.

	W_0 (MJ m^{-3})		D_u (MJ m^{-3})	
Swelling ratios	Experimental	Model (Errors)	Experimental	Model (Errors)
	Original/1h recovery	Original/1h recovery	Original/1h recovery	Original/1h recovery
0	9.26/5.87	9.87 (6.65%)/6.20 (5.57%)	3.13/2.49	3.36 (7.07%)/3.04 (22.02%)
10	-	2.45/1.96	-	1.91/1.56
20	-	2.01/1.50	-	1.44/1.08
30	-	1.20/0.83	-	0.91/0.63
50	-	0.26/0.16	-	0.12/0.08
100	-	0.07/0.05	-	0.02/0.02

Table III.6 Experimental data and model outputs under a stretching-retraction cycle for a 0.7 wt% nanofiller amount.

The swelling-induced loss of energy dissipation capacity is attributable to the change in the limiting chain extensibility and the bonds strength (see Figure III.1b). The dramatic degradation of both stretchability and tensile strength with increasing water content is also well captured by the model. This negative effect on the tensile properties may be attributed to the swelling-induced network deformation and restriction of the chain motions, the breaking rate of bonds being strongly sensitive to the swelling as illustrated in (Figure III.4a).

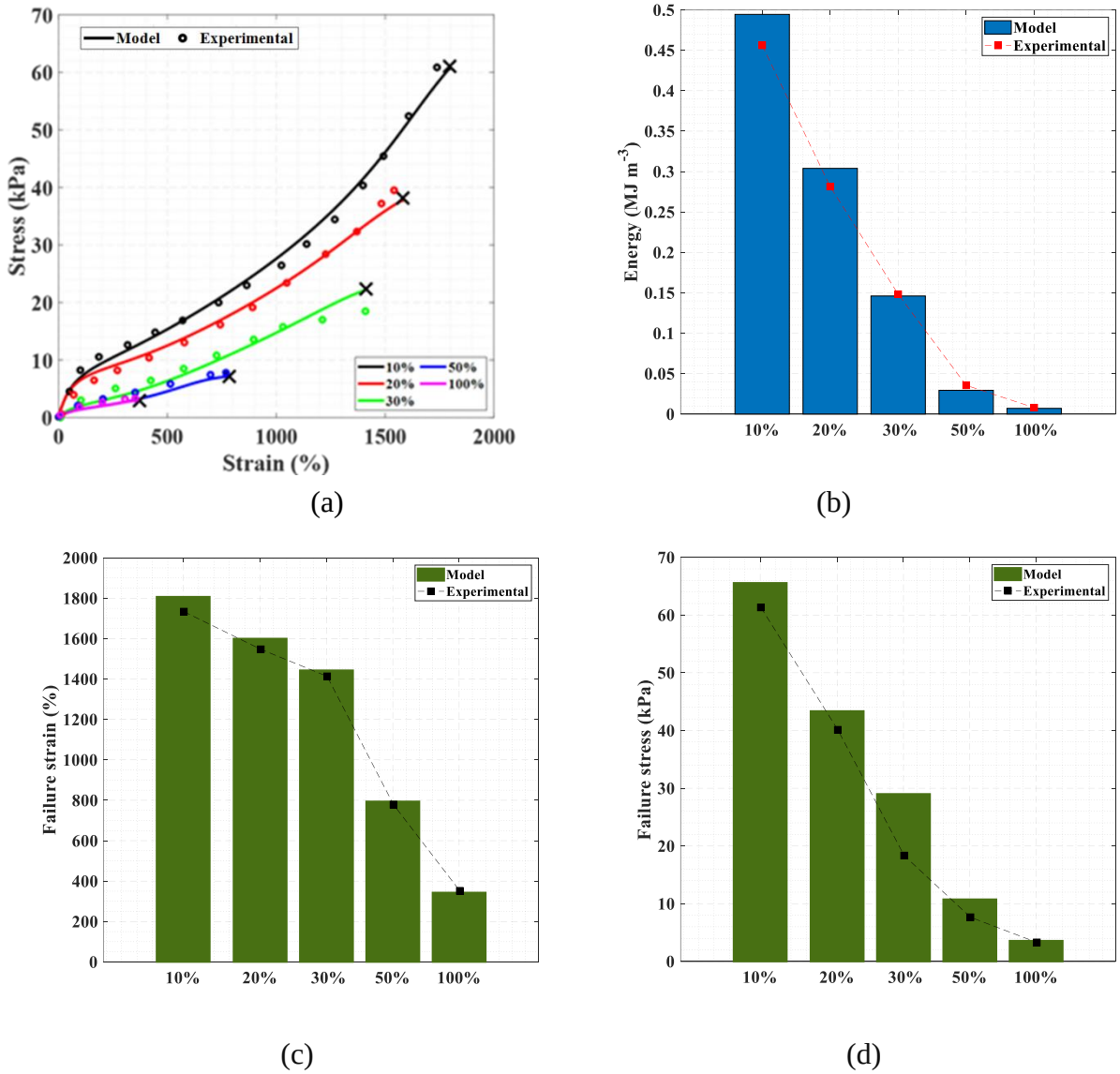

(a) (b)

(c) (d)

Figure III.6 Model vs. experimental under monotonic stretching at different swelling ratios for a 0.7 wt% nanofiller amount: (a) stress-strain response, (b) toughness, (c) failure strain and (d) failure stress.

Besides, the near-field direct interactions between nanoparticles and the swollen hydrogel matrix is strongly affected by the swelling state; More the amount of water, less efficient stress transfer as evidenced by the local stress in the nanoparticles plotted in (Figure III.4b).This negative effect on the tensile properties may be attributed to the swelling-induced network deformation and restriction of the chain motions, the breaking rate of bonds being strongly sensitive to the swelling as illustrated in (Figure III.4a). Besides, the near-field direct interactions between nanoparticles and the swollen hydrogel matrix is strongly affected by the swelling state; More the amount of water, less efficient stress transfer as evidenced by the local stress in the nanoparticles plotted in Figure (III.4b). The damage self-healing behavior is presented in (Figure III.7) for a 0.7 wt% filler concentration at the initial swelling state. (Figure III.7a) shows that the model matches very well with the stretching-retraction data both for the original response and after 1 hour of recovery. The large hysteresis observed for the first stretching-retraction cycle is gradually recovered to the original pathway after a reloading with increase in recovery time. In the insert of (Figure III.7b), it can be also observed a good agreement between the computed energy and the experimental data.

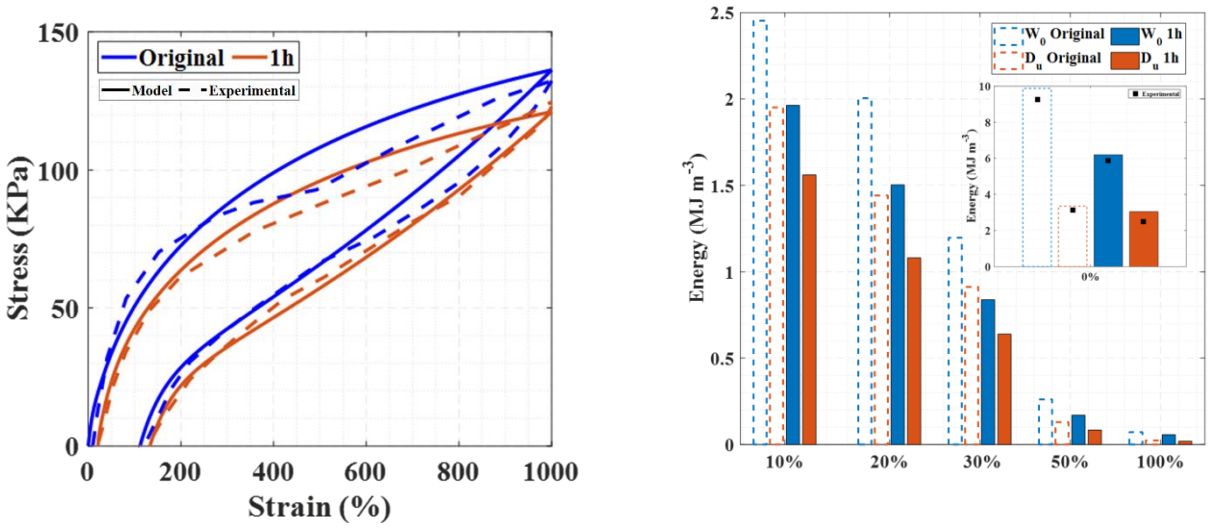

(a) (b)

Figure III.7 Model vs. experimental under a stretching-retraction cycle for a 0.7 wt% nanofiller amount and 1h recovery: (a) stress-strain response at the initial swelling state and (b) dissipated energy at different swelling ratios.

The other model predictions plotted in (Figure III.7b) and (Table III.6) point out the swelling effect on the self-healing in energy dissipation capacity. The latter is obviously affected by the stretch rate as observed in the illustrative examples provided in (Figure III.8) in which the stretching-retraction behavior is presented for one order of magnitude higher and one order of magnitude smaller than the stretch rate used in (Figure III.7a) The figure points out in particular the rate-dependency of the hysteresis loop both for the original response and after 1 hour of recovery. The higher the stretch rate, the higher the hysteresis loop area.

The self-healing evolution with the recovery time is now presented in (Figures III.9 and III.10) in terms of the strain recovery factor $R=\left(1-\varepsilon/\varepsilon_{\max}\right)\times 100$ in which $\varepsilon_{\max}$ is the maximum nominal strain and ε is the strain recovered with the time. The figures present computed results at the initial swelling state and at a swelling ratio of 50% for a 0.7 wt% filler concentration and the neat

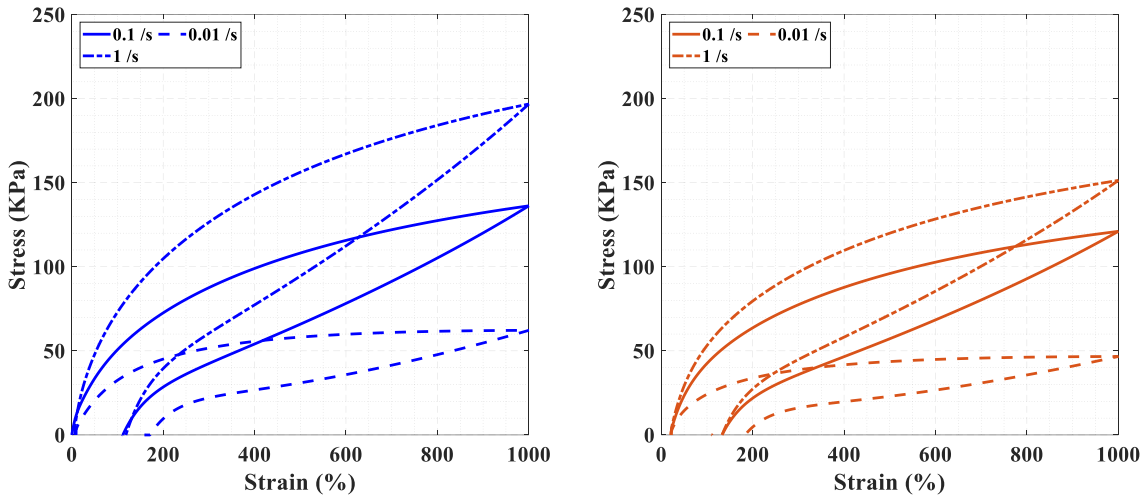

(a) (b)

Figure III.8 Model results of the stretching-retraction behavior at different stretch rates for a 0.7 wt% nanofiller amount: (a) original and (b) after 1h recovery.

hydrogel. The recovery response is characterized by an initial rapid transient followed by the trend to reach an equilibrium at the end of the zero-stress creep response. The model shows that the self-healing capacities are highly facilitated by the adding of nanoparticles. Nonetheless, the destroyed

bonds in the swollen nanocomposite cannot fully recombine; the recovery efficiency depends on the swelling state. The higher the water content, the slower the recombination mechanism and the smaller the recovery extent.

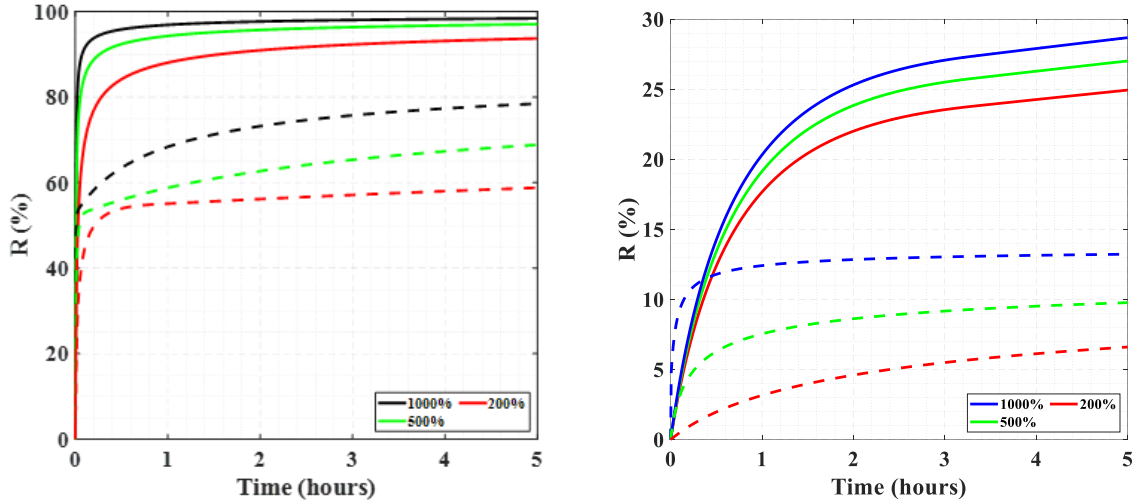

Figure III.9 Model results of the recovery behavior for previous stretching-retraction at different maximum strain levels: (a) 0.7 wt% nanofiller amount and (b) neat hydrogel (solid lines: initial swelling state, dashed lines: swelling ratio of 50%).

The degree to which the strain is recovered is found actually highly dependent on coupled effects of swelling state, microstructure and previous mechanical history in terms of applied strain level and strain rate. The higher the strain level, the higher the recovery extent (Figure III.9). It is also found that the incomplete strain recovery increases with the increase in strain rate (Figure III.10). The same tendency is observed for the initial swelling state and for the 50% swelling ratio.

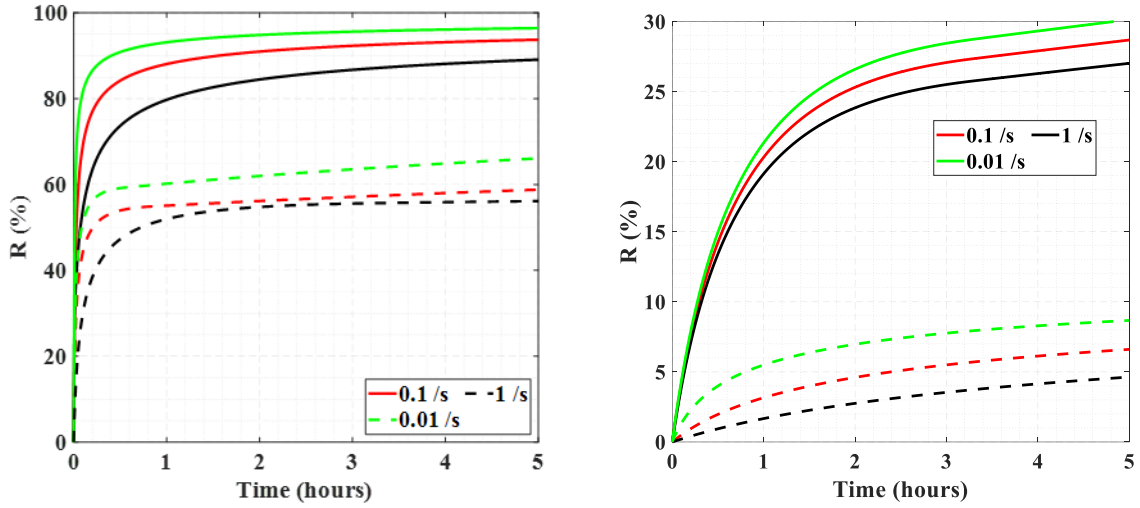

Figure III.10 Model results of the recovery behavior for previous stretching-retraction at different stretch rates (and a maximum strain level of 200%): (a) 0.7 wt% nanofiller amount and (b) neat hydrogel (solid lines: initial swelling state, dashed lines: swelling ratio of 50%).

III.4 Partial conclusion

In this chapter, a micromechanical model was proposed to quantitatively predict the visco-super-elastic behavior of swollen hydrogel-based nanocomposites. The model is formulated using the Eshelby equivalent inclusion method within a finite strain context. The application was performed on a high-swelling capacity hydrogel filled with different concentrations of nanoparticles. The quantitative comparisons show the relevance of the model to describe the swelling effect on the stretchability, the mechanical strength, the energy dissipation and the self-healing while accounting for the mechanisms of nanofillers reinforcement.

The model provides direct evidence of the variation of both structural evolution and reinforcement in response to a swelling variation, which is useful in the design and optimization of swollen hydrogel-based nanocomposites. In the future developments, the detachment-reattachment mechanism will be described by an expression based on a thermodynamic reasoning (Guo and Zaïri, 2021) while taking into account the chemical loading of the external fluid. More complex mechanical loading conditions remains also an important issue for further investigations of the swelling-microstructure-mechanics relationship.

References

Bergstrom, J.S., Boyce, M.C., 1998. Constitutive modeling of the large strain time-dependent behavior of elastomers. Journal of the Mechanics and Physics of Solids 46, 931-954.

Boyce, M. C., Arruda, E.M., 2001. Swelling and mechanical stretching of elastomeric materials. Mathematics and Mechanics of Solids 6, 641-659.

Chen, H., Liu, Y., Ren, B., Zhang, Y., Ma, J., Xu, L., Chen, Q., Zheng, J., 2017. Super bulk and interfacial toughness of physically crosslinked double-network hydrogels. Advanced Functional Materials 27, 1703086.

Chester, S.A., Anand, L., 2010. A coupled theory of fluid permeation and large deformations for elastomeric materials. Journal of the Mechanics and Physics of Solids 58, 1879-1906.

Chester, S.A., Anand, L., 2011. A thermo-mechanically coupled theory for fluid permeation in elastomeric materials: Application to thermally responsive gels. Journal of the Mechanics and Physics of Solids 59, 1978-2006.

Deng, H., Pence, T.J., 2010. Shear induced loss of saturation in a fluid infused swollen hyperelastic cylinder. International Journal of Engineering Science 48, 624-646.

Deng, H., Pence, T.J., 2010. Equilibrium states of mechanically loaded saturated and unsaturated polymer gels. Journal of Elasticity 99, 39-73.

Dolbow, J., Fried, E., Ji, H., 2004. Chemically induced swelling of hydrogels. Journal of the Mechanics and Physics of Solids 52, 51-84.

Drozdov, A.D., Christiansen, J.D., 2013. Constitutive equations in finite elasticity of swollen elastomers. International Journal of Solids and Structures 50, 1494-1504.

Duda, F.P., Souza, A.C., Fried, E., 2010. A theory for species migration in a finitely strained solid with application to polymer network swelling. Journal of the Mechanics and Physics of Solids 58, 515-529.

Flory, P.J., 1942. Thermodynamics of high polymer solutions. The Journal of Chemical Physics 10, 51-61.

Guo, J., Luo, J., Xiao, Z., 2016. On the opening profile and near tip fields of an interface crack between a polymeric hydrogel and a rigid substrate. Engineering Fracture Mechanics 153, 91-102.

Guo, Q., Zaïri, F., Guo, X., 2018. A thermo-viscoelastic-damage constitutive model for cyclically loaded rubbers. Part II: Experimental studies and parameter identification. International Journal of Plasticity 101, 58-73.

Guo, Q., Zaïri, F., 2021. A micromechanics-based model for deformation-induced damage and failure in elastomeric media. International Journal of Plasticity 140, 102976.

Gurtin, M.E., Anand, L., 2005. The decomposition F=FeFp, material symmetry, and plastic irrotationality for solids that are isotropic-viscoplastic or amorphous. International Journal of Plasticity 21, 1686-1719.

Hong, W., Zhao, X., Zhou, J., Suo, Z., 2008. A theory of coupled diffusion and large deformation in polymeric gels. Journal of the Mechanics and Physics of Solids 56, 1779-1793.

Huggins, M.L., 1941. Solutions of long chain compounds. The Journal of Chemical Physics 9, 440-440.

Konda, A., Urayama, K., Takigawa, T., 2011. Strain-rate-dependent Poisson's ratio and stress of polymer gels in solvents revealed by ultraslow stretching. Macromolecules 44, 3000-3006.

Lai, Y., Hu, Y., 2017. Unified solution for poroelastic oscillation indentation on gels for spherical, conical and cylindrical indenters. Soft Matter 13, 852-861.
Li, J., Suo, Z., Vlassak, J.J., 2014. A model of ideal elastomeric gels for polyelectrolyte gels. Soft Matter 10, 2582-2590.
Lira, L.M., Martins, K.A., de Torresi, S.I.C., 2009. Structural parameters of polyacrylamide hydrogels obtained by the equilibrium swelling theory. European Polymer Journal 45, 1232-1238.
Liu, H., Peng, H., Xin, Y., Zhang, J., 2019. Metal-organic frameworks: a universal strategy towards super-elastic hydrogels. Polymer Chemistry 10, 2263-2272.
Lou, Y., Robisson, A., Cai, S., Suo, Z., 2012. Swellable elastomers under constraint. Journal of Applied Physics 112, 034906.
Okumura, D., Kondo, A., Ohno, N., 2016. Using two scaling exponents to describe the mechanical properties of swollen elastomers. Journal of the Mechanics and Physics of Solids 90, 61-76.
Okumura, D., Mizutani, M., Tanaka, H., Uchida, M., 2018. Effects of two scaling exponents on biaxial deformation and mass transport of swollen elastomers. International Journal of Mechanical Sciences 146, 507-516.
Okumura, D., Chester, S. A., 2018. Ultimate swelling described by limiting chain extensibility of swollen elastomers. International Journal of Mechanical Sciences 144, 531-539.
Ovalle-Rodas, C., Zaïri, F., Naït-Abdelaziz, M., Charrier, P., 2015. Temperature and filler effects on the relaxed response of filled rubbers: experimental observations on a carbon-filled SBR and constitutive modeling. International Journal of Solids and Structures 58, 309-321.
Saadedine, M., Zaïri, F., Ouali, N., Tamoud, A., Mesbah, A., 2021. A micromechanics-based model for visco-super-elastic hydrogel-based nanocomposites. International Journal of Plasticity 144, 103042.
Sakamoto, S., Fujino, K., Shimojima, A., Kuroda, K., 2018. Formation of silica-organic hybrid nanoparticles by cross-linking of ultra-small silica nanoparticles. Chemistry Letters 47, 1018-1021.
Shi, F.K., Wang, X.P., Guo, R.H., Zhong, M., Xie, X.M., 2015. Highly stretchable and super tough nanocomposite physical hydrogels facilitated by the coupling of intermolecular hydrogen bonds and analogous chemical crosslinking of nanoparticles. Journal of Materials Chemistry B 3, 1187-1192.
Sun, J.Y., Zhao, X., Illeperuma, W.R.K., Chaudhuri, O., Oh, K.H., Mooney, D.J., Vlassak, J.J., Suo, Z., 2012. Highly stretchable and tough hydrogels. Nature 489, 133-136.
Urayama, K., Taoka, Y., Nakamura, K., Takigawa, T., 2008. Markedly compressible behaviors of gellan hydrogels in a constrained geometry at ultraslow strain rates. Polymer 49, 3295-3300.
Urayama, K., Takigawa, T., 2012. Volume of polymer gels coupled to deformation. Soft Matter 8, 8017-8029.
Wang, D., Wu, M.S., 2013. Analytical solutions for bilayered spherical hydrogel subjected to constant dilatation. Mechanics of Materials 58, 12-22.
Wang, Q., Gao, Z., 2016. A constitutive model of nanocomposite hydrogels with nanoparticle crosslinkers. Journal of the Mechanics and Physics of Solids 94, 127-147.
Wang, Q., Gao, Z., Yu, K., 2017. Interfacial self-healing of nanocomposite hydrogels: Theory and experiment. Journal of the Mechanics and Physics of Solids 109, 288-306.
Wineman, A., Rajagopal, K.R., 1992. Shear induced redistribution of fluid within a uniformly swollen nonlinear elastic cylinder. International Journal of Engineering Science 30, 1583-1595.
Yin, H.M., Sun, L.Z., Chen, J.S., 2002. Micromechanics-based hyperelastic constitutive modeling of magnetostrictive particle-filled elastomers. Mechanics of Materials 34, 505-516.

Zaïri, F., Naït-Abdelaziz, M., Woznica, K., Gloaguen, J.M., 2007. Elasto-viscoplastic constitutive equations for the description of glassy polymers behavior at constant strain rate. Journal of Engineering Materials and Technology 129, 29-35.

Zhao, X., Huebsch, N., Mooney, D.J., Suo, Z., 2010. Stress-relaxation behavior in gels with ionic and covalent crosslinks. Journal of Applied Physics 107, 063509.

Zhong, M., Shi, F.K., Liu, Y.T., Liu, X.Y., Xie, X.M., 2016. Tough superabsorbent poly (acrylic acid) nanocomposite physical hydrogels fabricated by a dually cross-linked single network strategy. Chinese Chemical Letters 27, 312-316.

Chapter IV

A multiscale model for multiaxial inelastic behavior of elastomeric particulate composites

CHAPTER IV

A multiscale model for multiaxial inelastic behavior of elastomeric particulate composites[5]

This chapter addresses the problem of the multiscale constitutive representation of the multiaxial inelastic behavior of elastomeric particulate composites. A fully three-dimensional model is proposed within a micromechanical treatment to describe the multiaxial inelastic response in relation to the reinforcement mechanisms. A network decomposition based on the tube confinement theory is used to consider the combined effects of multiaxiality and inelasticity. The near-field direct interactions between the particles and the rubber networks are physically described using the Eshelby inclusion theory. The capabilities of the microstructure-based model are evaluated for different modes of deformation over a wide range of filler concentrations. It is found being able to successfully reproduce the significant features of the multiaxial macro-response upon monotonic and cyclic loading sequences. Important insights about the effective role of the reinforcement mechanisms on the multiaxial dissipation are revealed.

Keywords: *Elastomeric particulate composites; Reinforcement mechanisms; Multiaxial deformation, Multiaxial failure; Multiaxial dissipation.*

[5] This chapter is based on the following paper: Saadedine, M., Zaïri, F., Ouali, N., Mai, T., Urayama, K., Tamoud, A., Mesbah, A., 2022. A micromechanics-based model for visco-super-elastic hydrogel-based nanocomposites. International Journal of Plasticity. (Under Review)

IV.1 Partial introduction

A reliable design of elastomeric parts requires to consider the multiaxial mechanical history that they could undergo. In this regard, the formulation of continuum-based constitutive models with multiaxial abilities to capture and predict the mechanical response in connection to the microstructure is of prime importance. By allowing a physically-consistent representation, the widely used eight-chain model proposed by Arruda and Boyce (1993) offers a flexible and simple three-dimensional analytical formulation. It takes into account the entropy of a simple network of eight long-chain molecules by introducing the Langevin chain statistics and degenerates to the more classical Neo-Hookean model for extremely long-chain molecules. Although it is widely used to design elastomeric parts, eight-chain model fails to capture the biaxial mechanics. Actually, most of existing models may capture the behavior in one loading mode such as the uniaxial extension to good accuracy and fail to predict the behavior in the other loading modes.

Over the years, several authors proposed enhancements of the eight-chain model by more or less deep empirical or physical corrections (Boyce and Arruda, 2000; Meissner and Matejka, 2003, 2004; Miroshnychenko and Green, 2009; Bechir et al., 2010; Kroon, 2011; Dal et al., 2020; Anssari-Benam and Bucchi, 2021). These models were proposed to increase the biaxial performance of the eight-chain model. Comparative studies of the different modified versions of the eight-chain model can be found in the literature (Boyce and Arruda., 2000; Hossain et al., 2015; He et al., 2021; Melly et al., 2021). Being based on an affine description, the eight-chain model ignores the interactions between polymer chains. Some well-known modified versions of the eight-chain model were proposed to consider the chains interactions through the adding of the topological constraint effects obtained from the micromechanics of the chain molecules. Boyce and Arruda (2000) proposed a modified version of their original model based on a network decomposition by combining a phantom part due to the presence of neighboring chains, and represented by the eight-

chain energy function, with a Flory and Erman (1982) topological constraint contribution[6], the two networks being thus considered in which the chain crosslinking points are constrained from the eight-chain network with phantom characteristics via interactions with other chains. Wu and van der Giessen (1992) combined the three-chain model (James and Guth, 1943) and the eight-chain model by a phenomenological adjustment parameter. In the Wu and van der Giessen (1992) model, when the deformation is applied, the two superimposed networks deform affinely. Later, Bechir et al. (2010) proposed a similar phenomenological eight-chain/three-chain combination considering topological constraints to account for the non-affine deformation with four supplementary model parameters. Meissner and Matejka (2003, 2004) added an entanglement term of the extended tube model to the eight-chain model. In the abovementioned models, the eight-chain energy function remains solely dependent on the first strain invariant I_1 which explains in great part the difficulty to predict or even to simply capture the multiaxial mechanical response. Other extensions of the eight-chain model were proposed to improve its multiaxial abilities by the incorporation of the second strain invariant I_2. This strain invariant has indeed a greater importance in the multiaxial deformation than in the uniaxial deformation (Horgan and Saccomandi, 1999; Wineman, 2005; Horgan and Smayda, 2012; Puglisi and Saccomandi., 2016; Destrade et al., 2017). In the latter aforementioned studies, specific examples can be found in torsional and simple shear deformations. In a more general specification, all generalized neo-Hookean functions are unable to capture full deformation modes if the second strain invariant is not incorporated whatever the mathematical expression. Kroon (2011) improved the eight-chain model by introducing a I_2-dependence using the tube model along with topological constraints to consider the non-affine deformation of a polymer chain; the resulting model contains three supplementary model parameters. Recently, Dal

[6] This approach is consistent with the tube-constraints earlier introduced by Doi and Edwards (1988) and extended latter by several authors (Edwards and Vilgis, 1988; Heinrich et al., 1988; Heinrich and Kaliske, 1997; Khiêm and Itskov, 2016) in which a chain is confined by neighboring chains within a tube-like region. Similarities of the physics can be noticed between the Flory-Erman (1982) and the Doi-Edwards (1988) approaches despite the different departure points in the treatment of topological constraints.

et al. (2020) proposed a similar I_2-based extension of the eight-chain model resulting in three supplementary model parameters. Anssari-Benam and Bucchi (2021) proposed an extended eight-chain model introducing both the tube-constraints and the second strain invariant; the resulting model contains two model parameters. These studies provide improved fits to the experimental data compared with the original model particularly for biaxial and pure shear deformations. The incorporation of the second strain invariant into strain energy function appears as a necessary condition to capture the multiaxial behavior and to further improve model prediction abilities (Anssari-Benam et al., 2021). Besides, the nanoparticles are widely employed to reinforce the elastomers. Nonetheless, none of these extensions of the eight-chain model introduces the effective contribution of fillers while the model abilities are verified most of the time by comparisons to particle filled elastomeric experimental data. Moreover, these material media exhibit inelastic features such as Mullins effect and hysteresis upon stretching-retraction. Considerable efforts have been made to the constitutive modeling of the inelastic features of rubber-like materials (Ayoub et al., 2014; Dargazany et al., 2014; Khiêm and Itskov, 2016; Guo et al., 2018; Su and Peng, 2018; Zhou et al., 2018; Mahjoubi et al., 2019; Morovati and Dargazany, 2019; Mohammadi and Dargazany, 2019; Xiang et al., 2019; Chaabane et al., 2021; Morovati et al., 2021; Xiao et al., 2021; Guo and Zaïri, 2020, 2021; Liu et al., 2022). In the most physically-based constitutive models, the description of the inelasticity in neat rubber is provided by means of the tube-constraints of Doi and Edwards (1988) describing conceptually the interaction of an individual chain with its neighbourhoods via its reptational Brownian motion along the centerline of a tube-like region. Besides, the energy dissipation in filled rubbers is mainly governed by the interfacial friction between the fillers and the rubber matrix, e.g. slippage of chains along the filler surface and adsorption-desorption mechanism of chains on the filler surface. Due to an increase in the total interfacial area between filler and rubber matrix, a deep influence of the filler concentration on the

energy dissipation was reported (Guo et al., 2017) with a strong influence in loading multiaxiality (Mai et al., 2017).

Comprehensive understanding of the coupled effects between multiaxiality and inelasticity in connection to the reinforcement mechanisms is important but a constitutive representation connecting them has not been treated in the literature yet. In order to resolve this issue, in this contribution, we formulate, identify and verify a micromechanics-based extension of the eight-chain model. In our previous work (Saadedine et al., 2021), we formulated a micromechanics-based model relating the internal network structure of reinforced soft rubber-like materials to their large nonlinear response while considering the effective interactions with the inorganic nanoparticles. The latter were integrated by means of the Eshelby equivalent inclusion method within a finite strain context and the eight-chain cube context. Only monotonic stretching till failure had been used to verify the model abilities. The main objective of this paper is thus to further extend the model to provide him multiaxial abilities. A two-scale strategy is used to formulate the multiaxial and multiscale model. Firstly, the transition from the particles scale to the macroscale is described within the Eshelby inclusion theory. Secondly, the micromechanics of the chains is described using the tube-constraints and the second strain invariant to account for the combined effects of multiaxiality and inelasticity in the finite-strain behavior. The fully three-dimensional microstructure-based constitutive model is used to represent the multiaxial macro-response of elastomeric particulate composites upon monotonic and cyclic loading sequences. The developed approach is employed to better understand the mechanisms of mechanical property enhancement by providing important insights about the relation between microstructure and multiaxial dissipation.

This chapter is organized as follows. Section IV.2 provides the main elements of the multiscale model formulated within the continuum-based micromechanical framework.Section IV.3 presents and discusses the multiaxial capacities of the model. Section IV.4 closes the paper with some concluding remarks.

The following notation is used throughout the text. Tensors and vectors are denoted by normal boldfaced letters and italicized boldfaced letters, respectively, while scalars and individual components of vectors and tensors are denoted by normal italicized letters. The superposed dot designates the time derivative. The superscript *T* indicates the transpose quantity.

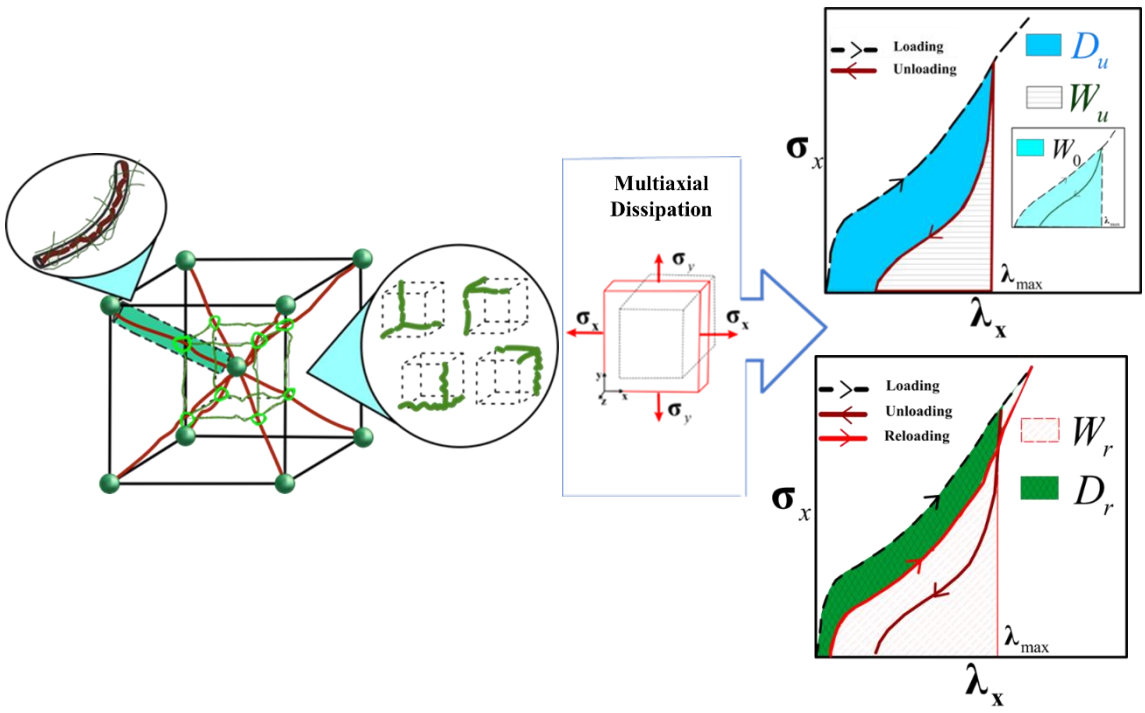

Figure IV.1 Nine-particle cubic cell with tube-constrained eight-chain and three-chain networks and energy balance upon loading-unloading and loading-unloading-reloading sequences.

IV.2 Model formulation

Figure IV.1 presents a schematic view of the model based on the idealized eight-chain cubic cell. The ideal representation of the polymer network has undergone in our approach some adjustments to introduce the combined effects of multiaxiality and inelasticity using a network decomposition. The topological constraints of the polymer chains are introduced using the tube model in which the motion of a single chain of the eight-chain cubic cell is constrained in a tube-like region due to the neighboring chains. In the main cubic cell is inscribed another cubic cell constituted by four three-

chain units located in the center and distributed upon the three principal axes. The introduction of the four three-chain units into the eight-chain cubic cell was earlier proposed by Bechir et al. (2010). The main cubic cell is used for the non-entangled links while the inscribed three-chain units play the role of a superimposed constraint network to represent the entanglements. Both links may change with the mechanical loading depending on the deformation mode and the deformation level applied to the cell. The particles are then explicitly considered in the model thanks to the micro-macro scale transition within the Eshelby inclusion theory as already presented in our previous work (Saadedine et al., 2021). The Eshelbian homogenization provides the approximate solution of the near-field direct interactions between matrix and particles. Eight particles are inserted at the vertices of the cubic cell and are connected to a central particle via the eight chains as illustrated in Figure IV.1.

IV.2.1 Kinematics based on micro-macro scale transition

This subsection provides the finite-strain kinematics within the framework of continuum mechanics. A simple topological-based analysis of the cubic cell leads to the following expression of the deformation gradient of the composite $\bar{\mathbf{F}}$ (Saadedine et al., 2021):

$$\bar{\mathbf{F}} = (1-2\rho)\mathbf{F}_m + 2\rho\mathbf{F}_p \tag{IV.1}$$

where $\mathbf{F}_m$ and $\mathbf{F}_p$ are the deformation gradients of the rubber matrix and the particles, respectively. The term $\rho = r/b$ is defined as the ratio between the particle radius r and the center-to-center distance b between the central particle and a neighboring particle. The Jacobian of the deformation gradient $\bar{\mathbf{F}}$ is $\bar{J} = \det(\bar{\mathbf{F}}) > 0$ and its time derivative is $\dot{\bar{\mathbf{F}}} = \bar{\mathbf{L}}\bar{\mathbf{F}}$ in which $\bar{\mathbf{L}}$ is the spatial velocity gradient. The different couplings are inserted using the multiplicative decomposition notion of the deformation based on the conceptual sequence of configurations. By introducing an intermediate virtual configuration, $\bar{\mathbf{F}} = \bar{\mathbf{F}}_{\text{iso}}.\bar{\mathbf{F}}_{\text{vol}}$ is multiplicatively split into an isochoric part $\bar{\mathbf{F}}_{\text{iso}}$ and a

volumetric part $\bar{\mathbf{F}}_{\text{vol}}$. The Jacobian of the isochoric part is equal to unity and the volumetric deformation gradient is expressed as $\bar{\mathbf{F}}_{\text{vol}} = \bar{J}^{1/3}\mathbf{I}$, $\mathbf{I}$ being the unit tensor.

The intrinsic viscosity of the composite emanates from the rubber matrix. By considering an intermediate relaxed configuration during a spontaneous virtual elastic unloading, the isochoric deformation gradient of the rubber matrix $\mathbf{F}_{m\_\text{iso}}$ may be multiplicatively split into an elastic part $\mathbf{F}^{e}_{m\_\text{iso}}$ and a viscous part $\mathbf{F}^{v}_{m\_\text{iso}}$ as $\mathbf{F}_{m\_\text{iso}} = \mathbf{F}^{e}_{m\_\text{iso}}.\mathbf{F}^{v}_{m\_\text{iso}}$. The corresponding isochoric spatial velocity gradient $\mathbf{L}_{m\_\text{iso}} = \dot{\mathbf{F}}_{m\_\text{iso}}\mathbf{F}^{-1}_{m\_\text{iso}}$ is described by:

$$\mathbf{L}_{m\_\text{iso}} = \dot{\mathbf{F}}^{e}_{m\_\text{iso}}\mathbf{F}^{e^{-1}}_{m\_\text{iso}} + \mathbf{F}^{e}_{m\_\text{iso}}\dot{\mathbf{F}}^{v}_{m\_\text{iso}}\mathbf{F}^{v^{-1}}_{m\_\text{iso}}\mathbf{F}^{e^{-1}}_{m\_\text{iso}} = \mathbf{L}^{e}_{m\_\text{iso}} + \mathbf{L}^{v}_{m\_\text{iso}} \tag{IV.2}$$

The viscous part $\mathbf{L}^{v}_{m\_\text{iso}} = \mathbf{F}^{e}_{m\_\text{iso}}\dot{\mathbf{F}}^{v}_{m\_\text{iso}}\mathbf{F}^{v^{-1}}_{m\_\text{iso}}\mathbf{F}^{e^{-1}}_{m\_\text{iso}}$ is the sum of the viscous stretching rate tensor $\mathbf{D}^{v}_{m\_\text{iso}} = \left(\mathbf{L}^{v}_{m\_\text{iso}} + \mathbf{L}^{v^{T}}_{m\_\text{iso}}\right)/2$ and the viscous spin tensor $\mathbf{W}^{v}_{m\_\text{iso}} = \left(\mathbf{L}^{v}_{m\_\text{iso}} - \mathbf{L}^{v^{T}}_{m\_\text{iso}}\right)/2$: $\mathbf{L}^{v}_{m\_\text{iso}} = \mathbf{D}^{v}_{m\_\text{iso}} + \mathbf{W}^{v}_{m\_\text{iso}}$ and becomes equivalent to the symmetric part $\mathbf{D}^{v}_{m\_\text{iso}}$ while the common assumption of viscous irrotationality $\mathbf{W}^{v}_{m\_\text{iso}} = \mathbf{0}$ is respected (Gurtin and Anand, 2005). The viscous stretching rate $\mathbf{D}^{v}_{m\_\text{iso}}$ is defined by the following general flow rule: $\mathbf{D}^{v}_{m\_\text{iso}} = \dot{\gamma}^{v}_{m}\mathbf{N}$ in which $\dot{\gamma}_{\text{v}}$ is the accumulated viscous strain rate and $\mathbf{N} = \boldsymbol{\sigma}_{m\_\text{iso}}/\|\boldsymbol{\sigma}_{m}\|$ is the direction tensor of viscous flow aligned with the isochoric Cauchy stress $\boldsymbol{\sigma}_{m\_\text{iso}} = \boldsymbol{\sigma}_{m} - 1/3\,\text{trace}\left(\boldsymbol{\sigma}_{m}\right)\mathbf{I}$ with $\|\boldsymbol{\sigma}_{m}\| = \sqrt{\text{trace}\left(\boldsymbol{\sigma}_{m\_\text{iso}}.\boldsymbol{\sigma}^{T}_{m\_\text{iso}}\right)}$ the effective stress expressed by the Frobenius norm.

The finite-strain kinematics of the particles is obtained using the Eshelbian homogenization. The governing constitutive equations of the equivalent homogeneous medium of the linear elastic two-phase medium, obtained using the Eshelby equivalent inclusion method, may be expressed in the context of hyperelasticity by invoking the Saint Venant-Kirchhoff assumption (Yin et al., 2002). The spatial velocity gradient of the particles $\mathbf{L}_{p} = \dot{\mathbf{F}}_{p}.\mathbf{F}^{-1}_{p}$ is expressed as:

$$\mathbf{L}_{p} = \mathbf{A}.\boldsymbol{\Gamma}.\left(\mathbf{I} - \phi\boldsymbol{\Gamma}\right)^{-1} : \bar{\mathbf{L}} \tag{IV.3}$$

where ϕ is the volume fraction of particles, $\mathbf{A}=\left(\mathbf{K}_p-\mathbf{K}_m\right)^{-1}.\mathbf{K}_m$ is the mismatch tensor with $\mathbf{K}_m$ and $\mathbf{K}_p$ the stiffness tensors of the rubber matrix and the particles, respectively, and $\mathbf{\Gamma}$ is a tensor given by:

$$\Gamma_{ijkl}=\left(\frac{-m}{\left(2w-M\right)\left(2w+3m-M\right)}+\frac{M}{2w\left(2w-M\right)}\delta_{IK}\right)\delta_{ij}\delta_{kl}+\frac{1}{4w}\left(\delta_{ik}\delta_{jl}+\delta_{il}\delta_{jk}\right) \tag{IV.4}$$

in which δ_{ij} is the Kronecker delta and, m, w and M are given by:

$$m=\frac{1}{3}\left(K_{mp}-\mu_{mp}\right)+\frac{5\nu_m-1}{15\left(1-\nu_m\right)}+\frac{M}{5},\ w=\frac{\mu_{mp}}{2}+\frac{4-5\nu_m}{15\left(1-\nu_m\right)}+\frac{M}{5},\ M=\frac{40\left(14\rho^2-5\right)\rho^3}{45\left(1-\nu_m\right)} \tag{IV.5}$$

with $K_{mp}=K_m/\left(K_p-K_m\right)$ and $\mu_{mp}=\mu_m/\left(\mu_p-\mu_m\right)$. The terms K_m and K_p are the bulk moduli, μ_m and μ_p are the shear moduli and ν_m is the Poisson's ratio.

IV.2.2 Constitutive relations

The strain-energy function of the composite $\bar{\psi}$ is given as follows (Saadedine et al., 2021):

$$\bar{\psi}=\left(1-2\rho\right)\psi_m+\phi\psi_p \tag{IV.6}$$

where ψ_m and ψ_p are the strain-energy functions of the rubber matrix and the particles, respectively, from which the local stresses are obtained from the differentiation with respect to respective deformations. In what follows, the constitutive relations for the chains network and the particles are successively provided.

IV.2.2.1 Free energy of the rubber matrix with multiaxial abilities

In virtue of the isochoric-volumetric coupling, the free energy of the rubber matrix $\psi_m=\psi_{m\_\mathrm{vol}}+\psi_{m\_\mathrm{iso}}$ is additively split into a volumetric part ψ_{m_vol} and an isochoric part ψ_{m_iso}.

The volumetric strain-energy function ψ_{m_vol} may be expressed as follows (Holzapfel and Simo, 1996):

$$\psi_{m\_\mathrm{vol}} = \frac{1}{4} K_m \left(\exp\left(2\varepsilon_{m\_\mathrm{vol}}\right) - 1 - 2\varepsilon_{m\_\mathrm{vol}} \right) \tag{IV.7}$$

where $\varepsilon_{m\_\mathrm{vol}} = \ln J_m$ is the Hencky volumetric strain of the rubber matrix.

The isochoric free energy ψ_{m_iso} is given by a combination of the eight-chain and three-chain models as: $\psi_{m\_\mathrm{iso}} = \psi_8 + \psi_3$. The following modified version of the eight-chain strain-energy function ψ_8 is used:

$$\psi_8 = n_8 k_B T N_8 \left[\sqrt{\frac{I_{1m}^e/3}{N_8}} \beta + \ln\left(\frac{\beta}{\sinh \beta} \right) \right] + C N_8 \sqrt{I_{2m}^e/3} \tag{IV.8}$$

in which three material parameters are involved: the number of statistical links in a chain N_8, the chain density n_8 and the constant related to the tube constraint on the chains C. The term k_B is the Boltzmann constant, T is the temperature, $\beta = \mathcal{L}^{-1}\left(\sqrt{I_{1m}^e/3} \Big/ \sqrt{N_8} \right)$ is the inverse Langevin function given by a Padé approximant $\mathcal{L}^{-1}(x) \approx x\left(3 - x^2\right)\Big/\left(1 - x^2\right)$, $I_{1m}^e = \mathrm{trace}\left(\mathbf{C}_{m\_\mathrm{iso}}^e\right)$ is the elastic first invariant and $I_{2m}^e = \left(\mathrm{trace}\left(\mathbf{C}_{m\_\mathrm{iso}}^e\right)^2 - \mathrm{trace}\left(\mathbf{C}_{m\_\mathrm{iso}}^{e^2}\right) \right)\Big/2$ is the elastic second invariant, $\mathbf{C}_{m\_\mathrm{iso}}^e = \mathbf{F}_{m\_\mathrm{iso}}^{e^T} . \mathbf{F}_{m\_\mathrm{iso}}^e$ being the elastic part of the isochoric right Cauchy-Green deformation tensor of the rubber matrix. Two valuable differences from the Kroon (2010) work can be noted regarding the considering topological constraints. Firstly, the power-law part originating from the non-affine polymer chain deformation consideration is not introduced in Eq. (IV.8), only the I_2-dependent part based on the tube theory is kept. Secondly, due to similarities of the physics, the non-constrained and constrained stretches are replaced, respectively, by the viscous and elastic stretches.

The following modified version of the three-chain strain-energy function ψ_3 is used:

$$\psi_3 = \frac{n_3 k_B T N_3}{3} \sum_{i=1}^{3} \left[\lambda_{i\_c}^{e} \beta_{i\_c} + \ln\left(\frac{\beta_{i\_c}}{\sinh \beta_{i\_c}} \right) \right] \tag{IV.9}$$

in which the terms N_3 and n_3 are the two material parameters related to the three-chain model with signification analogue to the counterparts of the eight-chain model. Here, β_{i_c} is the inverse Langevin function given by $\beta_{i\_c} = \mathcal{L}^{-1}\left(\lambda_{i\_c}^{e}\right)$ in which $\lambda_{i\_c}^{e} = k\lambda_{i\_m}^{e} \big/ \sqrt{N_3}$ is introduced to consider the topological constraints of the polymer chains to account for the non-affine deformation because of the fluctuations of the junction points. The term $\lambda_{i\_m}^{e}$ is the principal elastic stretch in the i^{th} direction and k is a constant referring to the strength of the constraints.

The three-chain units and the I_2 dependence are the two key aspects combined and added to the original eight-chain model to cancel its difficulties to capture the biaxial mechanics.

The quantities $\mu_8 = n_8 kT$ and $\mu_3 = n_3 kT$ represent the respective shear moduli of the networks in the non-deformed state. The shear modulus of the rubber matrix at small-strains writes $\mu_m = \mu_8 + \mu_3$. According to Elias-Zuniga and Beatty (2002), and Bechir et al. (2010), the following proportional relationship between each network modulus and the rubber matrix modulus is retained:

$$\mu_3 = \left(1 - \frac{\eta \lambda_{\max\_c}^{e}}{\sqrt{N_3}} \right) \mu_m \text{ and } \mu_8 = \omega \sqrt{\frac{I_{1m}^{e}/3}{N_8}}\, \mu_m \tag{IV.10}$$

where $\lambda_{\max\_c}^{e} = \max\left(\lambda_{11\_c}^{e}, \lambda_{22\_c}^{e}, \lambda_{33\_c}^{e}\right)$ and, η and ω are constants related to the strength of chain interactions.

IV.2.2.2 Free energy of the particles

The strain-energy function of the particles ψ_p is given by (Yin et al., 2002):

$$\psi_p = \left(\frac{\lambda_p}{2} \left(\chi_1 + 3\chi_2 \right)^2 + \mu_p \left(2\chi_1\chi_2 + 3\chi_2^2 \right)^2 \right) \bar{\varepsilon}_{\text{vol}}^2 + \mu_p \chi_1^2 \bar{\boldsymbol{\varepsilon}}_{\text{iso}} : \bar{\boldsymbol{\varepsilon}}_{\text{iso}} \tag{IV.11}$$

where $\bar{\varepsilon}_{\text{vol}}$ is the Hencky volumetric strain of the composite, $\bar{\boldsymbol{\varepsilon}}_{\text{iso}} = \ln \bar{\mathbf{F}}_{\text{iso}}$ is the isochoric Hencky strain tensor of the composite, μ_p is the Lame's constant of the particles and, χ_1 and χ_1 are given by:

$$\chi_1 = \frac{\mu_{mp}}{2w - M - \phi} \text{ and } \chi_2 = \frac{K_{mp}}{3\left(2w + 3m - M - \phi\right)} - \frac{\chi_1}{3} \tag{IV.12}$$

IV.2.2.3 Viscous flow

The viscous flow is captured by the accumulated viscous strain rate $\dot{\gamma}_m^v$ taking here the following form:

$$\dot{\gamma}_m^v = \frac{k_v - k_u}{\left(\sqrt{I_{1m}^v / 3} - 1 \right)^{\alpha}} \left\| \boldsymbol{\sigma}_m \right\| \tag{IV.13}$$

where α is the stretch-dependency factor and $I_{1m}^v = \text{trace}\left(\boldsymbol{\varepsilon}_{m\_\text{iso}}^v . \boldsymbol{\varepsilon}_{m\_\text{iso}}^{v^T} \right)$ is the viscous first invariant, $\boldsymbol{\varepsilon}_{m\_\text{iso}}^v = \ln \mathbf{F}_{m\_\text{iso}}^v$ being the viscous isochoric Hencky strain tensor. The term k_v represents conceptually the strength of inter-chain interactions and is expressed as follows (Saadedine et al., 2021):

$$k_v = k_{v\_0} \left(1 + \left| \frac{\dot{\lambda}_{\max}}{\dot{\lambda}_0} \right| \right)^{\tau} \exp\left(\text{sgn}\left(\dot{\lambda}_{\max} \right) \right) \tag{IV.14}$$

in which k_{v_0} is the viscous multiplier, τ is the rate-dependency factor, $\dot{\lambda}_0$ is the reference loading rate, $\dot{\lambda}_{\max} = \max\left(\dot{\lambda}_{11}, \dot{\lambda}_{22}, \dot{\lambda}_{33} \right)$ is the maximum stretch rate, $\text{sgn}\left(\dot{\lambda}_{\max} \right) = +1$ for stretching ($\dot{\lambda}_{\max} > 0$) and $\text{sgn}\left(\dot{\lambda}_{\max} \right) = -1$ for retraction ($\dot{\lambda}_{\max} < 0$). The recovery term k_u conceptually captures the

conformational change upon unloading. With the assumption of a proportionality to the maximum viscous strain $\varepsilon^{v}_{m\_\max} = \max\left(\varepsilon^{v}_{11m\_\mathrm{iso}}, \varepsilon^{v}_{22m\_\mathrm{iso}}, \varepsilon^{v}_{33m\_\mathrm{iso}}\right)$, it takes a similar form:

$$k_u = k_{u\_0}\left(1+\left|\frac{\dot{\lambda}_{\max}}{\dot{\lambda}_0}\right|\right)^{\tau} \varepsilon^{v}_{m\_\max} \exp\left(\mathrm{sgn}\left(\dot{\lambda}_{\max}\right)\right) \tag{IV.15}$$

where k_{u_0} is the viscous multiplier and the other parameters are defined above.

IV.2.2.4 Dynamic bonds

The microscopic origin of the degradation at the origin of the Mullins effect or even the final failure can be attributed to the destruction of bonds from the crosslinks between chains, the links between chains and particles or the internal chain fracture. To capture the failure when the network losses all connectivity, the dynamic detachment mechanism of bonds is considered using the following changes in average chain lengths of the two networks:

$$N_3(t) = \frac{N_{3(t=0)}}{N_{on/off}} \text{ and } N_8(t) = \frac{N_{8(t=0)}}{N_{on/off}} \tag{IV.16}$$

with $\mu_m = \mu_{m(t=0)} N_{on/off}$. The terms $N_{3(t=0)}$, $N_{8(t=0)}$ and $\mu_{m(t=0)}$ are the initial values and $N_{on/off}$ is defined by the following kinetics:

$$\dot{N}_{on/off} = 1 - N_{on/off}\left(1+k_{on/off}\right) \tag{IV.17}$$

in which $k_{on/off}$ is the rate of detachable bonds given by:

$$k_{on/off} = k_{on/off\_0} \exp\left(\frac{\|\boldsymbol{\sigma}_m\|}{\sigma_{off} N_{on/off}}\right) \tag{IV.18}$$

where k_{on/off_0} is a material constant and σ_{off} is a scale factor controlling the bonds strength.

The chain scission occurs for chains with extensibility smaller than the applied maximum stretch level $\lambda^{old}_{\max}$ while the chains with extensibility higher than $\lambda^{old}_{\max}$ remain unbroken, as main Mullins effect characteristic. This deformation-induced damage behavior can be captured by a change in the average chain length with the historical maximal deformation by following the equation:

$$N_8 = N_{8(t=0)} + \left(N_{8(t=0)} - N_{\lambda_{\max}} \right) N_\lambda \tag{IV.19}$$

in which $N_{\lambda_{\max}}$ and N_λ are expressed as:

$$N_{\lambda_{\max}} = N_{8(t=0)} \exp\left(\left(\frac{\lambda_{\max}^{old} - 1}{\lambda_{\max}^{chain} - 1} \right)^2 \right) \text{ and } N_\lambda = \left(1 - \exp\left(- \left(\frac{\lambda - 1}{\lambda_{\max}^{old} - 1} \right)^2 \right) \right) \tag{IV.20}$$

where $\lambda_{\max}^{chain}$ is a material constant.

The above two equations introduce a possible mechanism for the Mullins effect and affect only the features of the non-entangled links of the main cubic cell, the entangled part being not concerned. This deformation-induced damage allows describing a smaller overall stress upon the reloading process compared to the virgin state. The local events of detachment mechanism lead in turn to changes in the local filler-chains interactions which is directly reflected in our approach by the modifications of the strain energy.

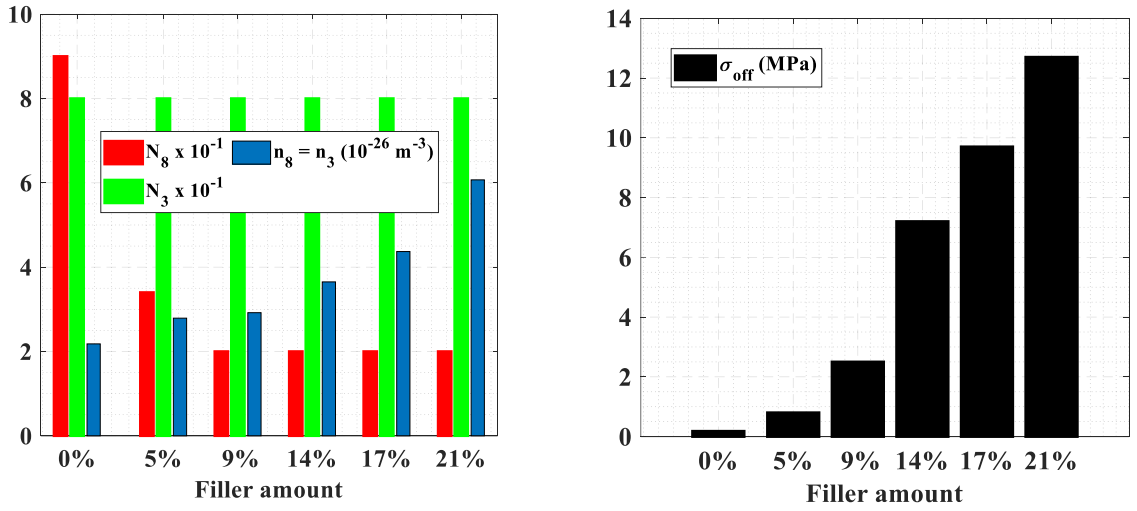

(a) (b)

Figure IV.2 Elastomeric matrix characteristics for different filler amounts: (a) mean chain density and mean chain length, (b) bonds strength.

IV.3 Model application

The micromechanical model has been coded in MATLAB software. To assess how the proposed model works for different loading modes, the model simulations are compared with available experimental data extracted from the paper of Mai et al. (2017) of an elastomeric material system with a wide range of amounts of particles: 0 %, 5 %, 9 %, 14 %, 17 % and 21 %. The examined behaviors include monotonic stress-strain response till failure and inelastic features characterized by the Mullins effect and the dissipation at room temperature and upon different loading paths: uniaxial extension (UA), equal-biaxial extension (EB) and planar extension (PS - Pure shear). The UA data are used to fit the model parameters while the other loading paths (EB and PS) are used to verify the model predictability with the same set of model parameters.

Parameter	Significance	Value
ν_m	Matrix Poisson's ratio	0.49
$\mu_p/\mu_m = K_p/K_m$	Moduli mismatch	50
k_{on/off_0} (s^{-1})	Dynamic bonds	5×10^{-5}
k_{v_0} ($MPa^{-1}\ s^{-1}$)	Viscous multiplier	9×10^{-6}
k_{u_0} ($MPa^{-1}\ s^{-1}$)	Viscous multiplier	2.3×10^{-6}
$\dot{\lambda}_0$	Reference loading rate	0.01
τ	Rate-dependency	0.8
α	Stretch-dependency	2.1
C (MPa)	Tube constraint	1×10^{-3}
η	Interactions strength	2.5
ω	Interactions strength	4.8
$\lambda_{\max}^{chain}$	Mullins constant	1.8

Table IV.3 Model parameters.

Some of the model parameters (elastically active chains features, filler elastic constants and filler amount) have direct physical meaning while other inputs (related to dissociation/re-association mechanism and to tube-constraints for inelasticity and multiaxiality) are physically interpretable. (Table IV.1) and (Figure IV.2) provide the model parameters obtained through a fitting

optimization based on the minimization of differences between micromechanical model simulations and uniaxial experimental data. (Figure IV.2) is a supplement of the identification results with the model parameters that were found modified with the variation in filler amount.

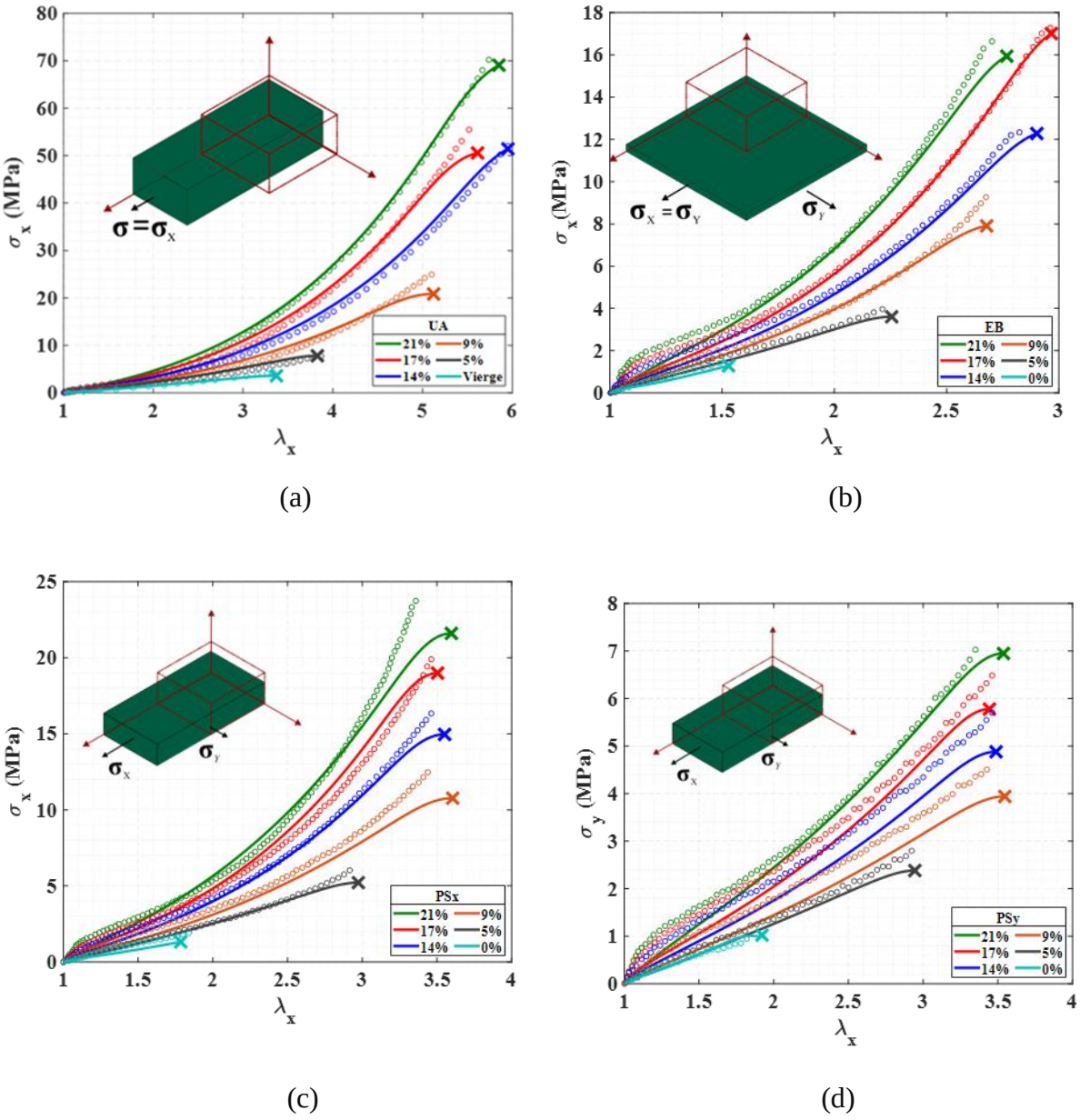

Figure IV.3 Stress-strain curves of the elastomers for different filler amounts: (a) uniaxial extension, (b) equal-biaxial extension, (c) planar extension in the (x) direction, (d) planar extension in the (y) direction (lines: model, symbols: experiments).

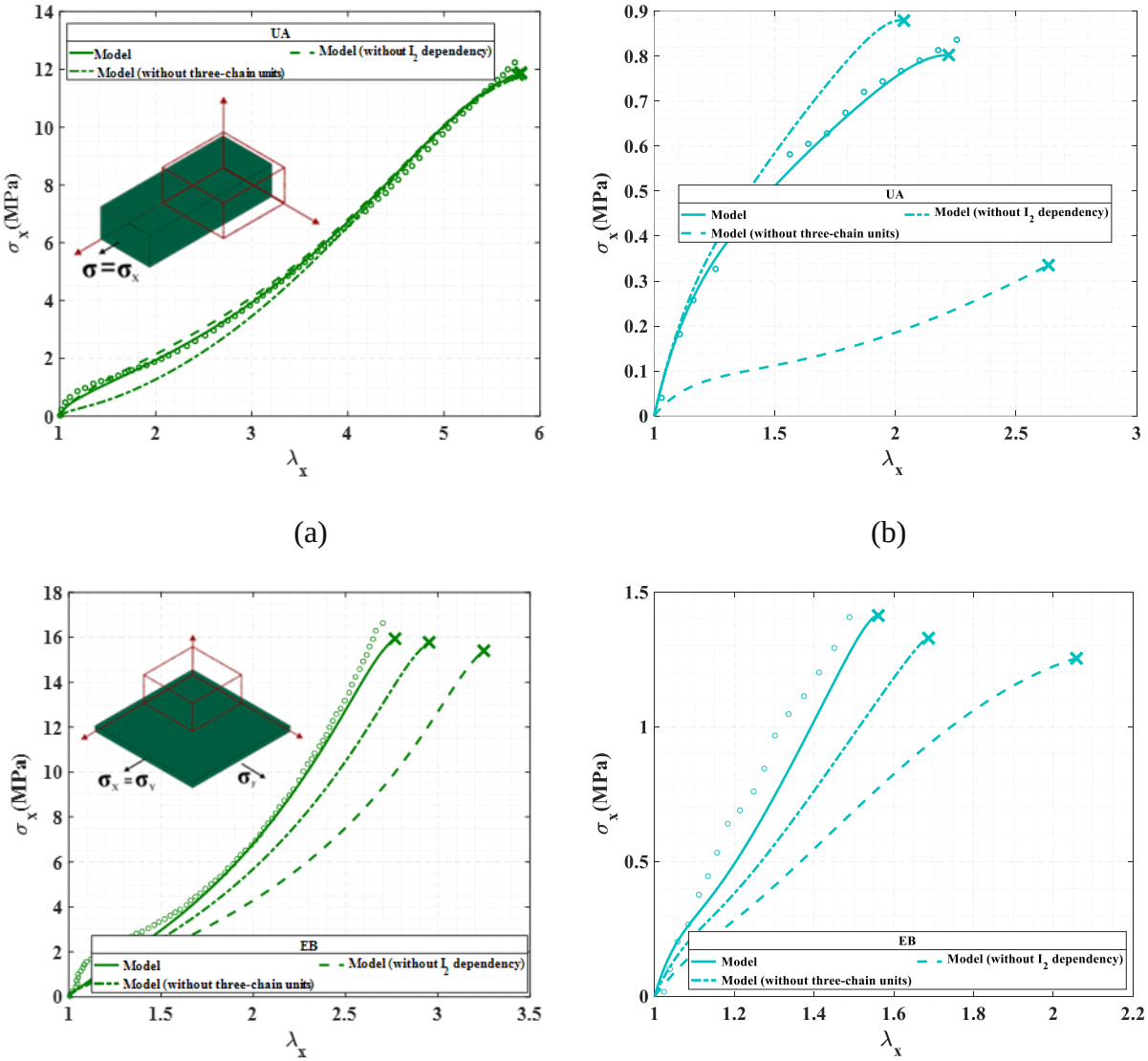

Figure IV.4 Stress-strain curves considering the influence of the three-chain units and the I_2 dependency under uniaxial extension for the elastomers with (a) ϕ = 21%, (b) ϕ = 0%, and under equal-biaxial extension for the elastomers with (c) ϕ = 21%, (d) ϕ = 0% (lines: model, symbols: experiments).

IV.3.1 Multiaxial monotonic stress-strain behaviors

It can be seen in (Figure IV.3a) the identification quality of the monotonic macro-stress evolution for different amounts of fillers. The simulations are conducted till failure, identified as the local

maximum stress level reached as indicated by the cross. The model identification can bring some physical interpretations in particular on the effective strengthening mechanisms and the underlying changes of the elastomeric structural features. The reinforcement mechanisms may be ascribed to stronger near-field direct interactions modifying the networks features inside the composite (Boutaleb et al., 2009) and resulting in better overall stretchability and strength. The presence of fillers is likely to act as additional crosslinking points to strengthen the network; the higher the filler amount, the smaller the mean chain length and the higher the mean chain density and the bonds strength (Figure IV.2). We show in (Figures IV.3b, IV.3c and IV.3d) how the model predicts the multiaxial experimental observations. A global view at these plots shows that the general trends of the model provide an acceptable description of the main features of the multiaxial monotonic response while taking into consideration the reinforcement mechanisms with a strong physical interpretation. The model adequately reproduces, as the filler content increases, the increase in biaxial strength and ductility. It is also satisfactory to observe that the considerable decrease of the ultimate properties under a biaxial stretching state is well predicted by the model. The rollover of the low-strain biaxial response is captured rather poorly by the model for the highest filler amounts. Nonetheless, the general trends of the large-strain macro-response variation with the biaxial stretching state are well predicted. Recall that the progressive local damage events of detachment mechanism identified under UA loading till failure were directly integrated to simulate the complete loss of load-bearing capability under EB and PS loadings. The reorganization of the chains upon the biaxial stretching state modifies in turn the interfacial interactions between elastomeric matrix and fillers and the topological constrains leading to lowest stress transfer and lowest overall toughening effects. (Figure IV.4) shows how the two main parts of the model (three-chain units and I_2 dependency) act on the uniaxial and equal-biaxial response of one selected filler concentration and the unfilled elastomer by canceling them in the plots. For the unfilled elastomer, the incomplete model does not provide a good agreement with the experiments under the two

loading paths, highlighting the importance of both three-chain units and I_2 dependency. It is obvious that the fitting of the incomplete model using uniaxial data would provide a better match for this loading mode but without the possibility of predicting the other loading mode. Interestingly, both three-chain units and I_2 dependency have negligible effects on the uniaxial behavior of the filled elastomer. Nonetheless, more significant effects are clearly observed on its equal-biaxial behavior.

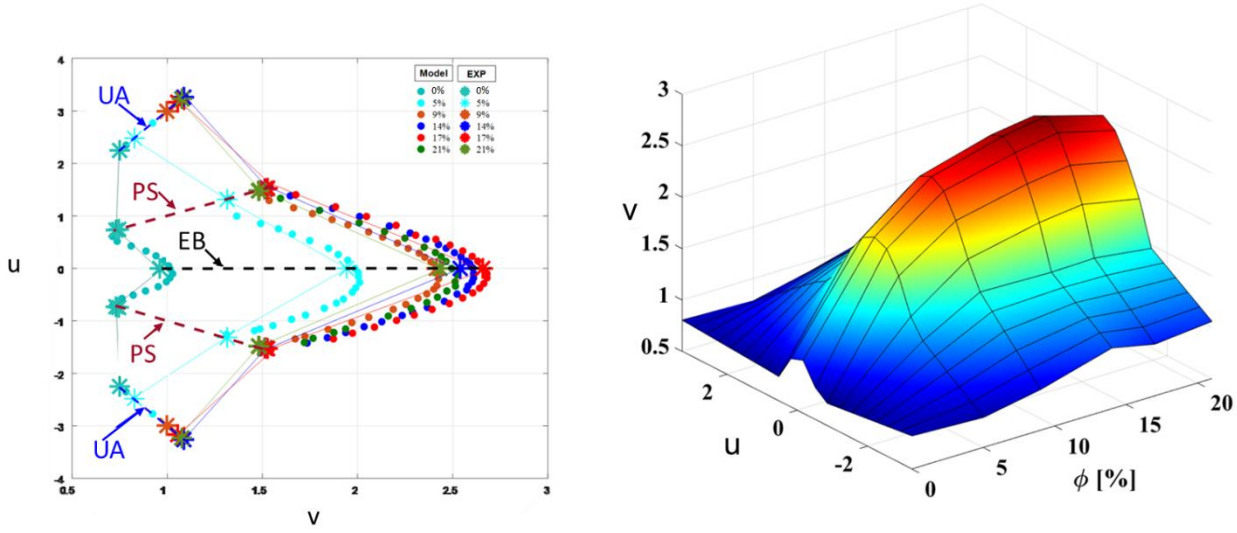

(a) (b)

Figure IV.5 Failure envelope in (a) the u-v plane and (b) the u-v-ϕ space.

The question that arises now is how the proposed model captures quantitatively the macroscopic multiaxial failure behavior, the predictability of the failure envelope being itself an open issue (Guo and Zaïri, 2021). The ultimate points in terms of maximum stress and maximum principal strain are computed by identifying the macroscopic failure state by the local maximum stress in the material response. The computed failure envelope is here represented in the following u-v plane:

$$u=(1+K)\ln(\lambda_{max}) \text{ and } v=(1-K)\ln(\lambda_{max}) \tag{IV.21}$$

where λ_{max} represents the maximum strain in the principal loading direction and $K=(\ln(\lambda_1)/\ln(\lambda_2))$ is the biaxial ratio.

The computed results are plotted in (Figure IV.5a) under a wide range of biaxial loading conditions such as a symmetric failure envelope with respect to the u axis is obtained. A very good agreement can be seen with the tendencies of the experimental data reported in the figure using asterisks. These plots show the predictive ability of the model to estimate the failure surface while considering both the particle concentration effect and the multiaxiality of the loading (Figure IV.5b).

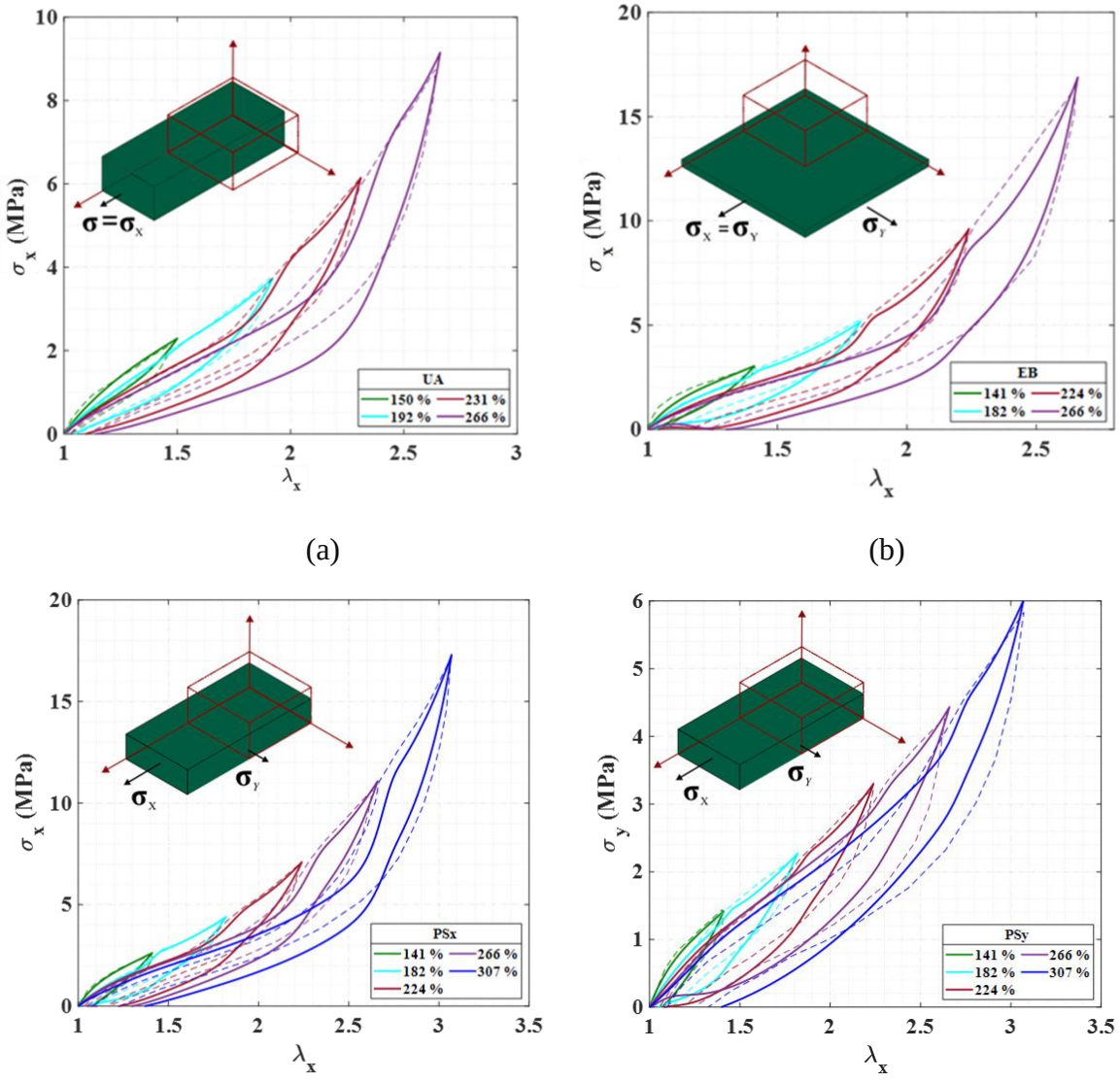

(a) (b)

(c) (d)

Figure IV.6 Stress-strain curves upon a stretching-retraction cycle of the elastomer with ϕ = 21%: (a) uniaxial extension, (b) equal-biaxial extension, (c) planar extension in the (x) direction, (d) planar extension in the (y) direction (solid lines: model, dashed lines: experiments).

IV.3.2 Multiaxial stretching-retraction behaviors

The model capacities upon cyclic loading at different stretch amplitudes are also examined. We can see in (Figure IV.6) that the model can match well the uniaxial cyclic data and predict well the biaxial cyclic data. The loss of stiffness when subjected to cyclic loading and the emergence of the residual strain over cycles, both characteristics of the Mullins effect, are well reproduced. The influence of the particle concentration is reproduced in a satisfactory manner by the model.

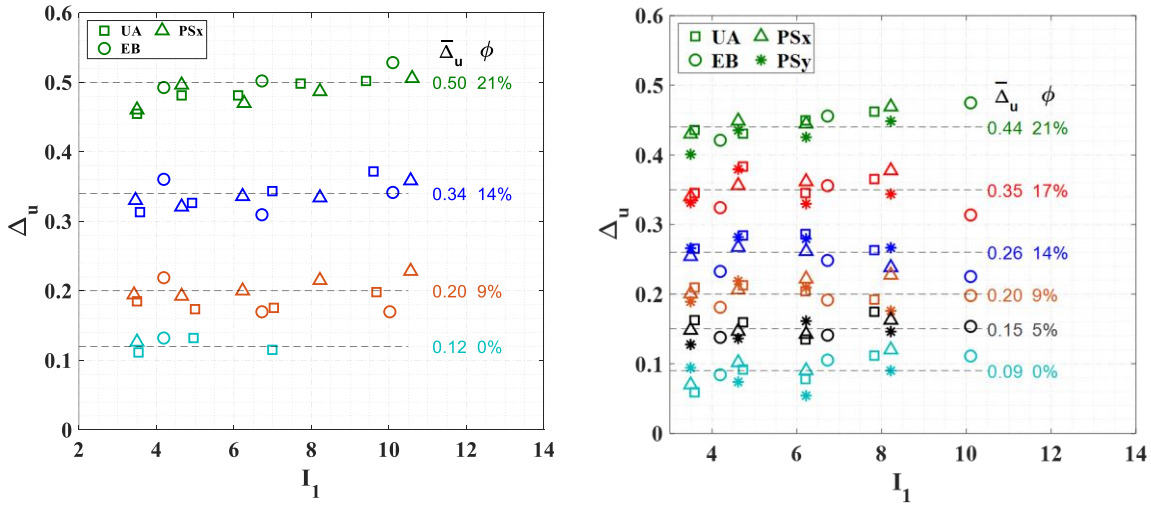

(a) (b)

Figure IV.7 Dissipated energy for the elastomers with different filler amounts under multiaxial loading-unloading sequences: (a) experimental data of Mai et al. (2017) and (b) model predictions.

IV.3.3 Multiaxial energy dissipation

The quantitative evaluation of the model regarding the multiaxial dissipation is now presented. The energy balance illustrated in (Figure IV.1) introduces two key parameters for multiaxial loading-unloading and loading-unloading-reloading sequences:

$$D_u = W_0 - W_u \text{ and } D_r = W_0 - W_r \tag{IV.22}$$

in which W_0 is the stored elastic energy in loading, W_u is the released energy in unloading and W_r is the stored elastic energy in reloading.

The dissipation factors representing the fraction of energy loss in input energy can be further defined as the following ratio for the two multiaxial loading sequences:

$$\Delta_u = \frac{D_u}{W_0} \text{ and } \Delta_r = \frac{D_r}{W_0} \tag{IV.23}$$

(Figures IV.7a and IV.8a) report the experimental data extracted from the paper of Mai et al. (2017) for the two dissipation factors Δ_u and Δ_r as a function of the first strain invariant for different types of deformation. The model predictions are presented in (Figures IV.7b and IV.8b) for all the amounts of particles. It worth noticing that energy data at filler amounts not reported in the paper of Mai et al. (2017) were provided in the figures for the sake of completeness.

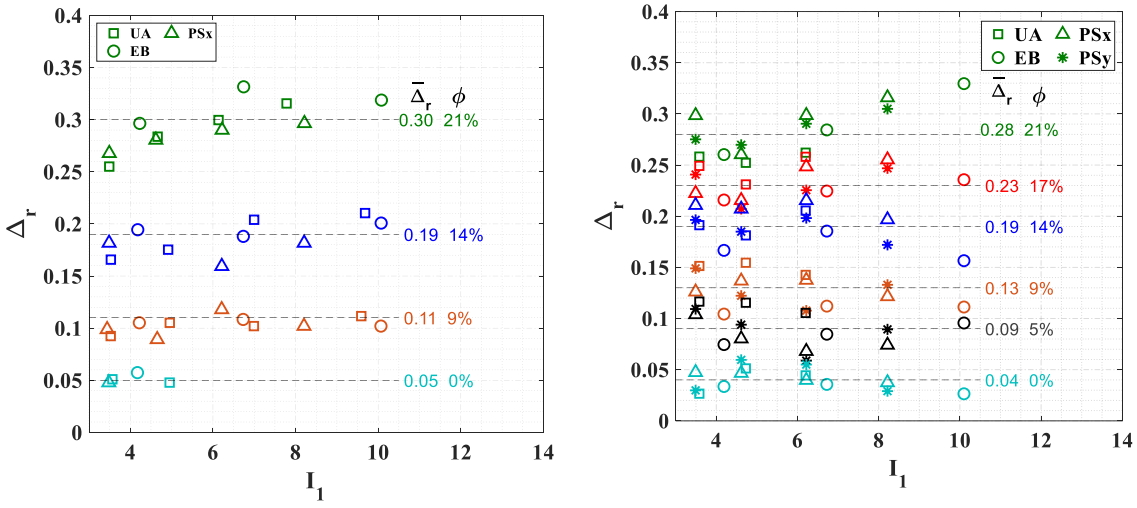

(a) (b)

Figure IV.8 Dissipated energy for the elastomers with different filler amounts under multiaxial loading-unloading-reloading sequences: (a) experimental data of Mai et al. (2017) and (b) model predictions.

(Figures IV.9a and IV.9b) present the data in the form of model-experimental plots in order to appreciate the discrepancies between experimental and predicted data. It can be seen that all points are close to the main bisectrix indicating a good agreement of our predictions with the experiments. The strong sensitivity of the magnitudes of Δ_u and Δ_r to the amount of particles is well predicted by the model. In (Figures IV.7(a,b) and IV.8(a,b)), the mean values are plotted in the form of straight lines around which the Δ_u and Δ_r data are arranged. It appears that after a certain extent of deformation, Δ_u and Δ_r become insensitive to both level and type of the deformation. In other words, at a given filler concentration, a constant fraction of the input energy dissipates independently of both the level and type of the deformation. The degree of local events of detachment mechanism and local filler-chains interactions increases with the filler concentration and appears proportional to the stored elastic energy.

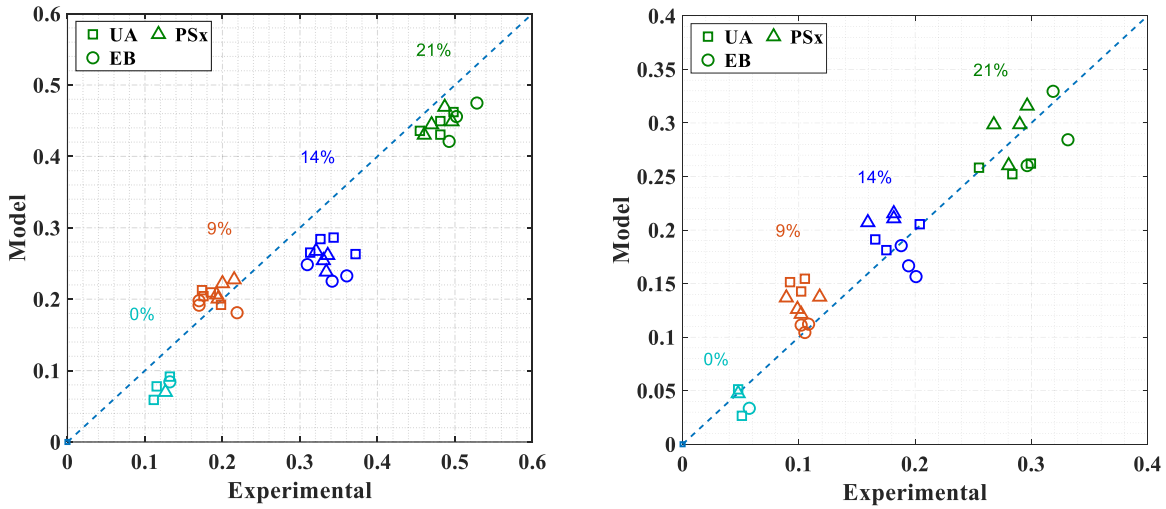

(a) (b)

Figure IV.9 Model vs. experimental for the dissipated energy at different filler amounts under (a) multiaxial loading-unloading sequences, (b) multiaxial loading-unloading-reloading sequences.

IV.4 Partial conclusion

In this chapter, we presented a physically-based model able to reproduce intrinsic behavior of elastomeric particulate composites in connection to the microstructure, the underlying mechanisms and the multiaxial loading conditions. Our approach considers a two-scale strategy: (i) a network decomposition at the chain scale based on the tube confinement theory to consider the combined effects of multiaxiality and inelasticity, (ii) the micro-macro scale transition to consider the effective contribution of particles. A quantitative evaluation of the model showed that the predictions successfully reproduced a series of multiaxial experimental observations under monotonic and cyclic conditions. We have clearly shown the trustworthiness of the model to give accurate estimates of the multiaxial energy dissipation in elastomeric particulate composites.

In future works, the proposed constitutive model will be implemented into a finite element program and numerical applications will be presented in order to investigate the damage and failure under more complex inhomogeneous deformation conditions.

References

Arruda, E.M., Boyce, M.C., 1993. A three-dimensional constitutive model for the large stretch behavior of rubber elastic materials. Journal of the Mechanics and Physics of Solids 41, 389-412.

Anssari-Benam, A., Bucchi, A., 2021. A generalised neo-Hookean strain energy function for application to the finite deformation of elastomers. International Journal of Non-Linear Mechanics, 103626.

Anssari-Benam, A., Bucchi, A., Saccomandi, G., 2021. On the central role of the invariant I2 in nonlinear elasticity. International Journal of Engineering Science 163, 103486.

Ayoub, G., Zaïri, F., Naït-Abdelaziz, M., Gloaguen, J.M., Kridli, G., 2014. A visco-hyperelastic damage model for cyclic stress-softening, hysteresis and permanent set-in rubber using the network alteration theory. International Journal of Plasticity 54, 19-33.

Bechir, H., Chevalier, L., Idjeri, M., 2010. A three-dimensional network model for rubber elasticity: The effect of local entanglements constraints. International Journal of Engineering Science 48, 265-274.

Boutaleb, S., Zaïri, F., Mesbah, A., Naït-Abdelaziz, M., Gloaguen, J.M., Boukharouba, T., Lefebvre, J.M., 2009. Micromechanics-based modelling of stiffness and yield stress for silica/polymer nanocomposites. International Journal of Solids and Structures 46, 1716-1726.

Boyce, M.C., Arruda, E.M., 2000. Constitutive models of rubber elasticity: A review. Rubber Chemistry and Technology 73, 504-523.

Chaabane, M., Ding, N., Zaïri, F., 2021. An approach to assess the thermal aging effects on the coupling between inelasticity and network alteration in filled rubbers. International Journal of Non-Linear Mechanics 136, 103783.

Dal, H., Gültekin, O., Açıkgöz, K., 2020. An extended eight-chain model for hyperelastic and finite viscoelastic response of rubberlike materials: Theory, experiments and numerical aspects. Journal of the Mechanics and Physics of Solids 145, 104159.

Dargazany, R., Khiêm, V.N., Itskov, M., 2014. A generalized network decomposition model for the quasi-static inelastic behavior of filled elastomers. International Journal of Plasticity 63, 94-109.

Destrade, M., Saccomandi, G., Sgura, I., 2017. Methodical fitting for mathematical models of rubber-like materials. Proceedings of the Royal Society A: Mathematical, Physical and Engineering Sciences 473, 20160811.

Doi, M., Edwards, S.F., 1988. The Theory of Polymer Dynamics (Vol. 73). Oxford University press.

Edwards, S.F., Vilgis, T. A., 1988. The tube model theory of rubber elasticity. Reports on Progress in Physics, 51, 243.

Elías-Zúñiga, A., Beatty, M. F., 2002. Constitutive equations for amended non-Gaussian network models of rubber elasticity. International Journal of Engineering Science 40, 2265-2294.

Flory, P.J., Erman, B., 1982. Theory of elasticity of polymer networks. 3. Macromolecules 15, 800-806.

Guo, Q., Zaïri, F., Baraket, H., Chaabane, M., Guo, X., 2017. Pre-stretch dependency of the cyclic dissipation in carbon-filled SBR. European Polymer Journal 96, 145-158.

Guo, Q., Zaïri, F., Guo, X., 2018. A thermo-viscoelastic-damage constitutive model for cyclically loaded rubbers. Part I: Model formulation and numerical examples. International Journal of Plasticity 101, 106-124.

Guo, Q., Zaïri, F., 2020. A physically-based thermo-mechanical model for stretch-induced crystallizable rubbers: Crystallization thermodynamics and chain-network crystallization anisotropy. International Journal of Plasticity 131, 102724.

Guo, Q., Zaïri, F., 2021. A micromechanics-based model for deformation-induced damage and failure in elastomeric media. International Journal of Plasticity 140, 102976.

Gurtin, M.E., Anand, L., 2005. The decomposition $F=F^eF^p$, material symmetry, and plastic irrotationality for solids that are isotropic-viscoplastic or amorphous. International Journal of Plasticity 21, 1686-1719.

He, H., Zhang, Q., Zhang, Y., Chen, J., Zhang, L., Li, F., 2022. A comparative study of 85 hyperelastic constitutive models for both unfilled rubber and highly filled rubber nanocomposite material. Nano Materials Science 4, 64-82.

Heinrich, G., Straube, E., Helmis, G., 1988. Rubber elasticity of polymer networks: theories. Polymer Physics 85, 33-87.

Heinrich, G., Kaliske, M., 1997. Theoretical and numerical formulation of a molecular based constitutive tube-model of rubber elasticity. Computational and Theoretical Polymer Science 7, 227-241.

Holzapfel, G., Simo, J., 1996. Entropy elasticity of isotropic rubber-like solids at finite strains. Computer Methods in Applied Mechanics and Engineering 132, 17-44.

Horgan, C.O., Saccomandi, G., 1999. Simple torsion of isotropic, hyperelastic, incompressible materials with limiting chain extensibility. Journal of Elasticity 56, 159-170.

Horgan, C.O., Smayda, M.G., 2012. The importance of the second strain invariant in the constitutive modeling of elastomers and soft biomaterials. Mechanics of Materials 51, 43-52.

Hossain, M., Amin, A.F.M.S., Kabir, M.N., 2015. Eight-chain and full-network models and their modified versions for rubber hyperelasticity: A comparative study. Journal of the Mechanical Behavior of Materials 24, 11-24.

James, H.M., Guth, E., 1943. Theory of the elastic properties of rubber. The Journal of Chemical Physics 11, 455-481.

Khiêm, V. N., Itskov, M., 2016. Analytical network-averaging of the tube model: Rubber elasticity. Journal of the Mechanics and Physics of Solids, 95, 254-269.

Kroon, M., 2011. An 8-chain model for rubber-like materials accounting for non-affine chain deformations and topological constraints. Journal of Elasticity 102, 99-116.

Liu, D., Ma, S., Yuan, H., Markert, B., 2022. Computational modelling of poro-visco-hyperelastic effects on time-dependent fatigue crack growth of hydrogels. International Journal of Plasticity 155, 103307.

Mahjoubi, H., Zaïri, F., Tourki, Z., 2019. A micro-macro constitutive model for strain-induced molecular ordering in biopolymers: application to polylactide over a wide range of temperatures. International Journal of Plasticity 123, 38-55.

Mai, T. T., Morishita, Y., Urayama, K., 2017. Novel features of the Mullins effect in filled elastomers revealed by stretching measurements in various geometries. Soft Matter 13, 1966-1977.

Meissner, B., Matějka, L., 2003. A Langevin-elasticity-theory-based constitutive equation for rubberlike networks and its comparison with biaxial stress–strain data. Part I. Polymer 44, 4599-4610.

Meissner, B., Matějka, L., 2004. A Langevin-elasticity-theory-based constitutive equation for rubberlike networks and its comparison with biaxial stress–strain data. Part II. Polymer 45, 7247-7260.

Melly, S. K., Liu, L., Liu, Y., Leng, J., 2021. A review on material models for isotropic hyperelasticity. International Journal of Mechanical System Dynamics 1, 71-88.

Miroshnychenko, D., Green, W.A., 2009. Heuristic search for a predictive strain-energy function in nonlinear elasticity. International Journal of Solids and Structures 46, 271-286.

Mohammadi, H., Dargazany, R., 2019. A micro-mechanical approach to model thermal induced aging in elastomers. International Journal of Plasticity 118, 1-16.

Morovati, V., Dargazany, R., 2019. Micro-mechanical modeling of the stress softening in double-network hydrogels. International Journal of Solids and Structures 164, 1-11.

Morovati, V., Bahrololoumi, A., Dargazany, R., 2021. Fatigue-induced stress-softening in cross-linked multi-network elastomers: Effect of damage accumulation. International Journal of Plasticity 142, 102993.

Puglisi, G., Saccomandi, G., 2016. Multi-scale modelling of rubber-like materials and soft tissues: An appraisal. Proceedings of the Royal Society A: Mathematical, Physical and Engineering Sciences 472, 20160060.

Saadedine, M., Zaïri, F., Ouali, N., Tamoud, A., Mesbah, A., 2021. A micromechanics-based model for visco-super-elastic hydrogel-based nanocomposites. International Journal of Plasticity 144, 103042.

Su, X., Peng, X., 2018. A 3D finite strain viscoelastic constitutive model for thermally induced shape memory polymers based on energy decomposition. International Journal of Plasticity 110, 166-182.

Wineman, A., 2005. Some results for generalized neo-Hookean elastic materials. International Journal of Non-Linear Mechanics 40, 271-279.

Wu, P. D., van der Giessen, E., 1992. On improved 3-D non-Gaussian network models for rubber elasticity. Mechanics Research Communications 19, 427-433.

Xiang, Y., Zhong, D., Wang, P., Yin, T., Zhou, H., Yu, H., Baliga, C., Qu, S., Yang, W., 2019. A physically based visco-hyperelastic constitutive model for soft materials. Journal of the Mechanics and Physics of Solids 128, 208-218.

Xiao, R., Mai, T.T., Urayama, K., Gong, J.P., Qu, S., 2021. Micromechanical modeling of the multi-axial deformation behavior in double network hydrogels. International Journal of Plasticity 137, 102901.

Yin, H.M., Sun, L.Z., Chen, J.S., 2002. Micromechanics-based hyperelastic constitutive modeling of magnetostrictive particle-filled elastomers. Mechanics of Materials 34, 505-516.

Zhou, J., Jiang, L., Khayat, R.E., 2018. A micro-macro constitutive model for finite-deformation viscoelasticity of elastomers with nonlinear viscosity. Journal of the Mechanics and Physics of Solids 110, 137-154.

General conclusion

General conclusion

The implantable devices that can match tissues mechanically, electrically and biologically, emerged in biomedical applications. The theoretical calculation and experimental validation can guide the manufacturing of soft materials with programmable responses. As a meaningful prerequisite of advanced applications of such new materials, the formulation of constitutive models is needed. Such tools would provide a better understanding of the separate and synergistic effects of key factors that govern the impressive improvements of their properties. In this regards, only micromechanics-based approaches allow to propose a framework avoiding (or at least limiting) the arbitrary inclusion of heuristic parameters. Such a development would offer a way to gain a better understanding of the overall properties and to provide detailed information for their design. The aim of this PhD thesis dissertation was to propose a quantitative prediction of the mechanics of hydrogel-based nanocomposites. A constitutive representation that considers as well history-dependent effects and local matrix-nanoparticle interaction had not been yet developed. In this work, we firstly developed a constitutive model to correlate the behavior of visco-super-elastic hydrogel-based nanocomposites to their internal network structures in terms of hydrogel matrix and inorganic nanoparticles properties. We presented a model based on the Eshelby inclusion theory and the micromechanics framework using the concept of cubic material volume to account for the effective role of nanoparticles on the nonlinear and finite-strain macro-behavior of hydrogel-based nanocomposites. The hydrogel-nanofiller material system was representatively regarded as a cubic unit cell containing nine particles. A central nanoparticle connects eight nanoparticles placed at the cube vertices via a number of hydrogel chains. The model explicitly

considers the chains network with dynamic reversible detachable/re-attachable mechanisms of bonds to coherently capture the rate-dependent extreme stretchability and some inelastic features including strong hysteresis upon stretching-retraction and continuous relaxation. A quantitative evaluation of our model was presented by comparisons to a few available experimental data of a variety of hydrogel-nanofiller material systems. To get even closer to the physics that governs hydrogel-based nanocomposites, the constitutive model was extended to take into account the mechanisms of nanofillers reinforcement and their changes due to the hydrogel swelling state. We thus improved the model by taking into account the hydrogel swelling state in order to provide a quantitative prediction of the visco-super-elastic response of swollen hydrogel-based nanocomposites. The model was applied to a high-swelling capacity hydrogel-based nanocomposite reinforced with different concentrations of inorganic nanoparticles. Monotonic stretching till failure, stretching-retraction and self-healing properties, all largely dependent on the swelling state, was used to verify the model capacities. The swelling-induced changes in both dynamic breaking-recombination mechanism and strength of interactions with nanofillers were pointed out thanks to the model. We had further enriched the physically-based model to reproduce multiaxial mechanics of soft materials reinforced by nanoparticles. Our approach considered a two-scale strategy: (i) a network decomposition at the chain scale based on the tube confinement theory to consider the combined effects of multiaxiality and inelasticity, (ii) the micro-macro scale transition to consider the effective contribution of particles. A quantitative evaluation of the model showed that the predictions successfully reproduced a series of multiaxial experimental observations under monotonic and cyclic conditions.

To summarize, we have successfully developed a useful predictive multiscale tool describing as realistic as possible the relation between microstructure evolution and overall multiaxial mechanics of reinforced soft materials. In the future, the developed tool may be beneficially applied in the advancement of biomedical engineering solutions. Improvements will be intended

to take into account the multiphysics coupling (chemical, thermal, electrical and biological) through the micromechanical framework introduced in this work. Thought a transition from academic investigations to future practical applications, the purchased goal will be to develop a robust predictive tool accounting for the underlying interactions with the human body. The accuracy of the constitutive theory was demonstrated by means of data taken from the literature, the realization of our own experimental measurements, especially considering the coupling with the environment under different stimuli (temperature and chemical) will be also very interesting to feed our models. It is also planned to begin the implementation of the model into a finite element code in order to perform non-homogeneous calculations.